UNIVERSITAT DE
BARCELONA

Magnetization Dynamics at the Nanoscale in Nanoparticles and Thin Films

Single-Molecule Magnets, Magnetic Vortices, and Magnetic Droplet Solitons

Sergi Lendínez Escudero

Magnetization Dynamics at the Nanoscale in Nanoparticles and Thin Films

Single-Molecule Magnets, Magnetic Vortices, and Magnetic Droplet Solitons

A Dissertation Submitted to
Facultat de Física
in Candidacy for the Degree of
Doctor of Philosophy
Programa de Doctorat de Nanociències

Departament de Física Fonamental

UNIVERSITAT DE BARCELONA

by

Sergi Lendínez Escudero

Advisors:
Javier Tejada Palacios
Ferran Macià Bros

Tutor:
Javier Tejada Palacios

Barcelona
September 2015

Magnetization Dynamics at the Nanoscale in Nanoparticles and Thin Films

Single-Molecule Magnets, Magnetic Vortices, and Magnetic Droplet Solitons

Sergi Lendínez Escudero

Universitat de Barcelona

Contents

List of Figures

Acknowledgments

So it seems the writing of this thesis is coming to an end. It has been a long time since I finished my degree on Physics and I started wandering around the faculty, looking for opportunities to keep learning, until I found Dr. Javier Tejada and he fascinated me with those tiny magnets having strange quantum effects.

Es por eso que, justamente, es la primera persona a quien quiero agradecer la confianza depositada en mí. Gracias Javier, por darme la oportunidad de trabajar todos estos años en este grupo, por mostrarme siempre ilusión en todos los proyectos, por confiar en el buen destino de esta tesis, incluso cuando yo he sido más pesimista, por tu paciencia y tu disponibilidad. Han sido unos cuantos años de charlas y discusiones científicas de las que he aprendido muchísimo.

Una altra persona sense la qual aquesta tesi no hauria estat possible és el meu codirector Dr. Ferran Macià. Gràcies Ferran, per tot l'esforç que has posat en tota l'elaboració d'aquesta tesi; amb els teus consells aquesta tesi només ha anat a millor. Gràcies també per les hores dedicades amb mi al laboratori i, sobre tot, per les dedicades fora; les hores d'escalada han estat una gran recàrrega d'energia.

També vull agrair tot el temps que hem passat junts als membres del Grup de Magnetisme. En especial al Dr. Joan Manel Hernàndez i al Dr. Toni Garcia. Joan Manel, gràcies per la teva paciència per ensenyar-me tot el que he pogut aprendre al laboratori, per totes les discussions que sempre han servit per anar un pas més enllà en la comprensió de la física i per ser tant proper amb tots els estudiants que hem passat per aquest grup. Gràcies Toni, perquè si bé no hem coincidit en gaires projectes, sempre m'has ajudat quan ho he necessitat. Gràcies de veritat a tots dos per fer que venir a treballar a aquest Grup sigui divertit, i per fer que, al marxar-ne, se'l trobi a faltar.

Moltíssimes gràcies a tots els meus companys del Grup de Magnetisme per ser també amics i generar un ambient de treball únic. Gràcies Cris, Saül, Víctor, Ricardo, Diego, Gian, Antonio i Jesús, que m'heu patit des del començament de la tesi. Als companys de despatx, per totes les converses serioses i no tan serioses. En especial a Diego, que hemos compartido el tramo final de nuestras tesis; ¡ahora salgamos a correr! Y a Gian, por los días de escalada que hay que mantener. I als més joves que han passat pel grup: Martí, Nahuel i Raimón, molta sort en el doctorat que comenceu.

Vull agrair al grup de la Dra. Neus Domingo a l'ICN per la col·laboració en les mesures de MFM, i al grup del Dr. Luis Hueso i el Dr. Fèlix Casanova a Nanogune per la col·laboració en les mesures de la droplet en funció de la temperatura, van ser uns dies molt productius.

I would also like to thank all the people I have been with during my various stays abroad. First, during my stay at the Paul Drude Institut in Berlin. Thanks to Dr. Paulo Santos for giving me the chance to be part of the group for some months, and for all the discussions, there is much to learn from you. Gracias en especial a Dr. Alberto Hernández, por tratarme tan bien durante mi estancia en Berlín; espero que nos volvamos a ver por Berlín. Thanks to the other members of the group Edgar and Adriano. And thanks to Pawel, it has been great to meet you and share such great moments.

Thanks to Dr. Val Novosad for giving me the chance to work at Argonne National Laboratory not only once, but twice! Thanks also to Dr. Clarence Chang for the chance to join the SPT-3G collaboration, even if it was far from my expertise, because I have learned much from it. Thanks to all the people I've worked with at Argonne, especially Vlad, Junjia, and my climbing friend Chrystian: you guys have taught me a lot in the clean room, and spending some days with you in Yosemite has been great. Gracias, Chrystian, por los días de escalada en Chicago y las quedadas por la ciudad, el invierno en Chicago ha sido más llevadero.

A les secretàries del departament Bea, Elena i Cristina, per fer-nos la vida més fàcil. En especial a la Bea, que resol en minuts molts dels meus mals de cap.

Quiero agradecer especialmente a quien más me ha soportado durante todos estos años. Gracias de corazón Vero. Gracias por escucharme cuando lo necesitaba, y por no hacerme caso cuando no hacía falta. Gracias por hacérmelo pasar bien y olvidar lo peor de la tesis. Gracias por enseñarme tantas cosas. Gracias, en definitiva, por estar a mi lado.

També vull agrair als meus amics Jordi, Chus, Berta, Dàmaris, Dani, Marta i Karen totes les estones. Ara podreu veure algunes de les coses que he fet aquells dies que no he pogut estar amb vosaltres perquè "hi havia heli" o havia de mesurar.

Por último, quiero agradecer a mi familia el apoyo incondicional y los ánimos que me habéis dado siempre. Por escucharme cuando necesitaba desfogarme y por saber cuándo animarme sin que os lo pidiera.

Resumen

En esta memoria de tesis se recogen algunos de los trabajos realizados durante mis años de doctorado en el Grupo de Magnetismo de la Universidad de Barcelona. Hay otra gran cantidad de trabajo que no se presenta aquí, aunque haya contribuido igualmente a mi formación. Con la memoria he querido plasmar las líneas de investigación más importantes que he seguido durante estos años.

Toda la tesis gira en torno al estudio de la dinámica de la magnetización. Aunque los sistemas estudiados son muy diversos, hay dos partes diferenciadas. En la primera parte, que incluye los capítulos sobre el efecto Doppler y el Mn_{12}, se usa un modelo de macroespín, mientras que la segunda parte, correspondiente a los capítulos de vórtices y *droplet*, se estudia la dinámica de distintos tipos de dominios magnéticos, y el model de macroespín no puede usarse. Hay además cierto orden cronológico en los capítulos. La tesis empieza con el estudio del efecto Doppler rotacional, que fue mi primer trabajo en el grupo. En el siguiente capítulo estudio el Mn_{12}, un imán molecular. Si bien la publicación entorno a la cual gira el capítulo es de 2014, empecé a trabajar con este tipo de sistemas desde el principio de mi incorporación al grupo, dada la experiencia del grupo y de mi director Prof. Tejada en el tema. Las nanoparticulas de este material que se han estudiado están estrechamente ligadas con las conclusiones del capítulo del efecto Doppler. Posteriormente trabajé en la dinámica de dominios magnéticos. Primero, los vórtices magnéticos, sobre todo durante mis estancias en el Paul Drude Institut de Berlín y en el Argonne National Laboratory. Finalmente explico los experimentos más recientes en nanocontactos en capas finas ferromagnéticas con anisotropía magnética perpendicular al plano.

Los sistemas usados en esta tesis son sistemas magnéticos usados ampliamente en la investigación a la nanoescala. Aparte del interés puramente científico, estos sistemas son potencialmente aplicables en varios usos. Los imanes moleculares como q-bits en computadoras cuánticas; los vórtices magnéticos como oscilado-

res, como unidades de almacenamiento o como cristales magnónicos; y las *droplet* magnéticas como osciladores de alta frecuencia y transporte de información a alta velocidad y bajos campos magnéticos y corrientes eléctricas.

Efecto Doppler rotacional en la resonancia ferromagnética

El efecto Doppler consiste en el cambio de frecuencia de una onda percibido por un observador en movimiento relativo al emisor de la onda. Este es un efecto que se puede observar en nuestra vida cotidiana al oír un sonido agudo cuando un coche se aproxima, mientras que el sonido pasa a ser grave en cuanto se aleja. En ondas electromagnéticas el efecto es análogo, pero hay que tener en cuenta efectos relativistas. Un observador en la línea de movimiento con un emisor de ondas electromagnéticas percibirá un aumento de la frecuencia (o corrimiento al azul, *blueshift*) si el emisor se aproxima, o un descenso (o corrimiento al rojo, *redshift*) si el emisor se aleja. Este efecto se usa en los radares de velocidad en las carreteras, e incluso para dar explicación al corrimiento al rojo observado en el fondo de microondas, gracias a lo cual se determinó que el universo está en expansión. En la ciencia de materiales, el efecto Doppler se usa en la técnica de espectroscopia Mössbauer, que tiene una gran resolución. En este experimento, el movimiento relativo de una fuente radiactiva con el material en estudio permite analizar las interacciones hiperfinas de los núcleos atómicos. La alta resolución de este experimento ha permitido observar el llamado efecto Doppler transversal, producido cuando el emisor está en rotación, y el observador se mueve en la dirección transversal al eje de rotación. El efecto Doppler transversal es un efecto de segundo orden respecto al Doppler convencional, y no debe confundirse con el efecto Doppler rotacional. El efecto Doppler rotacional, a diferencia del efecto Doppler transversal, se produce cuando el observador y la fuente están en rotación relativa.

Cuando una onda electromagnética polarizada circularmente incide en un objeto ferromagnético en rotación, cabría esperar un desplazamiento en su frecuencia ferromagnética proporcional a la rotación. Sin embargo, debido a que la rotación de un sistema de cargas produce un campo magnético en el interior del objeto, en general se cancela cualquier posible desplazamiento. En ciertas circunstancias el efecto de la rotación podría no cancelarse, con lo que se produciría un desplazamiento de la frecuencia resonante.

Hemos estudiado los efectos que ejerce el campo ficticio creado por la rotación sobre el objeto ferromagnético. Hemos obtenido una expresión que determina la frecuencia resonante en función de los parámetros característicos de la muestra, teniendo en cuenta la polarización de la onda electromagnética y la velocidad de rotación. Además, hemos calculado la potencia absorbida por un objeto ferromagnético en rotación cuando se excita con una onda electromagnética polarizada linealmente.

Los resultados muestran que se produce un desplazamiento en la frecuencia resonante proporcional a la velocidad de rotación si existe anisotropía en el sistema. La anisotropía puede ser tanto magnetocristalina como de forma. Además, en el caso de una onda electromagnética polarizada linealmente, aparece un segundo pico de absorción con un desplazamiento respecto al pico principal correspondiente al doble de la velocidad de rotación. Sin embargo, la observación experimental de este efecto requiere de velocidades de rotación muy altas, lo que puede ser difícil de conseguir. En los sistemas conocidos como rotores libres, se incrustan nanopartículas en una matriz de manera que pueda rotar a grandes velocidades. En el siguiente capítulo estudiaremos nanopartículas que podrían usarse con este propósito.

Efecto túnel resonante de espín en nanoesferas de Mn_{12}

Los llamados imanes moleculares son cristales compuestos por un gran número de moléculas prácticamente idénticas que interactúan muy débilmente. Debido a esta débil interacción, el cristal tiene el mismo comportamiento que una sola molécula aislada. Cada una de estas moléculas está compuesta de átomos magnéticos que interactúan para formar un espín grande. Esto hace que los efectos cuánticos producidos en una sola molécula sean observables macroscópicamente en todo el cristal. En el caso del Mn_{12}, doce átomos de manganeso forman un espín total 10, con anisotropía cristalina uniaxial.

Para la observación de los efectos cuánticos a nivel macroscópico, lo óptimo consiste en alinear todos los ejes fáciles de un cristal en la misma dirección, u observar una sola molécula. Sin embargo, este procedimiento puede ser complejo a la hora de la fabricación.

En nuestros experimentos con nanoesferas de Mn_{12} no hemos alineado los ejes fáciles de las moléculas y, aun así, observamos las características de un sistema cuántico. En particular, la curva de imanación presenta saltos a los campos resonantes. También observamos un cambio de comportamiento en la temperatura de bloqueo en los campos resonantes debido al cambio de la barrera efectiva.

Mediante el análisis de moléculas con los ejes fáciles dispuestos aleatoriamente, argumentamos que efectivamente este es el comportamiento a esperar y que, en general, el efecto túnel resonante se presenta como picos en la derivada de la magnetización en torno a los campos resonantes, incluso en muestras no ordenadas. Este resultado facilita la caracterización de compuestos candidatos a imanes moleculares, ya que no es necesaria la formación de monocristales.

Creación de un antivórtice mediante excitación dinámica de un vórtice magnético en elipses ferromagnéticas y estudio de muestras gruesas con forma de estadio

A diferencia de los sistemas descritos anteriormente, la magnetización en capas finas de materiales ferromagneticos tiende a formar dominios magnéticos. A pesar de que la configuración de la magnetización puede ser muy compleja, se puede estudiar la dinámica de cada dominio como un objeto. El vórtice magnético es una configuración quiral prácticamente bidimensional de la magnetización que aparece cuando las dimensiones de muestras ferromagnéticas con forma cilíndrica se reducen, pasando a una forma más parecida a un disco. En el centro de este tipo de muestras la magnetización apunta fuera del plano para minimizar la gran energía de intercambio producida por la configuración antiparalela de la magnetización. Una de las características de estos vórtices es que se pueden caracterizar por el movimiento del núcleo. Este movimiento se produce a una frecuencia característica que depende de las dimensiones del disco, típicamente en el rango de centenares de MHz a algunos GHz. Si el vórtice se excita a esta frecuencia mediante un pulso de alta potencia, es posible invertir la dirección del núcleo. Este fenómeno podría usarse para almacenar información. La inversión del núcleo también se puede hacer mediante la excitación de ondas de espín a frecuencias más altas, del orden del GHz y decenas de GHz.

El proceso de inversión del núcleo ha sido objeto de investigación durante los últimos años. Estos estudios revelan que el proceso de inversión es complejo, y conlleva la aparición de una pareja vórtice-antivórtice con la magnetización del núcleo antiparalela respecto al núcleo original. A continuación, el nuevo antivórtice y el vórtice original se aniquilan, generando ondas de espín en el proceso. Así pues, el estudio de la dinámica de los antivórtices por separado puede revelar también detalles del proceso de inversión de vórtices.

Más recientemente se ha empezado a trabajar con discos acoplados. Debido a las interacciones entre discos, la dinámica de estos sistemas es más compleja que en el caso de discos aislados. Dichas interacciones hacen que sea posible identificar las configuraciones paralela y antiparalela entre los núcleos de los discos, así como controlar mediante la excitación dinámica el estado final del sistema.

En nuestros experimentos con elipses, hemos excitado el sistema en la configuración con un solo vórtice. Esta excitación genera un estado compuesto de un vórtice, un antivórtice y un vórtice, que hemos observado mediante imágenes de microscopía de fuerza magnética. Sin embargo, no hemos podido detectar el espectro de excitación asociado a este estado.

En el estudio de muestras gruesas con forma de estadio hemos observado un espectro de excitación complejo que no hemos podido asociar a ninguno de los estados conocidos hasta ahora. En las imágenes de microscopía de fuerza atómica hemos observado una configuración que asociamos a la presencia de una línea con la magnetización fuera del plano, que hemos reproducido con simulaciones micromagnéticas. Mediante simulaciones micromagnéticas hemos estudiado el efecto del campo magnético sobre esta configuración. El comportamiento simulado concuerda con el observado en las imágenes de microscopía. Argumentamos que la excitación de esta configuración produce una gran variedad de modos, lo cual complica el espectro y, de aquí, que no podamos asociar nuestras medidas a ningún modo.

Observación de frecuencias de deriva en solitones *droplet* magnéticos y fijación de la *droplet* a bajas temperaturas

Otra forma de conseguir dominos magnéticos es mediante excitaciones con corrientes eléctricas en capas finas de materiales ferromagnéticos. Los solitones son excitaciones localizadas en sistemas dinámicos. Una de sus características es su estabilidad. Los solitones magnéticos se pueden producir en materiales ferromagnéticos sin amortiguamiento mediante ondas de espín localizadas. Estos objetos se caracterizan por tener la magnetización en la zona localizada en dirección opuesta al resto. Sin embargo, los materiales reales siempre tienen amortiguamiento. El amortiguamiento se puede compensar con una corriente de electrones polarizados, que genera un momento de fuerza de transferencia de espín (STT). La localización se consigue usando un nanocontacto por el que pasa la corriente. En este caso, hablamos de solitones *droplet* magnéticos con disipación, ya que es necesario mantener la corriente para evitar la disipación. Estas excitaciones se observaron experimentalmente por primera vez hace pocos años, y están siendo objeto de investigación debido a su potencial aplicabilidad. Por un lado, se podrían usar para transportar información. Por otro lado, sus propiedades dinámicas hacen que sean buenas candidatas para dispositivos de espintrónica, ya que requieren baja densidad de corriente y bajo campo magnético para generarse.

Sin embargo, en los experimentos anteriores se observó que las medidas de resistencia no correspondían a una inversión total de la magnetización de la *droplet*. Experimentos a baja temperatura revelaron que, en este caso sí, la magnetización de la *droplet* estaba próxima a una completa inversión.

En nuestros experimentos hemos observado la aparición de un espectro de baja frecuencia (decenas o centenares de MHz) que atribuimos al movimiento de la *droplet* como un todo. Esto resulta en una resistencia promedio inferior a la correspondiente a una inversión total, lo cual explica los resultados anteriores. Mediante simulaciones micromagnéticos obtenemos algunos posibles orígenes del movimiento de baja frecuencia. En general, cualquier asimetría en el nanocontacto (como diferencias de anisotropía) produce un campo efectivo transversal que desplaza la *droplet* lateralmente fuera del nanocontacto. En cuanto la *droplet* sale de la región del nanocontacto, el amortiguamiento domina y se destruye. A la vez, la corriente aplicada en el nanocontacto vuelve a crear la *droplet*.

En las medidas de los parámetros característicos de la *droplet* en función de la temperatura hemos observado un incremento en la corriente umbral de creación con la temperatura, así como una disminución en el campo de creación y en el cambio de resistencia. Todo esto lo hemos asociado a efectos de anclaje. Al bajar la temperatura, los efectos de anclaje aumentan. Argumentamos que esto facilita la creación de la *droplet*. Por un lado, hace más difícil los efectos de deriva observados anteriormente, ya que fijan la posición de la *droplet*, lo cual también explica el mayor cambio de resistencia a menor temperatura. Por otro lado, fijan la magnetización en cuanto se invierte, con el resultado de una corriente de creación menor.

1

Introduction

Research in magnetic materials leads to new devices and technologies. As the technology progresses, the devices become smaller and this miniaturization allows more storage capacity and lower costs in the production of new technologies. As new and smaller materials are fabricated, new phenomena appear and thus new physics is needed to describe them. Nanomaterials meet characteristics of both the microscopic quantum world and the macroscopic classic world. This intermediate length scale is known as *mesoscale*. Nanomaterials can be obtained in a variety of forms, being nanoparticles and magnetic ultra-thin films some of the most used. These magnetic systems are very different in their composition: nanoparticles are grown with chemical reactions, and thin films are grown on a substrate by nanofabrication techniques such as sputtering or electron-beam evaporation. The magnetization might not be uniform in a magnetic thin film or in a large magnetic nanoparticle leading to the formation of magnetic domains. Magnetic domains are static structures that appear due to competition of the different magnetic energies and can be used to store and transport information. Magnetization dynamics, in addittion, offers new capabilities for applications and at the same time allows the study of new physical phenomena. Understanding the spin dynamics of nanomaterials and the evolution of the magnetization is a key process to develop faster devices and technologies. In this dissertation I studied the dynamics of the magnetization in a variety of systems; from the quantum relaxation process in nanoparticles of a single-molecule magnet to dynamical excitations in ferromagnetic thin films, including a theoretical study of the effect of a rotating body to the ferromagnetic resonance. The thesis presents mostly experimental results, but there are also some theory and simulation approaches.

In the first part of the thesis I began with a study of the magnetization dynamics in a rotating magnetic body. This work was first done theoretically because the experimental observation is difficult. With that work we find that very high rotating speeds are needed. Mechanically, this is challenging. However, systems known as free rotors may achieve high rotating speeds. Free rotors can be obtained with nanoparticles embedded in a matrix. I later on studied the dynamics of nanoparticles of a single molecule magnet (Mn_{12}), a compound that presents macroscopic quantum effects when is grown as a single crystal or when the molecules are oriented all along the same direction. In the second part of the thesis I studied the magnetization dynamics of macroscopic magnetic objects that appear in ferromagnetic thin films. I first studied vortices in patterned samples and investigated how to control the dynamical excitations of the vortices with an external microwave signal. Finally I studied dynamical solitons formed in electrical nanocontacts to ferromagnetic thin films due to the spin-transfer-torque effect.

Given the variety of systems studied, I have organized this dissertation in a way that each chapter is almost self-contained, having an introduction that describes the state of the art and the motivation, a background section with specific theory and details, the results and analysis sections, and finally a conclusion section that discusses and summarizes the chapter results. However, I found instructive to present in Chapter 2 the general theory of magnetism and the methods that are needed to understand and develop the studies and analyses presented throughout the dissertation.

The work on this thesis began with the study showed in Chapter 3. That chapter is devoted to a theoretical study of the effects of rotation on a magnetic body and the shift in the ferromagnetic resonance frequency perceived due to rotation. This effect is known as the rotational Doppler effect. This study was motivated by recent experiments in nanoparticles that detected peaks in the electron paramagnetic resonance that were attributed to fast rotating nanoparticles. The results presented here show that the Doppler effect on magnetic resonance would be observable in systems presenting some kind of anisotropy and able to rotate at large angular velocities, such as nanoparticles embedded in a matrix. The conclusions points towards the system studied in Chapter 4, nanoparticles of single-molecule magnets, as possible candidates for studying the effect.

Chapter 4 presents the experimental results on Mn_{12} nanospheres. Mn_{12} is a single-molecule magnet with uniaxial anisotropy. Mn_{12} has had a great importance in the discovery of macroscopic quantum tunneling, and has contributed vastly to the understanding of low-dimensional magnetism. In a Mn_{12} crystal, the quantum nature of the spin gives rise to noticeable macroscopic effects, such as steps in the magnetization curves. Hence, the quantum approach presented in Chapter 2 is needed to describe this kind of systems, even if the effects are measured at the macroscopic level. In order to observe quantum effects, it was needed to either synthesize large crystals with enough magnetic signal or use experimental techniques capable to measure single molecules. These approaches are challenging both from the fabrication point of view and from the measuring point of view. Simplifying the work needed to characterize single-molecule magnets showing quantum effects is hence of great relevance. In this work, we characterize non-oriented nanospheres of Mn_{12} and look for the characteristic behavior of quantum effects at the macroscopic level.

Chapters 5 and 6 study the dynamics of the magnetization from a different approach, in which a complex magnetization distribution moves as a sole entity. Chapters 3 and 4 use a macrospin approximation of the magnetization. In this approximation, the magnetization is determined by a unique vector in the whole sample. This is the usual approach in nanoparticles and saturated magnets. However, the magnetization distribution found in thin films (as the systems of Chapters 5 and 6) usually invalidates this approximation. For instance, in magnetic thin films, domains with magnetization pointing towards different direction usually form. Chapter 5 studies a specific type of magnetic domain structure appearing in cylindrical patterned structures in magnetic thin films: *magnetic vortices*. Magnetic vortices are interesting magnetic systems because they respond to oscillatory fields and, at the same time, have a magnetization distribution that minimizes the magnetic field coming out of the samples. A characteristic feature of the vortex is its small out-of-plane core, which can be excited and its direction reversed. This is of great importance because it allows fast and controllable switching between two states, which could be used as information bits. However, the physics of the reversal is not well understood. Apparently, it involves the creation and following annihilation of a new entity: the *antivortex*. Hence, obtaining antivortex systems and understanding their dynamic behavior is of great interest. The chapter shows the experimental work done in nanopatterned elongated samples. Elongated patterns favor antivortex formation, and we shall look for experimental evidence of the antivortex formation in spectral measurements and with magnetic force microscopy. Furthermore, the chapter studies the effects of the film thickness on the formation of the vortex with spectral measurements, magnetic force microscopy and micromagnetic simulations.

Chapter 6 also deals with a type of domain structure in a ferromagnetic film. In this case we use an electrical current to create magnetic excitation in a ferromagnetic thin film; we use the spin-transfer-torque effect to cancel the damping term and thus favor the formation of *magnetic solitons*. The chapter introduction explains how the excitation of localized spin waves may create a dissipative droplet soliton. The magnetic anisotropy plays an important role in the creation of these solitons, in particular perpendicular magnetic anisotropy is needed. Droplet solitons are interesting systems because of their stability, their fast dynamics, and the possibility to control them with electrical currents and low magnetic fields. Although magnetic droplet solitons were predicted long time ago, it was recently that were observed experimentally. The existing experiments show that a full reversal of the magnetization occurs at low temperature but only a partial reversal occurs at room temperature. In the experimental work presented in this chapter, we study the dynamic response of the droplet with ac measurements of the magnetoresistance at room temperature, and dc measurements at different temperatures. With the experiments at room temperature, we are able to give an explanation to the observation of partial reversal of the magnetization. In the experiments at different temperatures, we study the dependance of the characteristic parameters of the droplet creation and further discuss the stability of the droplet soliton.

2

Fundamentals

Magnetism and magnetic materials are used nowadays in a great variety of devices, from cutting-edge electronics and state-of-the-art laboratory equipment, to simple house hardware and daily-use sensors. Even though the physical origin for all these different applications is the same, it is clear that the scale of the problem determines the suitability of one model or another. For instance, we would fail to describe the forces that hold a tiny magnet in our freezer door with quantum mechanics and need instead the classical Maxwell equations; similarly, we would fail in trying to use the Maxwell equations to describe the interaction between two electrons and need, this time, quantum mechanics. In between the macroscopic classical world and the atomic quantum world we need to apply a combination of both quantum and classical descriptions; this is the *mesoscale* length. It is then crucial to determine the scale of a certain physical system and keep to the proper model describing it.

In this chapter we study the energies involved in the magnetism of materials. We go through the general formalism followed throughout the thesis. Because in this thesis we mainly work with mesoscopic systems, we need a semi-classical description of the energies. We generalize formalism to this semi-classical limit from the quantum origin of the different energies. In addition, we introduce the dynamics of the magnetization. We leave specific details on the treatment of some energies to the following chapters.

2.1 Magnetic Moments

When we place a body in a magnetic field, it may experience a torque that tends to align the body in a certain direction. The strength of this torque is determined by the magnetic field and by the *magnetic moment* $\vec{\mu}$, a property intrinsic to the body.

The total magnetic moment of a body is a certain combination of the magnetic moments of its components, that may interact in very different ways.

Let us consider the smallest components of a body: electrons. The magnetic moment of an electron has two microscopic contributions

$$\vec{\mu}_l = \gamma_e \hbar \vec{l}, \qquad \vec{\mu}_s = g_e \gamma_e \hbar \vec{s}, \tag{2.1}$$

where $\gamma_e = e/2m_e$ is the *gyromagnetic factor*, with e the charge of the electron and m its mass, $g_e \approx 2$ the electron spin g-factor, $\vec{l}$ is the orbital momentum and $\vec{s}$ the *spin quantum number*. These relations can be rewritten as

$$\vec{\mu}_l = -\mu_{\mathrm{B}} \vec{l}, \qquad \vec{\mu}_s = -g_e \mu_{\mathrm{B}} \vec{s}, \tag{2.2}$$

where $\mu_{\mathrm{B}} \equiv \hbar|\gamma_e| = 9.27 \cdot 10^{-24}$ Am^2 is the *Bohr magneton*, that gives the units of quantization of the magnetic moment of the electron.

In an atom with a total orbital momentum $\vec{L}$ and total spin $\vec{S}$, the total angular momentum is given by the operator $\vec{J} = \vec{L} + \vec{S}$, and hence its magnetic moment would be $\vec{\mu} = \gamma\hbar\vec{J}$. In general, one can always express the magnetic moment as

$$\vec{\mu} = \gamma\hbar\vec{S}, \tag{2.3}$$

and take the corresponding γ and proper total angular momentum of the system $\vec{S}$. Note that, in the case of an electron, $\vec{\mu}$ and $\vec{S}$ are of opposite sign, since $\gamma < 0$.

In the classical description, one has to take an average of the magnetic moment on a small volume V_0 containing a large number of atoms that are still small to maintain a uniform alignment of spins. Hence, we can define the *magnetization* $\vec{M}(\vec{r})$ as a "magnetic moment density", and the magnetic moment distribution $\vec{\mu}(\vec{r})$ on a body of volume V is given by

$$\vec{\mu}(\vec{r}) = \int_V \mathrm{d}^3 r \vec{M}(\vec{r})\,. \tag{2.4}$$

2.2 Magnetic Energies

Magnetic moments may be ordered depending on the interaction energy between electrons. The balance between the different energies in a system determines its ground state. In the following, we describe the most important energies that determine the state of a magnetic system.

2.2.1 Zeeman Energy

A magnetic moment $\vec{\mu}$ in an external magnetic field $\vec{B}_0 = \mu_0 \vec{H}_0$ ($\mu_0 = 4\pi \cdot 10^{-7}$ H/m being the *permeability of vaccum*) experiences a torque $\vec{\mu} \times \vec{B}_0$, and the energy of this interaction is given by

$$E = -\vec{\mu} \cdot \vec{B}_0 \,. \tag{2.5}$$

This effect holds whatever is the origin of the magnetic moment, i.e. classical or quantum. Hence, when acting on a spin $\vec{s}$ it can be expressed as

$$\mathcal{H}_{\text{Zeeman}} = -\gamma \hbar \vec{s} \cdot \vec{B}_0 \,, \tag{2.6}$$

and in the classical approximation of Eq. (2.4)

$$E_{\text{Zeeman}} = -\mu_0 \int \mathrm{d}^3 r \, \vec{M}(\vec{r}) \cdot \vec{H}_0 . \tag{2.7}$$

This energy is called the *Zeeman energy*. From this equations we see that the energy is minimum when $\vec{M}(\vec{r})$ and $\vec{B}_0$ point towards the same (parallel) direction, and maximum when they are antiparallel.

2.2.2 Exchange Energy

Ferromagnets have a magnetic moment even at zero field. Atoms in a material interact via the Coulomb potential, which depends on the position. Electrons also posses spin quantum number and, according to the Pauli exclusion principle, the total wave function must be antisymmetric. This condition imposes that, if the position wave functions overlap, the spin numbers must be different (anti-parallel alignment of spins) and, conversely, if the spin numbers are the same (parallel alignment of spins) the position wave functions cannot overlap [Chikazumi et al. 1997], see Fig. 2.1. The Heisenberg model describes this system with the Hamiltonian

$$\mathcal{H}_{\text{ex}} = -\sum_{n<m} J_{nm} \vec{s}_n \cdot \vec{s}_m \,, \tag{2.8}$$

where the interaction is between spins $\vec{s}_n$ and $\vec{s}_m$, the index n and m denoting positions, and J_{nm} is the *exchange constant* or *exchange integral*, which quantifies the energy difference between parallel and anti-parallel alignment of electron spins (the exchange of the two electrons, from which the interaction takes its name). Because the overlap of the wave functions decays exponentially with the distance, only the neighboring spins must be taken into account in the sumation of Eq. (2.8).

The sign of the exchange constant determines the type of spin order: parallel spins (*ferromagnetic* order) for $J_{ij} > 0$, and anti-parallel (*antiferromagnetic* order) for $J_{ij} > 0$. The absolute value determines the strength of the interaction and the temperature above which it disappears [Chudnovsky and Tejada 2006].

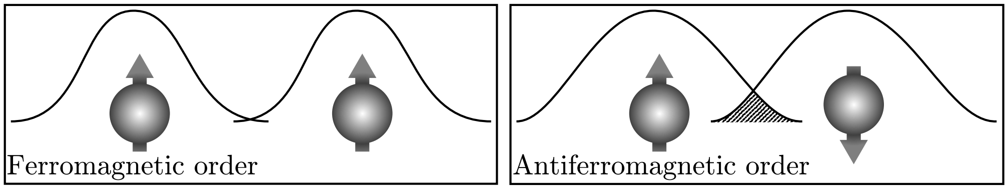

Figure 2.1: Two pairs of electrons with their wavefunctions and spins. (Left-hand-side panel) The position wavefunctions do not overlap, hence spins are parallel. (Right-hand-side panel) the position wavefunctions overlap, hence spins are antiparallel.

In the classical limit Eq. (2.8), turns into

$$E_{\mathrm{ex}} = -\frac{1}{2(\gamma\hbar)^2}\int \mathrm{d}^3r \int \mathrm{d}^3r' J(r-r')\vec{M}(\vec{r})\cdot\vec{M}(\vec{r'})\,. \tag{2.9}$$

As $J(r-r')$ decreases rapidly with increasing $|r-r'|$, taking the series expansion up to the quadratic term, the expression is reduced to

$$E_{\mathrm{ex}} = \frac{\mu_0}{2}\int \mathrm{d}^3r\,\alpha_{ij}\left(\frac{\partial\vec{M}}{\partial r_i}\cdot\frac{\partial\vec{M}}{\partial r_j}\right), \tag{2.10}$$

where

$$\alpha_{ij} = \alpha_{ji} = \frac{1}{2\mu_0(\gamma\hbar)^2}\int \mathrm{d}^3r\,J(\vec{r})r_ir_j \tag{2.11}$$

is the *exchange stiffness tensor*, and the indexes i and j run through the cartesian components (x, y, z). In the case of an isotropic material $\alpha_{ij} = \alpha\delta_{ij}$, the more common expression

$$E_{\mathrm{ex}} = A\int \mathrm{d}^3r\,\nabla^2\vec{M}\,, \tag{2.12}$$

is found, where $A = \mu_0\alpha/2 = 2JS^2N/a$ is the *exchange constant*, a being the nearest neighbor distance (i.e. cell size) and N the number of sites in the unit cell.

A useful quantity is the *exchange length*, the characteristic range of the exchange interaction, defined as

$$l_{\mathrm{ex}} = \sqrt{\frac{2A}{\mu_0M_0^2}}\,. \tag{2.13}$$

For the materials used in this thesis, it takes values ~ 10 nm.

2.2.3 Magnetocrystalline Anisotropy

The exchange energy described in the previous section is invariant under simultaneous rotations of all spins, i.e. it does not depend on the orientation of the total $\vec{S} = \sum_n \vec{s}_n$. In certain magnets, however, magnetic moment tends to align with an "easy axis", and some materials also have a certain "hard axis" that costs extra energy to align with. This is the *magnetic anisotropy.*

Generally, the magnetic anisotropy has the same symmetry as the crystal structure, and hence it is called *magnetocrystalline anisotropy.* The origin of the anisotropy is a relativistic spin-orbit interaction that alters the charge distribution depending on the orientation of the orbital electrons with respect to the crystal axes. In other words, due to the motion of the electrons they feel a magnetic field $\vec{B} = \vec{v} \times \vec{E}(\vec{r})$, given by the local electric field $\vec{E}(\vec{r})$ of the crystal [Chudnovsky and Tejada 2006]. This interaction makes the magnetization to align along the crystallographic axes, see Fig. 2.2.

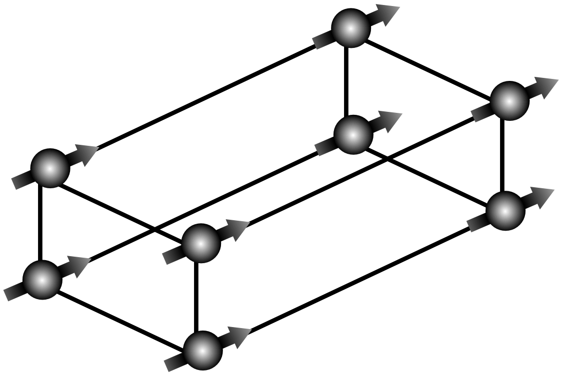

Figure 2.2: Due to spin-orbit coupling, spins minimize their energy when they align along the crystallographic axis.

The anisotropy of a certain crystal depends on the lattice symmetry, and it may be be uniaxial, biaxial, cubic, etc. The expression for any crystal geometry may be obtained taking into account that the energy should be invariable under rotation of the magnetization. This imposes the terms entering the energy to be even powers of the spin components or, equivalently, of the direction cosines. Limiting ourselves up to the 4th order, the general expression of the Hamiltonian is

$$\mathcal{H}_\mathrm{A} = b_{ij} s_i s_j + c_{ijkl} s_i s_j s_k s_l + \dots\ , \tag{2.14}$$

where b_{ij}, c_{ijkl} are the tensors of the second rank and fourth rank, and summation over indices $i, j, k, l = x, y, z$ has been omitted.

In the classic limit, the energy can be written as

$$E_{\mathrm{A}} = -\int \mathrm{d}^3r \left[\frac{\mu_0}{2}(\beta_{ij}M_iM_j) - \frac{\mu_0^2}{4}(\gamma_{ijkl}M_iM_jM_kM_l) + \ldots\right], \tag{2.15}$$

with β_{ij} the *anisotropy tensor* of second order, and γ_{ijkl} of fourth order. As explained above, the terms describing anisotropy are of relativistic smallness, hence the second order term dominates in the majority of cases and one may drop higher order terms.

Let us compare the quantum and classical expressions of the simplest case of *uniaxial anistropy* along the Z axis, with spin forming an angle θ with the axis. In the quantum model, it is described by the Hamiltonian

$$\mathcal{H}_{\mathrm{A}} = -DS_z^2\,, \tag{2.16}$$

with D being a constant, and S_z the spin projection in the Z axis. For $D > 0$, the energy is minimum when the spin is aligned along the Z axis—the *easy axis*. If $D < 0$ the energy, on the contrary, is maximum when the spin points in the Z axis, and minimum in the perpendicular plane; the Z axis is a *hard axis* and the XY plane is an *easy plane*.

In the classical approximation, the only term of the anisotropy different from zero is the term along the easy axis, chosen along the Z axis, $\beta_{zz} = \beta$; the energy can be written as

$$E_{\mathrm{A}} = -\frac{\mu_0}{2}\beta \int \mathrm{d}^3r \left(\hat{z}\cdot\vec{M}\right)^2 = K\int \mathrm{d}^3r \sin^2\theta(\vec{r}) + \mathrm{const.} \tag{2.17}$$

In the second term of the equation, K is the *anisotropy constant*, which is extensively used in the literature [Ashcroft et al. 1976; Chikazumi et al. 1997; Kittel 2004].

We may consider the effect of the anisotropy as an *anisotropy field* $\mu_0\vec{H}_K$, and the energy can be written as

$$E_{\mathrm{A}} = -\frac{1}{2}\mu_0 \int \mathrm{d}^3r\vec{M}(\vec{r})\cdot\vec{H}_K(\vec{r})\,, \tag{2.18}$$

and comparing with Eq. (2.15) for a second-order anisotropy, its value is given by

$$H_{Ki} = \beta_{ij}M_j\,. \tag{2.19}$$

2.2.4 Dipolar or Magnetostatic Energy

Spins in a solid also interact through the long range dipolar magnetic fields due to the fact that they are magnetic dipoles. The Hamiltonian of the dipolar interaction betweeen spins at locations n and m is

$$\begin{aligned}\mathcal{H}_\mathrm{d} &= \frac{\mu_0}{8\pi}(\hbar\gamma)^2 \sum_{n\neq m} \frac{1}{r_{nm}^5}\left[(\vec{s}_n\cdot\vec{s}_m)\vec{r}_{nm}^{\,2} - 3(\vec{s}_n\cdot\vec{r}_{nm})(\vec{s}_m\cdot\vec{r}_{nm})\right] \\ &= -\frac{\mu_0}{8\pi}(\hbar\gamma)^2 \sum_{n\neq m} s_{ni}s_{mj}\frac{\partial^2}{\partial r_{nmi}\partial r_{nmj}}\left(\frac{1}{r_{nm}}\right) ,\end{aligned} \tag{2.20}$$

where $\vec{r}_{nm} = \vec{r}_n - \vec{r}_m$ is the vector connecting the positions of the n and m spins.

In the classical limit, the above equation turns into

$$E_\mathrm{d} = -\frac{\mu_0}{8\pi}\int \mathrm{d}^3r \int \mathrm{d}^3r' \left[M_i(\vec{r})M_j(\vec{r}')\frac{\partial^2}{\partial r'_i \partial r'_j}\left(\frac{1}{|\vec{r}-\vec{r}'|}\right)\right]_{|\vec{r}-\vec{r}'|^3 > V_0} . \tag{2.21}$$

Even though its strength decays rapidly with increasing distance, this interaction must be averaged on the whole volume of the material and may become dominant in a macroscopic scale. Each magnetic moment interacts with other magnetic moments in the volume, and hence the total *dipolar energy* E_d depends on the configuration of the magnetization and on the shape of the solid. From magnetostatic (Maxwell) equations, it can be showed that the dipolar energy may be written as an interaction between a field $\vec{H}_\mathrm{d}(\vec{r})$ and the magnetization [Chudnovsky and Tejada 2006]

$$E_\mathrm{d} = -\frac{1}{2}\mu_0 \int \mathrm{d}^3r\, \vec{M}(\vec{r})\cdot\vec{H}_\mathrm{d}(\vec{r}) . \tag{2.22}$$

The field $\vec{H}_\mathrm{d}(\vec{r})$ is the *demagnetizing field*, as it is created by the free poles appearing on the surface and opposes to the magnetization, see Fig. 2.3. E_d and $\vec{H}_\mathrm{d}$ are also called the *magnetostatic energy* and *magnetostatic field*, because they are solely determined by the magnetization distribution.

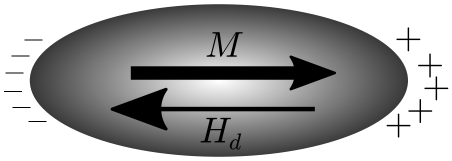

Figure 2.3: Illustration of the appearance of a demagnetizing field $\vec{H}_\mathrm{d}$, dependent on the solid shape.

The value and distribution of this field may be complex. For a uniformly magnetized ferromagnet, however, it can be analytically calculated [Ashcroft et al. 1976; Chikazumi et al. 1997; Chudnovsky and Tejada 2006] and expressed as

$$H_{\mathrm{d}i} = -N_{ij}M_j , \tag{2.23}$$

where N_{ij} is the *demagnetizing tensor*. In the case of an ellipsoid, the only non-zero components are $N_{xx} = M_{yy} = M_{zz} = 1/3$; for a long cylinder parallel to the z axis, the non-zero components are $N_{xx} = N_{yy} = 1/2$; and in the case of a thin plate on the xy plane, $N_{zz} = 1$.

The demagnetizing field creates easy directions for the magnetization similar to the crystalline anisotropy field presented in the previous section. Thus, the demagnetizing energy can be seen as a *shape anisotropy*, and added up to the crystalline anisotropy. An *effective anisotropy field* can then be written as

$$\vec{H}_{\mathrm{p}} = \vec{H}_K + \vec{H}_{\mathrm{d}} \,, \tag{2.24}$$

and an *effective anisotropy tensor*: $\beta_{ij}^{(\mathrm{eff})} = \beta_{ij} - N_{ij}$.

2.3 Magnetic Domains

In a ferromagnet of finite size, magnetization breaks into domains to reduce the magnetostatic energy generated by the demagnetizing field, see Fig. 2.4. As domains are formed, however, exchange energy and magnetocrystalline energy increase. The exchange energy tends to parallel align the magnetization, and the magnetocrystalline energy to align it along the easy axes. As a result, the stable magnetization configuration is calculated by minimization of the total energy

$$E = E_{\mathrm{d}} + E_{\mathrm{ex}} + E_{\mathrm{A}} + E_{\mathrm{Zeeman}} \,, \tag{2.25}$$

and is determined by the shape of the ferromagnetic body and its intrinsic properties such as the exchange stiffness and anisotropy constants.

The transition of the magnetic moment between domains occurs gradually along the *domain wall*, where magnetization rotates from one domain to another. While domain structure is determined by the geometry of the body, i.e. mainly exchange and magnetostatic energies, the type of domain walls and their width are determined by a competition between the exchange and the anisotropy energies.

The larger the exchange in a system, the thicker the wall, because a high rotation between adjacent spins costs more energy than smaller rotations, i.e. the wall tends to increase in size to minimize rotation angles of adjacent spins. At the same time, the larger the anisotropy, the thinner the wall, because deviation of spins from the easy axis occurs at a great energy cost, i.e. the wall tends to decrease, minimizing the spins not aligned with the easy axis [Chikazumi et al. 1997]. The equilibrium between these competing energies determines the *domain wall width*

$$l_{\mathrm{dw}} = \pi\sqrt{\frac{A}{K}} \,. \tag{2.26}$$

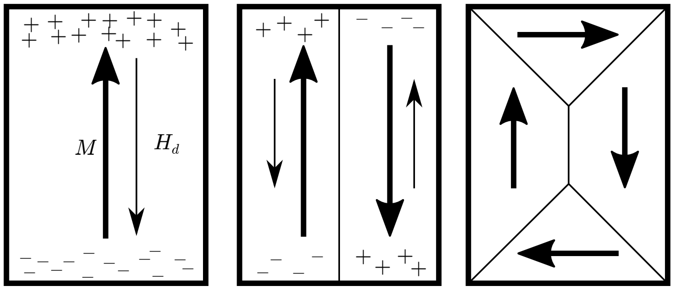

Figure 2.4: Ferromagnet breaking into domains to minimize the total energy. In a single domain, the magnetostatic energy is very high (left-hand-side panel), and the ferromagnet breaks into domains with opposite magnetization (center panel). Breaking into domains causes an increase of the exchange and anisotropy energies and thus it eventually arrives to an equilibrium (right-hand-side panel).

Domain walls can be divided into two classes depending on the direction of the magnetization in the wall:

- *Bloch wall*: the rotation of the magnetization occurs perpendicular to the plain determined by the domain magnetizations, Fig. 2.5. Its energy density is given by
$$\mathcal{E}_{\mathrm{Bw}} = 4\sqrt{AK}\,, \tag{2.27}$$
for a uniaxial ferromagnet, and $E_{\mathrm{d}} = 0$ for a sufficiently thick sample.

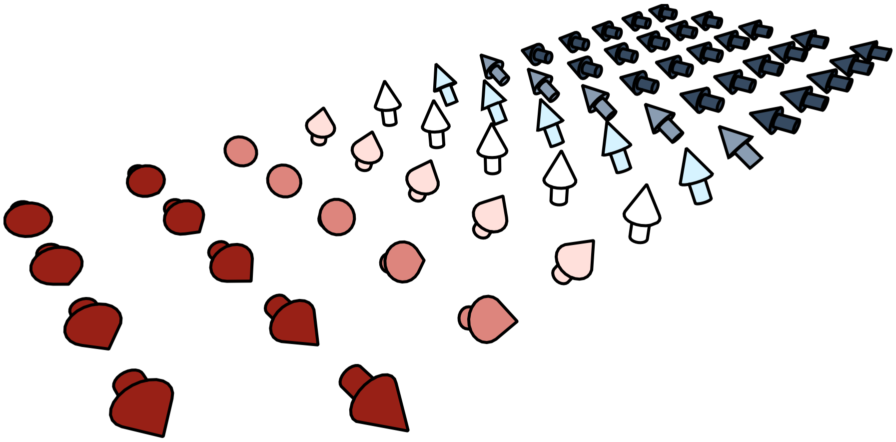

Figure 2.5: Schematics of the Bloch wall: spins rotating between two domains of antiparallel magnetization moving out of the plane.

- *Néel wall*: the rotation of the magnetization occurs in the plain determined by the domain magnetizations, Fig. 2.6. In this case, the energy density is given by

  $$\mathcal{E}_{\mathrm{Nw}} = 4\sqrt{A\left(K + \frac{\mu_0 M_0^2}{2}\right)}, \tag{2.28}$$

  also in the case of uniaxial anisotropy. In this case, however, the demagnetizing energy in the wall has been taken into account.

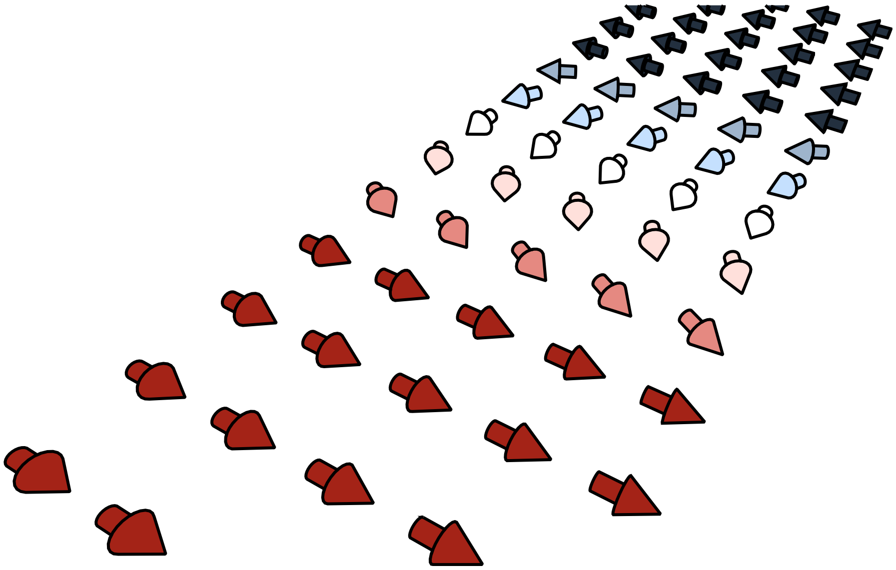

Figure 2.6: Schematics of the Néel wall: spins rotating between two domains of antiparallel magnetization moving in the plane.

Taking into account only Eq. (2.27) and Eq. (2.28), the energy of the Néel wall would always be higher than the energy of the Bloch wall. However, as samples get thinner, the Bloch wall generates free poles on the edges of the sample, and an increasing magnetostatic energy enters into the equation. In addition, the magnetostatic term in Eq. (2.28) decreases. For a certain thickness, the Néel wall is energetically favorable and the magnetization remains in plane [Kurti 1988].

2.4 Magnetization Dynamics

So far, we have seen what determines equilibrium magnetization configuration in magnetic materials. However, magnetization can also be excited dynamically, typically with temperature or with external magnetic fields, and change its static configuration. In this section, we give a general description of this process, and we present the tools to work in this framework.

2.4.1 Landau-Lifshitz Equation

The equation of motion of the magnetization can be derived from both classic and quantum mechanics. In the first case, the restoring force done by a field is treated as a torque acting on the magnetization. Because there are several fields involved, they sum up and act as an effective field. Derivation from quantum mechanics involves the computation

$$i\hbar\dot{\vec{S}} = \left[\vec{S}, \mathcal{H}\right], \tag{2.29}$$

where the right hand side is the commutator of the total Hamiltonian of the system with the spin. This results in the *Landau-Lifshitz equation* (LL) [Chudnovsky and Tejada 2006]:

$$\begin{aligned} \frac{\mathrm{d}\vec{M}(\vec{r},t)}{\mathrm{d}t} &= \gamma\mu_0\left[\vec{M}(\vec{r},t) \times \vec{H}_{\text{eff}}(\vec{r},t)\right], \\ \mu_0\vec{H}_{\text{eff}}(\vec{r}) &= -\frac{\delta E}{\delta\vec{M}}, \end{aligned} \tag{2.30}$$

where the torque is expressed as $\vec{M} \times \vec{H}_{\text{eff}}$ in the first term, and its effect is to force the magnetization rotate around the effective field.

Consequences of the LL Equation: Ferromagnetic Resonance

Let us consider the case of a uniformly magnetized ferromagnet along the Z direction. In this case, the equilibrium magnetization is $\vec{M}_0$, and $\vec{M}(\vec{r})^2 = M_0^2 = \text{const.}$, and Eq. (2.30) takes the solution

$$\begin{aligned} M_x &= M_0 \sin\theta_0 \mathrm{e}^{i\omega_0 t}, \\ M_y &= M_0 \sin\theta_0 \mathrm{e}^{i(\omega_0 t + \pi/2)}, \\ M_z &= M_0 \cos\theta_0, \end{aligned} \tag{2.31}$$

where θ_0 is the angle between the effective field along Z and the magnetization, and

$$\omega_0 = \gamma\mu_0 H_{\text{eff}} \tag{2.32}$$

is the characteristic *ferromagnetic frequency*. In this case, we have considered a uniform magnetization in the body. As a consequence, all spins maintain perfect parallelism during precession. Therefore this kind of oscillation is called the *uniform mode* or *Kittel mode* [Chikazumi et al. 1997; Kittel 1948; 2004], see Fig. 2.7. It occurs in magnetic materials when the precession angles θ_0 are small.

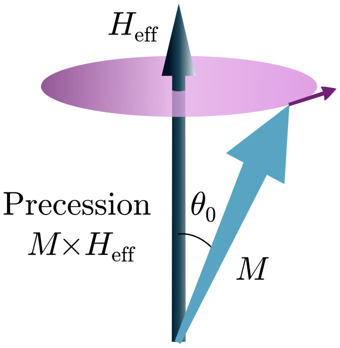

Figure 2.7: Precession of the magnetization at a characteristic frequency ω_0, at an angle θ_0.

Consequences of the LL Equation: Spin Waves

Staying in the uniformly magnetized ferromagnet assumption, limiting to second order anisotropy, we consider the small perturbation of the magnetization $\vec{m}(\vec{r},t)$, such as $\vec{M}(\vec{r},t) = \vec{M}_0 + \vec{m}(\vec{r},t)$, $m \ll M_0$, and $\vec{m}\cdot\vec{M}_0 = 0$. Switching to the Fourier transform of $\vec{m}$,

$$\vec{m}(\vec{r},t) = \frac{1}{(2\pi)^4}\int \mathrm{d}^3q\,\mathrm{d}\omega\,\vec{m}(\vec{q},\omega)\mathrm{e}^{i(\vec{q}\cdot\vec{r}-\omega t)}\,, \tag{2.33}$$

the LL equation (2.30) is then solvable for [Chudnovsky and Tejada 2006]

$$\omega = \gamma\mu_0 M_0\sqrt{\left[\zeta(\vec{q}) - \beta_{xx}^{(\text{eff})}\right]\left[\zeta(\vec{q}) - \beta_{yy}^{(\text{eff})}\right] - \left[\beta_{xy}^{(\text{eff})}\right]^2}\,, \tag{2.34}$$

with

$$\zeta(\vec{q}) = \alpha_{ij}q_iq_j + \beta_{zz}^{(\text{eff})} + \frac{1}{M_0^2}(\vec{H}_0\cdot\vec{M}_0)\,, \tag{2.35}$$

$\beta_{ij}^{(\text{eff})}$ being the effective anistropy tensor, written in the coordinate frame whose z axis coincides with $\vec{M}_0$.

Note that Eq. (2.33) has the form of a wave, and hence this corresponds to the excitations of *spin waves*. When the system rotates at the frequency given by Eq. (2.34) it is called *spin-wave mode* [Chikazumi et al. 1997].

We note here that, in the same approximations made in the derivation of the spin-wave mode, the ferromagnetic frequency corresponds to spin-wave resonance taking $\vec{q} = 0$, which is the gap in spin-wave spectrum.

Figure 2.8 shows the dispersion relation for the case of an effective anisotropy of the form $\beta_{xx} = \beta_{yy} \neq \beta_{zz}$ and $\beta_{ij} = 0$ for $i \neq j$, consisting of an easy axis along the z direction and a hard plane on the xy plane. The case of $\vec{q} = 0$ gives the characteristic ferromagnetic frequency.

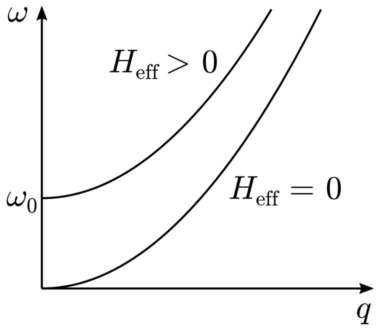

Figure 2.8: Dispersion relation $\omega(q)$ for a diagonal anisotropy tensor with $\beta_{xx} = \beta_{yy}$. When there are no spin waves ($q = 0$), the frequency corresponds to the characteristic ferromagnetic frequency.

In here, spin waves have been derived from the Landau-Lifshitz equation. However, they can also be derived from quantum principles considering excitation in a Heisenberg ferromagnet [Chudnovsky and Tejada 2006].

2.4.2 Landau-Lifshitz Equation with Damping

If one considers the expression of the Landau-Lifshitz equation (2.30), the magnetization would never stop rotating. However, this is not observed in real materials, where one needs to continuously excite the system to keep the rotation. This is taken into account by adding a non-conservative term to Eq. (2.30), known as the *damping* term:

$$\begin{aligned}\frac{\mathrm{d}\vec{M}(\vec{r},t)}{\mathrm{d}t} =&\gamma\mu_0\left[\vec{M}(\vec{r},t)\times\vec{H}_{\mathrm{eff}}(\vec{r},t)\right]\\ &-\eta\frac{\gamma\mu_0}{M_0}\vec{M}(\vec{r},t)\times\left[\vec{M}(\vec{r},t)\times\vec{H}_{\mathrm{eff}}(\vec{r},t)\right],\end{aligned} \tag{2.36}$$

where $\eta < 1$ is the damping constant. Hence, the damping term acts on the magnetization forcing it to the equilibrium position along the effective field.

Note that without a damping term, an external field would not align the magnetization toward the field direction, see Fig. 2.9. It should also be noted that the observation of any resonance is produced by dissipation in the system, which comes from the damping term.

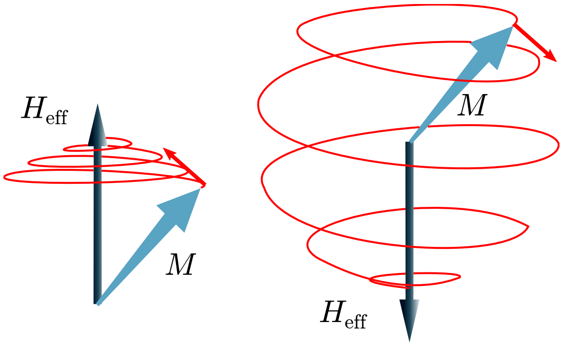

Figure 2.9: Effect of the damping term on the magnetization dynamics, stabilizing the magnetization in the effective field direction.

3

Rotational Doppler Effect in Ferromagnetic Resonance

The Doppler effect in a rotational system is known as the rotational Doppler effect (RDE), and is produced when the emitter and the receiver are in relative rotation. It might seem that the rotational Doppler would shift the ferromagnetic resonance (FMR) in a magnetic system, similar to the blue- or redshift of frequency in the conventional Doppler. However, the rotational Doppler effect in magnetic systems has not been observed. This is due to the fact that the rotation of a magnetic body produces magnetic fields that cancel out the change of the perceived electromagnetic wave. Under some circumstances, however, it might be possible that the rotation produces some shift. We shall use the Landau-Lifshitz equation presented in Chapter 2 to model the magnetization dynamics in a ferromagnetic material. Understanding when the rotational Doppler is produced in a magnetic system could lead to high-resolution spectroscopy, similar to the Mössbauer technique. The rotation of small particles has been observed, for instance, in paramagnetic spectroscopy. Our results indicate that the effect is only produced when the rotating sample has anisotropy. The source of anisotropy could be magnetocrystalline or due to the shape. We also propose some hints to achieve experimental evidence of the rotational Doppler.

3.1 Introduction

The Doppler effect is produced when a receiver and an emitter of radiation move relative to each other. The frequency of the radiation shifts proportional to the velocity of the displacement. We may perceive this effect everyday as we hear an ambulance approaching or leaving. In this classical example, the frequency of the compression waves, that determines the sound we listen, is observed differently depending on the direction of the source: when the ambulance approaches, we observe an increase in the frequency, hence a high-pitched sound. This classical example has its relativistic equivalent when an electromagnetic wave is involved. The Doppler effect is used in satellite communications, speed radars and it has been applied to explain the redshift in the cosmological microwave background and determine that the universe is expanding.

The frequency shift observed by the receiver of electromagnetic radiation may also come from a relative rotation between the source of the electromagnetic radiation and the observer, not just from a purely linear movement. In this case we talk about the RDE [Basistiy et al. 2002; Garetz et al. 1979; Nienhuis 1996]. Figure 3.1 shows schematically the effect. A moving electromagnetic wave is characterized by its frequency $\omega = 2\pi f$, and by the direction of displacement indicated by the wave vector $\vec{k}$. If the observer is rotating at an angular velocity Ω, with the axis of rotation along the wave vector, then the frequency perceived by the receiver ω' will be shifted by

$$\omega' = \omega \pm \Omega, \tag{3.1}$$

where the sign is determined by the relative direction of the helicity of the wave and the direction of rotation of the receiver, the plus (minus) sign determined by opposite (same) sense of rotation.

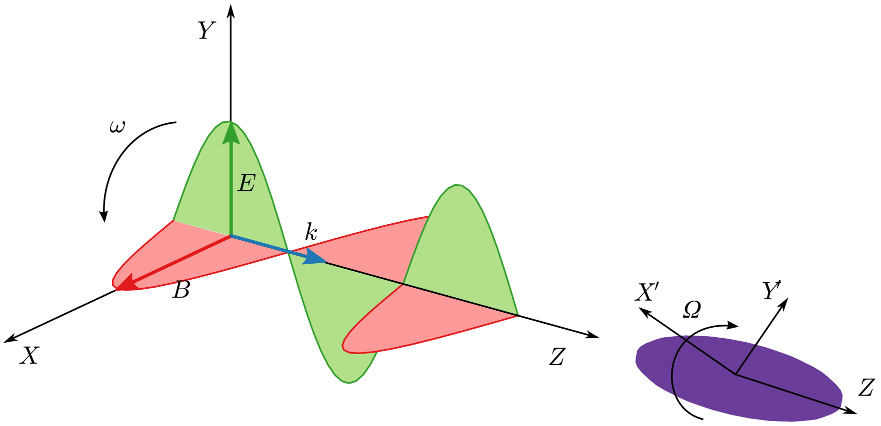

Figure 3.1: Rotational Doppler effect. The frequency ω of the circularly polarized electromagnetic wave $(\omega, \vec{k})$ is the angular velocity of the rotation of the electric (magnetic) field due to the wave at a given point in space. The rotation of the receiver at an angular velocity Ω, depending on the direction of the rotation and the helicity of the wave, adds or subtracts Ω to the frequency of the wave ω, rendering $\omega' = \omega \pm \Omega$ in the coordinate frame of the receiver.

The RDE is less commonly known than the conventional Doppler effect because it is more difficult to observe. In the conventional Doppler, the shift of the frequency, i.e. $\delta\omega/\omega = (\omega' - \omega)/\omega$ is determined by the relative velocity $\delta\omega/\omega = v/c$ for $v \ll c$. Hence the observability of the effect will be determined by the ability to detect such variations, which will increase with the relative velocity between the emitter and the observer. This is one of the limiting factors in the observation of the rotational Doppler, as high angular velocities are not easily achieved. High-speed rotors, such as those used for magic angle spinning in NMR applications or air turbines, can reach angular velocities up to 10 kHz. Let us compare the size of both effects in the Mössbauer technique, which provide a sensitive method for the study of the frequency shift due to conventional Doppler. In this case, the small bandwidth of the gamma radiation $\delta\omega/\omega \sim 10^{-13} - 10^{-12}$ allows a measurable effect even for small velocities of a fraction of a millimeter per second. The high sensitivity of this technique has allowed the measurement of the transverse Doppler effect, consisting of a frequency shift $\delta\omega/\omega = -v^2/(2c^2)$ due to the relativistic time dilation for a receiver moving tangentially with respect to the source of the radiation [Champeney et al. 1961; Hay et al. 1960; Kholmetskii, Yarman, and Missevitch 2008; Kholmetskii, Yarman, Missevitch, and Rogozev 2009; Kündig 1963]. In order to achieve measurements displacements of $\sim 10^{-13} - 10^{-12}$ with the RDE, the angular velocity between the emitter and the receiver should be $\sim$ 1 – 10 MHz, which is far from the highest achievable speed rotations.

Let us consider a circularly polarized electromagnetic wave propagating in the Z axis, as shown in Fig. 3.1. A body rotating around the same axis perceives the frequency of the electromagnetic wave according to Eq. (3.1). The resonance condition is then $\omega_{\text{res}} = \omega'$, with ω_{res} the characteristic frequency of the system. However, the mechanical rotation of a system of charges is equivalent to a magnetic field—the Larmor theorem [Landau et al. 1975]—and the characteristic frequency on the rotating system, ω'_{res}, might be affected. Resonant frequencies of LC circuits are insensitive to magnetic fields, where as the frequency of a receiver based upon magnetic resonance would be sensitive to the fictitious magnetic field due to rotation. The Doppler shift in rotating LC circuits has been tested by the GPS for the case of a receiving antenna making as little as 8 revolutions per second as compared to the carrier frequency of the electromagnetic waves in the GHz range [Ashby 2003].Eq. (3.1) has been also applied to the explanation of the frequency shift encountered by NASA in the communications with Pioneer spacecrafts [Anderson et al. 2003]. One essential difference between conventional and rotational Doppler effects is that the first refers to the inertial systems while the second occurs in the non-inertial systems. This prompted works that considered RDE in the context of nonlocal quantum mechanics in an accelerated frame of reference [Mashhoon 1993]. Relativity (or Galilean invariance for $v \ll c$) makes the conventional Doppler effect universal. Due to the magnetic field generated through the Larmor theorem, such a universality should not be expected for the RDE.

The RDE frequency shift caused by a rotating plate inserted into a beam of circularly polarized light was reported in Refs. [Basistiy et al. 2002; Bretenaker et al. 1990; Chen et al. 2008; Garetz et al. 1979; Simon et al. 1988]. The RDE was predicted for rotating light beams [Nienhuis 1996] and subsequently observed using millimeter waves [Courtial et al. 1998] as well as in the optical range [Barreiro et al. 2006] (see [Padgett 2006] for review). In solid-state experiments the Doppler effect has been used to explain the current-induced spin-wave frequency shift produced in a thin ferromagnetic layer [Vlaminck et al. 2008], and the spin-rotation coupling has also been used to argue for current generation from a rotation [Ieda et al. 2014], but the RDE has proved elusive. Frequencies of the FMR are typically in the GHz range or higher, which is far above achievable angular velocities of mechanical rotation of macroscopic magnets. However, small magnetic particles in beams [Xu et al. 2005] or in nanopores [Tejada, Zysler, et al. 2010] may rotate very fast. Equation (3.1) was applied to the analysis of the observed anomalies in the FMR data on rotating nanoparticles [Tejada, Zysler, et al. 2010].

However, a theory for the effect of rotation in the different magnetic resonances was never developed. By analyzing the Landau-Lifshitz equation [Eq. (2.36)] introducing the effect of a circularly polarized magnetic field, we find an expression for the shift of the FMR. Furthermore, we compute the absorbed power by the rotating magnet taking into account the dissipation of the magnet in a linearly polarized magnetic field.

3.2 Background

3.2.1 Spin in a Rotating Frame of Reference

In classical mechanics the Hamiltonian of a system in a rotating coordinate frame is given by [Landau et al. 1982]

$$\mathcal{H}' = \mathcal{H} - \vec{L} \cdot \vec{\Omega} \,. \tag{3.2}$$

Here $\mathcal{H}$ is the Hamiltonian at $\Omega = 0$ and $\vec{L}$ is the mechanical angular momentum of the system. For a system of charges one can write

$$\vec{L} = \frac{\vec{\mu}}{\gamma} \,, \tag{3.3}$$

where $\vec{\mu}$ is the magnetic moment and γ is the gyromagnetic ratio. Eq. (3.2) then becomes equivalent to the Hamiltonian,

$$\mathcal{H}' = \mathcal{H} - \vec{\mu} \cdot \vec{B} \,, \tag{3.4}$$

in the fictitious magnetic field,

$$\vec{B} = \frac{\vec{\Omega}}{\gamma}\,, \tag{3.5}$$

which is the statement of the Larmor theorem [Landau et al. 1975].

Classical mechanics and classical field theory do not deal with the concept of a spin. The question is then whether Eq. (3.2) should contain spin $\vec{S}$ alongside the orbital angular momentum $\vec{L}$. Eq. (3.4) hints that since the magnetic moment can be of spin origin this should be the case. Also, the generator of rotation, according to relativistic physics, is

$$\vec{J} = \vec{L} + \vec{S}\,. \tag{3.6}$$

Therefore, it should be expected that in the presence of a spin Eq. (3.2) should be generalized as

$$\mathcal{H}' = \mathcal{H} - (\vec{L} + \vec{S}) \cdot \vec{\Omega}\,. \tag{3.7}$$

In quantum theory this relation can be rigorously derived in the following way. Rotation by an angle $\vec{\phi}$ transforms the Hamiltonian of an isolated system into [Messiah 1976]

$$\hat{\mathcal{H}}' = \exp\left[\frac{i}{\hbar}(\vec{L} + \vec{S}) \cdot \vec{\phi}\right] \hat{\mathcal{H}} \exp\left[-\frac{i}{\hbar}(\vec{L} + \vec{S}) \cdot \vec{\phi}\right]\,. \tag{3.8}$$

To the first order on a small rotation $\vec{\phi}$ one obtains

$$\hat{\mathcal{H}}' = \hat{\mathcal{H}} - \frac{i}{\hbar}(\vec{L} + \vec{S}) \cdot [\hat{\mathcal{H}}, \vec{\phi}]\,, \tag{3.9}$$

where we have taken into account that for an isolated system $\vec{J}$ is conserved, i.e. $\vec{L}+\vec{S}$ commutes with $\hat{\mathcal{H}}$. This equation becomes Eq. (3.7) if one takes into account the quantum-mechanical relation

$$\vec{\Omega} = \frac{d\vec{\phi}}{dt} = \frac{i}{\hbar}[\hat{\mathcal{H}}, \vec{\phi}] \tag{3.10}$$

and replaces operator $\vec{\Omega}$ by its classical expectation value. For an electron, Eq. (3.7) can be also formally derived as a non-relativistic limit of the Dirac equation written in the metric of the rotating coordinate frame [Hehl et al. 1990]. The answer for the corresponding Schrödinger equation reads

$$i\hbar\frac{\partial\Psi}{\partial t} = \hat{\mathcal{H}}'\Psi\,, \quad \hat{\mathcal{H}}' = \frac{\hat{\vec{p}}^2}{2m} - \left(\vec{r} \times \hat{\vec{p}} + \frac{1}{2}\hbar\hat{\vec{\sigma}}\right) \cdot \vec{\Omega}\,, \tag{3.11}$$

where $\vec{r}$ is the radius-vector of the electron, $\vec{p} = -i\hbar\vec{\nabla}$ is the linear momentum of the electron, and $\sigma_{x,y,z}$ are Pauli matrices.

The term $-\vec{S}\cdot\vec{\Omega}$ in the Hamiltonian has lead to some discussion by researchers. They have discussed its meaning in the coordinate frame that rotates together with the body [Chudnovsky 1994; Chudnovsky, Garanin, and Schilling 2005; Hartmann-Boutron et al. 1996]. To elucidate the physical meaning of this term, let us consider the resulting equation of motion for a classical spin-vector [Chudnovsky and Tejada 2006]

$$\frac{\mathrm{d}\vec{S}}{\mathrm{d}t} = -\vec{S}\times\frac{\delta\mathcal{H}'}{\delta\vec{S}}\,. \tag{3.12}$$

We see from this equation that the spin cannot be affected by the rotation of the body unless $\mathcal{H}$ contains coupling of the spin to an internal vector of the crystal ($\delta\mathcal{H}'/\delta\vec{S}\neq 0$). In this case $\delta\mathcal{H}'/\delta\vec{S} = -\vec{\Omega}$ and Eq. (3.12) simply describes the precession of $\vec{S}$ about $\vec{\Omega}$:

$$\frac{\mathrm{d}\vec{S}}{\mathrm{d}t} = \vec{S}\times\vec{\Omega}\,. \tag{3.13}$$

It shows how a constant vector $\vec{S}$ is viewed by an observer rotating at an angular velocity $\vec{\Omega}$. This has nothing to do with the spin-orbit or any other interaction. Such interactions should be accounted for in the $\hat{\mathcal{H}}$ part of the Hamiltonian $\hat{\mathcal{H}}'$. The effect of rotations on ferromagnetic resonance is considered in the next sections.

3.3 Calculations for the Rotational Doppler Effect in FMR

3.3.1 Frequency Shift of the FMR due to Rotation

Let us consider the effect of the rotation on a ferromagnet. Using the ferromagnetic model studied by Kittel [Kittel 1948], we shall assume a macrospin in an external magnetic field $\vec{B}=\mu_0\vec{H}$. We consider a body with an ellipsoidal shape and uniform magnetization M_S, and neglect magnetocrystalline anisotropy. The Hamiltonian of this system is hence determined by the Zeeman interaction with the external field and by the dipolar term. The exchange term does not enter in the Hamiltonian, as we are considering that the system is composed of a big macrospin. Hence, the Hamiltonian of such a system can be written as

$$\mathcal{H} = \mu_0\left[\sum_{i,j=x,y,z}\frac{1}{2}N_{ij}M_iM_j - \vec{M}\cdot\vec{H}\right]. \tag{3.14}$$

We have used the same notation as in Chapter 2, where $\vec{M}$ is the magnetization and N_{ij} is the tensor of demagnetizing coefficients, its principal axes coinciding with those of the ellipsoid.

In the macrospin model, the magnetization remains constant, and if we choose a coordinate system with axes coinciding with the principal axes, then the relation

$$\vec{M}^2 = M_x^2 + M_y^2 + M_z^2 = M_\mathrm{S}^2 \tag{3.15}$$

holds, and the Hamiltonian of Eq. (3.14) can be written as

$$\mathcal{H} = -\mu_0 \left[\frac{1}{2}(N_x - N_z)M_x^2 + \frac{1}{2}(N_y - N_z)M_y^2 + \vec{M} \cdot \vec{H} \right] \tag{3.16}$$

up to an unessential constant. An ellipsoid with the long axis in the Z direction is characterized by $(N_x - N_z) > 0$ and $(N_y - N_z) > 0$, and hence the stable magnetization points in the Z direction. We consider the case of a magnetic field applied along the Z direction, which makes the stable magnetization to remain in the same direction. In a real sample, a field is needed to keep the ferromagnet from breaking into domains.

In this case, the FMR frequency ω_FMR can be obtained linearizing the Landau-Lifshitz equation

$$\frac{\mathrm{d}\vec{M}}{\mathrm{d}t} = \gamma \vec{M} \times \vec{B}_\mathrm{eff} \,, \tag{3.17}$$

around the equilibrium position $\vec{M} = M_\mathrm{S}\vec{e}_z$. The resulting effective field is

$$\begin{aligned} \vec{B}_\mathrm{eff} &= -\frac{\delta \mathcal{H}}{\delta \vec{M}} \\ &= \mu_0 \left[(N_x - N_z)M_x + (N_y - N_z)M_y + \vec{H} \right] \,, \end{aligned} \tag{3.18}$$

and the result of the linearization can be written as

$$\omega_\mathrm{FMR} = \sqrt{\omega_x \omega_y} \,, \tag{3.19}$$

with

$$\begin{aligned} \omega_x &= |\gamma| \mu_0 M_\mathrm{S} \left[(N_x - N_z) + \frac{H}{M_\mathrm{S}} \right] \\ \omega_y &= |\gamma| \mu_0 M_\mathrm{S} \left[(N_y - N_z) + \frac{H}{M_\mathrm{S}} \right] \,. \end{aligned} \tag{3.20}$$

If we now take into account the effect of a rotation around the Z axis at an angular velocity Ω as an effective field $\vec{B} = \vec{\Omega}/\gamma$ in the rotating frame, and add it to the Hamiltonian of Eq. (3.14), the result is

$$\begin{aligned} \mathcal{H}' &= \mathcal{H} - \vec{M} \cdot \frac{\vec{\Omega}}{\gamma} \\ &= -\mu_0 \left[\frac{1}{2}(N_x - N_z)M_x^2 + \frac{1}{2}(N_y - N_z)M_y^2 - \vec{M} \cdot \left(\vec{H} + \frac{\vec{\Omega}}{\gamma \mu_0} \right) \right] \,. \end{aligned} \tag{3.21}$$

As the effect of the rotation is an effective field, the expression of the resonant frequency in the rotating frame ω'_{FMR} is

$$\omega'_{\mathrm{FMR}} = \sqrt{\omega'_x \omega'_y}\,, \tag{3.22}$$

with

$$\begin{aligned} \omega'_x &= |\gamma|\mu_0 M_{\mathrm{S}} \left[(N_x - N_z) + \frac{H}{M_{\mathrm{S}}} + \frac{\Omega}{\gamma\mu_0 M_{\mathrm{S}}} \right] \\ \omega'_y &= |\gamma|\mu_0 M_{\mathrm{S}} \left[(N_y - N_z) + \frac{H}{M_{\mathrm{S}}} + \frac{\Omega}{\gamma\mu_0 M_{\mathrm{S}}} \right] . \end{aligned} \tag{3.23}$$

In the case of a symmetric ellipsoid $N_x = N_y$, the shift on the ferromagnetic resonance is

$$\omega'_{\mathrm{FMR}} = \omega_{\mathrm{FMR}} - \Omega\,, \tag{3.24}$$

so that the RDE frequency shift determined by the equation $\omega' = \omega - \Omega = \omega'_{\mathrm{FMR}}$ is exactly zero. For an asymmetric ellipsoid ($N_x \neq N_y$), expanding Eq. (3.22) into a series on Ω one obtains to the first order

$$\omega'_{\mathrm{FMR}} = \omega_{\mathrm{FMR}} - \kappa\Omega\,, \tag{3.25}$$

with

$$\kappa = \frac{1}{2}\left(\sqrt{\frac{\omega_x}{\omega_y}} + \sqrt{\frac{\omega_y}{\omega_x}} \right) , \tag{3.26}$$

and $\kappa \geq 1$.

At large fields, $B \gg \mu_0 M_{\mathrm{S}}$, equations (3.20) and (3.26) give $\kappa \to 1$, that is, no frequency shift due to the RDE. Sizable frequency shift of the FMR observed in the laboratory frame due to the rotation of the sample should occur only at B not significantly exceeding $\mu_0 M_{\mathrm{S}}$ and only in a sample lacking the rotational symmetry.

One can generalize the above approach to take into account any type of magnetocrystalline anisotropy. The formulas look especially simple in the case of second-order anisotropy. Such anisotropy adds the term

$$\mathcal{H}_{\mathrm{A}} = -\sum_{i,j=x,y,z} \frac{1}{2}\mu_0 \beta_{ij} M_i M_j \tag{3.27}$$

to the Hamiltonian of the magnet, with β_{ij} being some dimensionless symmetric tensor. Consider, e.g., an orthorhombic crystal whose axes (a, b, c) coincide with the axes of the ellipsoid and whose easy magnetization axis, c, is parallel to the Z direction. In this case all the above formulas remain valid if one replaces the demagnetizing factors with

$$N'_i = N_i - \beta_i\,, \quad i = x, y, z\,, \tag{3.28}$$

where β_x, β_y, and β_z are the principal values of β_{ij}. Due to the orthorhombic anisotropy ($a \neq b \to \beta_x \neq \beta_y$) the RDE may now occur even in a sample of rotationally invariant shape ($N_x = N_y$).

3.3.2 Power Absorption by a Rotating Magnet

For non-relativistic rotations the radiation power absorbed by a magnet should be the same in the laboratory frame and in the rotating frame. Calculation in the rotating frame is easier. We shall assume that the dimensions of the sample are small compared to the wavelength of the radiation, so that the field of the wave at the position of the ferromagnet is nearly uniform. The geometry studied below is illustrated in Fig. 3.2.

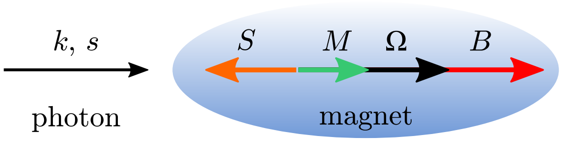

Figure 3.2: Geometry of the FMR in study. A ferromagnet uniformly magnetized by a static magnetic field, $\vec{B}$, is rotating at an angular velocity $\vec{\Omega}$ in the radiation field of circularly polarized photons of wave vector $\vec{k}$ and spin $\vec{s}$. (Due to the negative gyromagnetic ratio, the equilibrium spin of the magnet, $\vec{S}_0$, is antiparallel to its equilibrium magnetic moment $\vec{M}_{\mathrm{S}}$.)

Within the model of Eq. (3.21), a rotating magnet placed in the field of a circularly polarized wave feels an oscillating magnetic field that can be represented by a complex function

$$h(t) = h_0 e^{\pm i\omega' t}\,, \quad \omega' = \omega \mp \Omega \tag{3.29}$$

giving the components of the field as

$$h_x = \mathrm{Re}(h),\ h_y = \mathrm{Im}(h)\,. \tag{3.30}$$

Here h_0 is the complex amplitude of the wave, the $\pm$ sign in Eq. (3.29) determines the helicity of the wave, while the sign of Ω determines the direction of rotation of the magnet. Due to the wave the magnetization acquires a small ac component $m(t)$ (whose real part represents m_x and whose imaginary part represents m_y),

$$m(t) = \hat{\chi}(\omega) h(t)\,, \tag{3.31}$$

where $\hat{\chi}$ is the susceptibility tensor. The absorbed power is given by [Chudnovsky and Tejada 2006]

$$P = \pm i \mu_0 \omega' h_0^* (\hat{\chi} - \hat{\chi}^\dagger) h_0\,. \tag{3.32}$$

The problem has, therefore, reduced to the computation of the susceptibility in the rotating frame. The computation can be done by solving the Landau-Lifshitz equation,

$$\frac{\mathrm{d}\vec{M}}{\mathrm{d}t} = \gamma \vec{M} \times \vec{B}_{\mathrm{eff}} - \frac{\eta}{M_{\mathrm{S}}}|\gamma|\vec{M} \times \left[\vec{M} \times \vec{B}_{\mathrm{eff}}\right] , \tag{3.33}$$

in the rotating frame, that is, with $\vec{B}_{\mathrm{eff}} = -\delta\mathcal{H}'/\delta\vec{M}$ and

$$\mathcal{H}' = \mathcal{H} - \vec{M} \cdot \frac{\vec{\Omega}}{\gamma} - \vec{M} \cdot \vec{h} \, . \tag{3.34}$$

The parameter η in Eq. (3.33) is a dimensionless damping coefficient that is responsible for the width of the FMR in the absence of inhomogeneous broadening.

Substituting $\vec{M} = M_{\mathrm{S}}\vec{e}_z + \vec{m}$ into Eq. (3.33) and solving for $\hat{\chi}$ one obtains for the power

$$P_{\pm} = \frac{1}{2}\eta|\gamma|M_{\mathrm{S}}\mu_0^2|h_0|^2 f_{\pm}(\omega') \, , \tag{3.35}$$

where

$$f_{\pm} = \frac{\omega'^2[2(\omega'^2 - \omega'^2_{\mathrm{FMR}}) \pm 2\omega'(\omega'_x + \omega'_y) + (\omega'_x + \omega'_y)^2]}{(\omega'^2 - \omega'^2_{\mathrm{FMR}})^2 + \eta^2\omega'^2(\omega'_x + \omega'_y)^2} \, . \tag{3.36}$$

Notice that when there is full rotational symmetry, $\omega'_x = \omega'_y = \omega'_{\mathrm{FMR}}$, the absorbed power at the resonance is non-zero only for one polarization of the wave that corresponds to the upper sign in Eqs. (3.29) and (3.36). This is a consequence of the selection rule due to conservation of the Z-component of the total angular momentum (absorbed photon + excited magnet).

Let us now consider a rotating ferromagnet in the radiation field of a linearly polarized electromagnetic wave. In the rotating frame the complex magnetic field of such a wave is

$$h(t) = \frac{h_0}{2}\left[e^{i(\omega-\Omega)t} + e^{-i(\omega+\Omega)t}\right] = h_0 e^{-i\Omega t}\cos(\omega t) \, . \tag{3.37}$$

Repeating the above calculation, one obtains for the power averaged over the period of rotation

$$P = \frac{1}{8}\eta|\gamma|M_{\mathrm{S}}\mu_0^2|h_0|^2\left[f_{+}(\omega - \Omega) + f_{-}(\omega + \Omega)\right] \, . \tag{3.38}$$

When the rotational symmetry of the magnet is broken, $\omega_x \neq \omega_y$, $\kappa > 1$, the absorption has two maxima of uneven height at

$$\omega = \omega_{\mathrm{FMR}} - (\kappa \mp 1)\Omega \, . \tag{3.39}$$

As the rotational symmetry is gradually restored, $\omega_x \to \omega_y$, $\kappa \to 1$, the rotational shift in the position of the main maximum disappears. In that limit the shift in the position of a smaller maximum approaches 2Ω while the height of that maximum goes to zero, see Fig. 3.3.

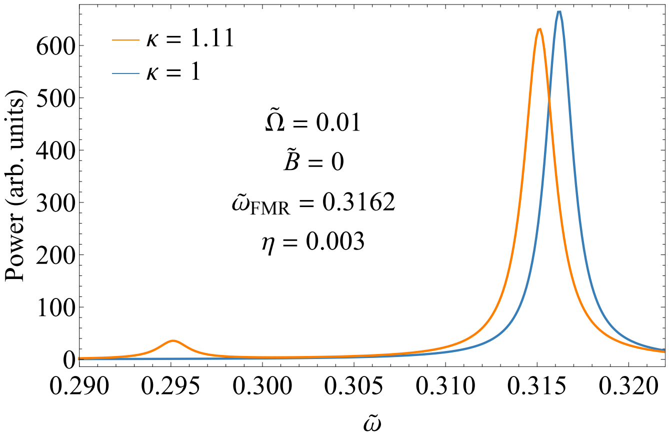

Figure 3.3: Absorption of power of linearly polarized electromagnetic radiation by a rotating magnet. Frequencies are given in the units of $\gamma\mu_0 M_{\mathrm{S}}$. As the rotational symmetry is violated the FMR becomes shifted and the second FMR line emerges separated by 2Ω from the first line.

3.3.3 Discussion

We have computed the frequency shift of the FMR due to rotation of the sample. We found that it is, in general, different from the rotational Doppler effect reported in other systems [Padgett 2006]. The differences stem from the observation that the spin of an electron or an atom would be insensitive to the rotation of the body as whole in absence of the relativistic spin-orbit coupling. Even taking into account spin-orbit interactions the spin would not simply follow the rotation of the body but would exhibit more complex behavior described by the dynamics of the angular momentum. This behavior is similar to a classical gyroscope in a rotating frame.

We found the following features in the FMR of a rotating sample.

- If the spin Hamiltonian is invariant with respect to the rotation, then the rotation of the body has no effect on the frequency of the resonant absorption of a circularly polarized electromagnetic wave.
- As the rotational invariance is violated, the absorption line shifts. The shift is different from the angular velocity of the rotation Ω. It depends on the degree of violation of the rotational symmetry. The frequency shift goes to zero when the symmetry is restored.
- In the case of a linearly polarized radiation, a second resonance line emerges separated by 2Ω from the first line. The intensity of that line depends on the

degree of violation of rotational symmetry. It disappears when the rotational symmetry is restored.

FMR measurements are usually performed in the GHz range, with the width of the resonance being sometimes as low as a few MHz. Currently available small mechanical rotors can rotate as fast as 100 kHz, which, nevertheless, is still low compared to the linewidths of FMR. Note, however, that the position of the FMR maximum can be determined with an accuracy of a few hundred kHz. It is then not out of question that under appropriate conditions the RDE frequency shift and the splitting of the resonance can be observed in high precision FMR experiments even when the rotation frequency is significantly lower than the linewidth. Since anisotropy of the sample is needed to provide rotational asymmetry, the measurements should be performed on single crystals. When the magnetocrystalline anisotropy is weak, the RDE in FMR can be induced by the asymmetric shape of the sample alone due to the anisotropy of dipole-dipole interactions. Even in this case, however, a single crystal would be preferred to provide a narrow linewidth.

Recent FMR experiments in magnetic nanoparticles embedded in nanopores have suggested that the particles are free to rotate at great velocities [Tejada, Zysler, et al. 2010]. An analytical solution of the quantum-mechanical rotator does not exist. Chudnovsky and Garanin [2010] found a low energy solution of a quantum spin interacting with mechanical rotation by treating the spin system as a two-level system. For a larger spin, the solution is more difficult to obtain. In [Tokman et al. 2015] the mechanical rotation of a nanomagnet interacting with an electromagnetic wave is treated from quantum mechanics. As in the case of the experiment in [Tejada, Zysler, et al. 2010], the nanoparticles consist of a large number of atoms, and hence a semiclassical approximation $\vec{\Omega} \sim \vec{L}/I$ holds (I being the moment of inertia). This suggests that the magnetic resonance would split into many levels corresponding to the quantization of $\vec{L}$. This approximation was indeed used to explain the results. In such systems, the RDE would become important. Measurements of single magnetic nanoparticles [Bogani et al. 2008] may show greater quantized rotational states and, as a consequence, splitting on the spin resonance.

3.4 Conclusions

In this chapter we have studied the effect of an electromagnetic wave on a ferromagnet. In particular we have used the Landau-Lifshitz equation to the case of a rotating ferromagnet, we have obtained a general expression for the characteristic ferromagnetic resonance and the absorbed power. The results show that, in order to observe a Doppler shift due to rotation, the system must be anisotropic. Even in samples without crystalline anisotropy, the shape of the sample could provide the needed anisotropy. The rotational Doppler would become visible when a linearly polarized electromagnetic wave is sent to a rotating ferromagnet. The absorption spectra is expected to show an emerging peak displaced by 2Ω, besides the shift of the main peak. The effect increases with the speed rotation and with increasing anisotropy, so high anisotropic materials and high speed rotations would favor the observation of the effect. Even though such high rotations are difficult to obtain, the effect could be visible in free-rotating systems that can achieve high rotation speeds.

4

Resonant Spin Tunneling in Single-Molecule Magnets

Single-molecule magnets are compounds formed by interacting metallic and organic atoms as building blocks. What makes these molecular compounds interesting is that each molecule displays a tiny interaction with neighboring molecules, thus exhibiting quantum features even in macroscopic experiments, such as *macroscopic quantum tunneling* (MQT). The advantage of single-molecule magnets over ensembles of particles is that a macroscopic sample is composed by a large number of identical molecules, and hence one can characterize the macroscopic sample by the set of parameters of the molecule. This allowed the quantitative evidence of resonant MQT in single-molecule magnets. However, fabrication of single-molecule magnets may be complicated, and the measurement of the quantum behavior typically needs special preparation of the sample. In this chapter, we study randomly oriented particles of the single-molecule magnet Mn_{12}-Acetate (Mn_{12} hereafter). Observing the features of quantum behavior at the macroscopic level of randomly oriented samples of single-molecule magnets may significantly reduce the effort to characterize newly synthesized compounds. Additionally, nanoparticles of Mn_{12} embedded in a matrix could act as free rotors and, at the same time, have quantum effects. We have performed macroscopic measurements of the magnetization in randomly oriented samples. Interestingly, we have observed quantum features in the magnetization curves, showing that the resonant quantum tunneling can also be observed in non-oriented systems.

4.1 Introduction

Since the discovery of resonant spin tunneling in Mn_{12} acetate [Friedman et al. 1996], researchers have generally believed that at the macroscopic level the effect can only be observed in a single crystal or in the array of microcrystallites with aligned crystallographic axes. Del Barco et al. [1999], Friedman et al. [1996], Hernandez, Torres, et al. [2002], Hernàndez et al. [1996], Hernandez, X. X. Zhang, et al. [1997], and Sales et al. [1999] aligned the microcrsytallites with high magnetic fields and the microcrystallites were fixed when the temperature decreased. This method is easier than obtaining single crystals of single-molecule magnets large enough to observe the resonant spin tunneling [Thomas et al. 1996]. Single crystals of Fe_8 were used to observe the crossing of levels as the field is swept, which allows tunneling with a probability given by the Landau-Zener formula, producing a varying rate of transition [Wernsdorfer et al. 1999]. Other characteristic features from quantum tunneling observed in single crystals include magnetic deflagration [Hernández-Mínguez et al. 2005; Subedi et al. 2013; Suzuki et al. 2005], which is produced when the system is brought to metastability and nearly all spins tunnel to the most stable state in a short time, and Rabi oscillations [Bertaina et al. 2008; Schlegel et al. 2008], produced by the cycling between states modulated at the resonant fields. More recently, experiments with individual magnetic molecules bridged between conducting leads and molecules grafted on carbon nanotubes have been performed and readout of quantum states of individual atomic nuclei has been achieved [Ganzhorn et al. 2013a; b]. However, this fabrication process is challenging. Quantum superposition of spin states in magnetic molecules makes them candidates for qubits—elements of quantum computers [Tejada, Chudnovsky, et al. 2001].

Nowadays a large number of new single-molecule magnets are synthesized by chemists every year and subsequently tested by physicists for the presence of spin tunneling. In many cases growing a sufficiently large single crystal is a challenging task as compared to growing microcrystals. At the same time, the effectiveness of the room-temperature alignment of microscrystals by a high-magnetic field in, e.g., an epoxy strongly depends on the shape of the crystallites and may also be incompatible with their chemistry. Hence finding a fast way to characterize the magnetic molecules would be advantageous.

Mn_{12} nanoparticles were first measured in [Carbonera et al. 2008; Imaz et al. 2008], where peaks in $\mathrm{d}M/\mathrm{d}H$ were observed and attributed to quantum tunneling. However, such observation in a disordered sample has not been explained. Zero-field cooled (ZFC) magnetization curve of the samples revealed large, up to 40 %, fraction of fast-relaxing species of Mn_{12}. This resulted in a complicated pattern of displaced tunneling maxima as compared to typical resonances in a Mn_{12} crystal with a separation of about 460 mT. This minority species consist of some molecules inside the crystal having a lower energy barrier and, hence, a lower T_B.

Our goal is to give explanation to those kind of maxima, and to further study the possiblity to obtain evidence of quantum tunneling in non-oriented samples.

Our samples consist of highly amorphous Mn_{12} nanoparticles. We characterize the synthesized nanoparticles with a variety of methods. First, we take scanning and transmission electron microscopy (SEM and TEM) images of the nanoparticles to determine the size uniformity and shape of the particles. The magnetic measurements were performed in a MPMS® SQUID magnetometer, which allows us to measure the magnetic moment of a sample at magnetic fields up to 5 T and temperatures down to 1.8 K. The magnetic moment can be measured as a function of both the magnetic field and the temperature. Moreover, the ac susceptibility can also be measured with this system.

Our measurements show evidence of spin tunneling in macroscopic magnetic measurements of single-molecule magnets. This is in contrast to previous works, in which researchers measured macroscopic single crystals or aligned the microcrystals. We observe spin tunneling by simply measuring the magnetization curve $M(H)$, and plotting the derivative of the magnetic moment with respect to the magnetic field, $\mathrm{d}\mu/\mathrm{d}H$. To illustrate this point we use amorphous nanospheres of Mn_{12} [Carbonera et al. 2008; Imaz et al. 2008]. Such nanospheres do not form crystals and cannot align with the easy magnetization axes of Mn_{12} molecules in a high magnetic field because of their isotropic magnetic susceptibility.

4.2 Background

4.2.1 Single-Molecule Magnets

Single-Molecule Magnets (SMMs) are compounds formed by ferromagnetic atoms bonded through organic ligands [Bartolomé et al. 2014]. The molecules are composed by several interacting ferromagnetic atoms, that produce a large total spin of $S \sim 10$ on each molecule. Due to the organic environment, molecules are isolated from each other and interact weakly only through long-range dipolar fields. They can be treated as ensembles of non-interacting macrospins. A large number of molecules form a crystal with a symmetry determined by the symmetry of the molecule. This makes it possible to treat each single molecule as a single domain, and the exchange interaction has the effect of keeping a uniform rotation of the spins with respect to the anisotropy axis, instead of individual rotation of spins. This keeps the magnetization uniform

$$M_x^2 + M_y^2 + M_z^2 = M_\mathrm{S}^2 = \text{const.}, \tag{4.1}$$

and hence the system can be described with a single spin Hamiltonian in presence of an applied field. Hence a crystal of a single molecule, despite the large spin of the molecule, has a small macroscopic spin equivalent to the spin of the molecule, and the magnetic behavior of the macroscopic crystal reflects the behavior of a single molecule.

Some of the most known SMMs are [Christou et al. 2000]:

- $[Mn_{12}O_{12}(CH_3COO)_{16}(H2O)_4]$, known as Mn_{12} or Mn_{12} Acetate.
- $[Fe_8O_2(OH)_{12}(tacn)_6]Br_8$, known as Fe_8.
- $[Mn_4O_3Cl(O_2CCH_3)_3(dbm)_3]$, known as Mn_4.
- $[Fe_4(OH)_6(dpm)_3]$, known as Fe_4.

4.2.2 Mn_{12} Hamiltonian

The molecule $[Mn_{12}O_{12}(CH_3COO)_{16}(H2O)_4]$ exhibits a *superparamagnetic* behavior above the *blocking temperature*, see below. The atoms in this molecule are arranged in two structures: an outer ring of 8 Mn(III) atoms, each with spin $S_{\mathrm{Mn(III)}} = 2$, and an inner smaller core structure with 4 Mn(IV), each with spin $S_{\mathrm{Mn(IV)}} = 3/2$. Each structure is ferromagnetically coupled, which produces a total spin of $S_{\mathrm{ring}} = 16$ for the ring and $S_{\mathrm{core}} = 6$ for the core. The spins of the ring and the core are antiferromagnetically aligned, producing a total effective single domain macrospin $S = 10$, see Fig. 4.1, with the easy axis along the flat, c axis [Lis 1980].

The Mn_{12} Hamiltonian, with the molecule having a uniaxial anisotropy with the easy axis along the Z direction, can be written as [Politi et al. 1995]

$$\mathcal{H} = -DS_z^2 - \vec{h} \cdot \vec{S} = -DS_z^2 - h_z S_z + \mathcal{H}_\perp, \tag{4.2}$$

where $\vec{h} = \gamma\hbar\mu_0\vec{H}$ is the magnetic field, and S_z the projection of the spin along the easy axis. In the second equality, we have divided the Hamiltonian in the parts that commute with S_z (first two terms), and a transverse Hamiltonian (last term).

4.2.3 Superparamagnetism and Blocking Temperature

We can see from Eq. (4.2) that there are two energy minima at zero field, separated by an energy barrier equal to DS^2. In such systems, the spins can jump between the two energy minima, with a characteristic flipping time that follows an Arrhenius law

$$t_{\mathrm{f}} = t_0 \exp\left[\frac{U(H)}{k_{\mathrm{B}}T}\right], \tag{4.3}$$

where $U(H)$ is the energy barrier, and t_0 the *microscopic attempt time* [Chudnovsky and Tejada 1998]. From this equation it follows that magnetization cannot

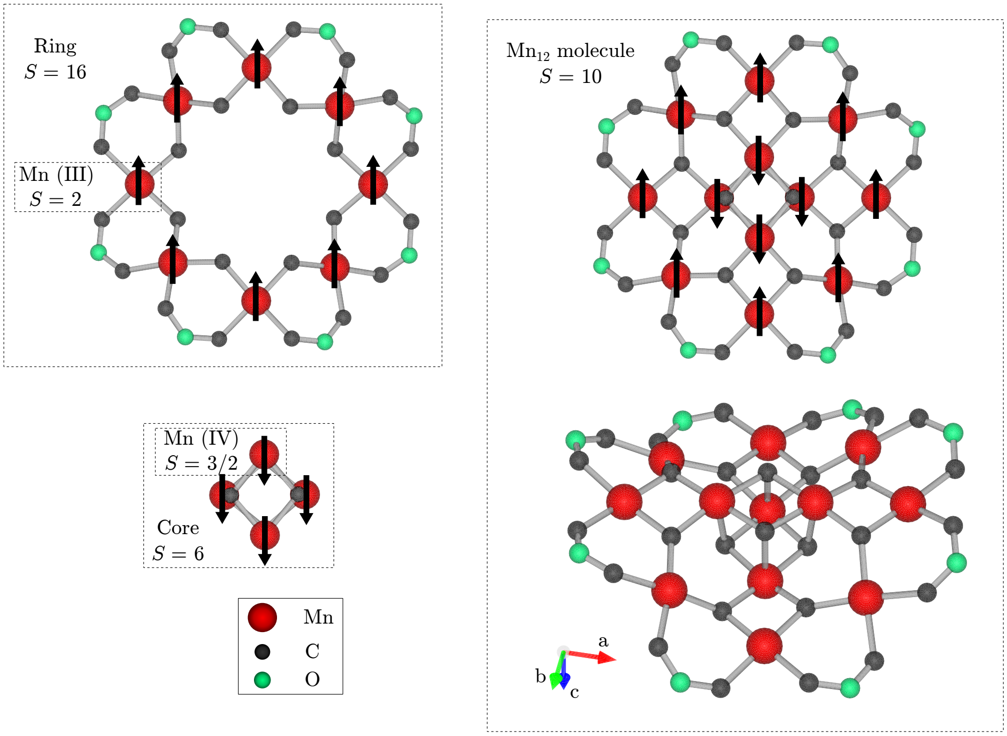

Figure 4.1: The Mn_{12} molecule, composed by Mn (red), C (black), and O (green) atoms. Some bonds and the H atoms have been omitted for clarity. The ring is composed by 8 Mn(III) atoms, with $S_{\mathrm{Mn(III)}} = 2$, ferromagnetically coupled to produce a total spin of $S_{\mathrm{ring}} = 16$. The core is composed by 4 Mn(IV) atoms, with $S_{\mathrm{Mn(IV)}} = 3/2$, ferromagnetically coupled to produce a total spin of $S_{\mathrm{core}} = 6$. The ring and core are antiferromagnetically coupled to form the molecule with a spin $S = 10$. The easy axis is along the c axis of the crystal. Figure produced with the VESTA 3 software [Momma et al. 2011].

flip for times $t \ll t_{\mathrm{f}}$—spins are *blocked*. One can hence define a *blocking temperature* that depends on the measuring time t_{m}

$$T_{\mathrm{B}} = \frac{U}{k_{\mathrm{B}} \ln \left(t_{\mathrm{m}}/t_0\right)}, \tag{4.4}$$

which separates the ferromagnetic and the superparamagnetic behavior of the particles. The superparamagnetic regime is characterized by a $1/T$ law of the susceptibility, just as a paramagnet, but with a much higher susceptibility.

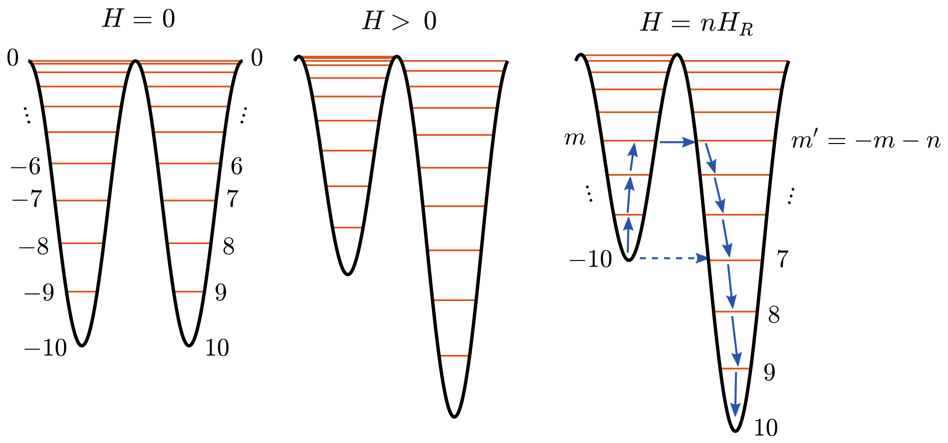

Figure 4.2: Energy barrier of the Hamiltonian from Eq. (4.2), as an external field is applied. At $H = 0$, there are two wells with $2S + 1$ levels, degenerated for the levels m and $m' = -m$. As the field is increased, the spins pointing in the field direction are more favorable. Eventually, at the resonant field values $H = nH_{\mathrm{R}}$, levels are again degenerated. A transverse component on the hamiltionian will allow tunneling between levels (dashed arrow), and thermal activation will excite the spins to the m level, which will tunnel to the $m' = -m - n$ with more probability.

4.2.4 Quantum Tunneling

Returning to Eq. (4.2), we can see that the energy levels at zero field are degenerated, with an energy barrier DS^2. A field applied along the easy axis shifts the potential well, making one spin direction more stable. However, as long as the levels are now quantized, there is a degeneracy at field values $h_z = nD$, with $n = 0, \pm 1, \pm 2, \ldots$ between the levels with spin quantum number m and $-m - n$, see Fig. 4.2. On the other hand, if there is a component of the applied field in a direction different to the anisotropy direction, the last term of the equation will allow tunneling between degenerated levels because the spin projections S_z do not commute with the Hamiltonian anymore, and thus are no longer system eigenstates. This quantization of levels produces a stepwise hysteresis curve [Friedman et al. 1996; Hernàndez et al. 1996; Thomas et al. 1996], with steps separated by $\mu_0 H_{\mathrm{R}} = \mu_0 \Delta H_z = \Delta h_z / |\gamma| \hbar$, which, in the case of Mn_{12}, takes the value $\mu_0 H_{\mathrm{R}} = 0.46$ T.

The tunneling probability between levels can be obtained taking into account the transverse part of the Hamiltonian [Chudnovsky and Tejada 1998; 2006]. It is then found that the tunnel probability increases for levels with $m \to 0$, i.e. spins have a higher tunneling probability in excited levels. If the temperature is very low, $k_{\mathrm{B}}T \ll 2DS$, almost all spins occupy the lowest energy state, and tunneling occurs at a slow and constant rate. As the temperature increases, however, the population of the excited levels increases according to the Arrhenius law, with the factor $\exp[D(m^2 - S^2)/k_{\mathrm{B}}T]$. At the same time, tunneling probability at this excited level will be higher, and hence *thermally assisted tunneling* occurs, see Fig. 4.2. The first level from the top at which the thermal activation rate dominates above the quantum tunneling is the *blocking level* m_{b}, i.e. the level at which most of the tunneling takes place. Hence, the effective barrier will be $U_{\mathrm{eff}} = E_{m_{\mathrm{b}}} - E_{-10}$. The characteristic temperature at which tunneling changes from purely quantum tunneling to thermally assisted tunneling is called *crossover temperature* T_{Q}.

The effect of the quantized barrier was suggested in relaxation experiments in clusters of Mn_{12} [Barbara et al. 1995], and later quantitatively confirmed by the steps in the magnetization curve and from the field dependance of the blocking temperature [Friedman et al. 1996]. The field dependance of the barrier can be obtained as a phenomenological approximation to the level quantization [del Barco et al. 1999; Sales et al. 1999]

$$U = DS^2\left(1 - \frac{H}{H_K}\right)^2 - c\left[1 - \left|\sin\left(\pi\frac{H}{H_{\mathrm{R}}}\right)\right|\right]^2, \tag{4.5}$$

where $c = E_{m_{\mathrm{b}}}$, and $\mu_0 H_K = 2DS/g\mu_{\mathrm{B}} = 2S\mu_0 H_{\mathrm{R}}$ the anisotropy field, i.e. the field needed to suppress the barrier. The blocking temperature, hence, will not only depend on the measuring time, but also on the external field with steps every H_{R}. Figure 4.3 shows the calculated behavior of the blocking temperature as an external field is increased, for different measuring times corresponding to the typical measurement parameters in SQUID magnetometry.

4.3 Experiments with Mn_{12} Nanospheres

4.3.1 Experimental Details

Fabrication and Characterization of Mn_{12} Nanospheres

To obtain spherical Mn_{12} particles showing the highest degree of amorphous character, they were synthesized using a method adapted from an earlier publication [Imaz et al. 2008]. In a typical experiment, 60 mg of Mn_{12} were dissolved in 15 mL of acetonitrile. The solution was added to 30 mL of toluene under vigorous stirring. Precipitation of a brown solid was observed. One hour later the resulting dispersion was centrifuged ($4' \times 8000$ rpm) and the supernatant was collected. The pellet was redispersed with acetonitrile:toluene $(1:2)$, centrifuged again and the supernatant was collected again. Both supernatants were then mixed and dried

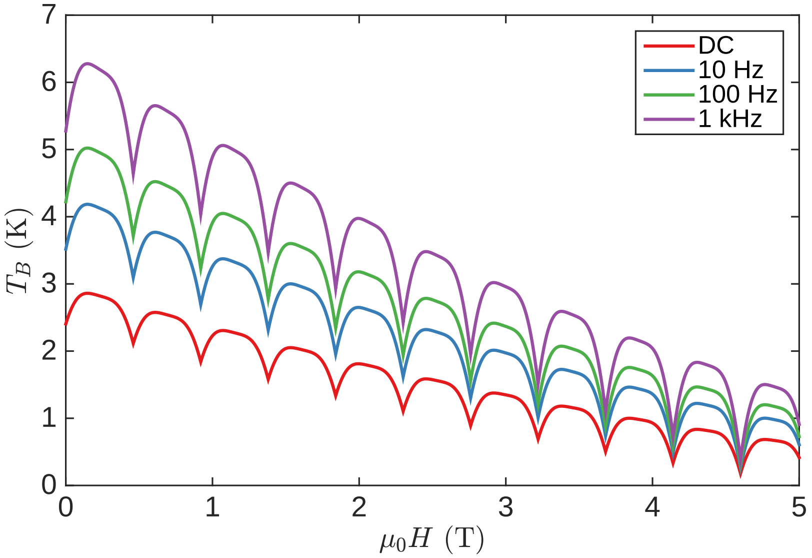

Figure 4.3: Blocking temperature dependance on the external field, according to Eqs. (4.4) and (4.5), for typical characteristic time measurements: DC (60 s) (red), 10 Hz (blue), 100 Hz (green), and 1 kHz (purple).

under vacuum condition. 5.8 mg of a brown solid (10% yield) were collected and stored in vacuum.

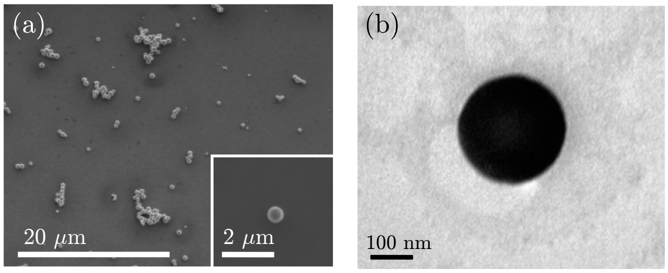

Figure 4.4: (a) Representative SEM image of Mn_{12} acetate spherical particles. Inset: individual particle. (b) TEM image of an individual Mn_{12} nanosphere.

SEM and TEM images of the brown solid revealed the formation of uniform spherical particles, see Fig. 4.4. The size of the particles was calculated from FE-SEM images by averaging the diameter of at least 300 particles from different areas of the sample. The average size of (237 ± 69) nm and the median size of 238 nm were determined. This average size was further confirmed by dynamic light scattering (DLS). The chemical correspondence with bulk $[Mn_{12}O_{12}(CH_3COO)_{16}(H_2O)_4]$

crystals was confirmed by elemental analysis and by the positive matching between the IR spectra, see Fig. 4.5. As we shall see below, the additional evidence of the conventional structure of Mn_{12} molecules in the nanospheres follows from the magnetic measurements that reveal the resonant spin tunneling at the same values of the magnetic field as for the single crystals of Mn_{12}.

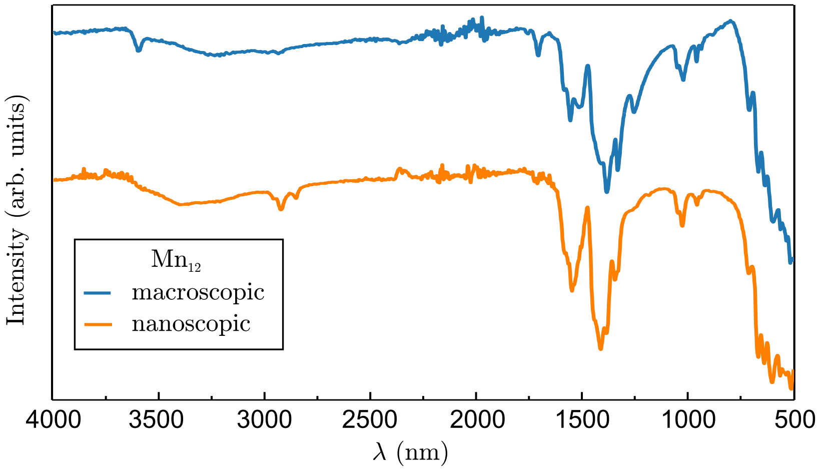

Figure 4.5: IR spectra of bulk Mn_{12} crystals (blue) and amorphous Mn_{12} nanospheres (orange).

To confirm the amorphous character of spherical Mn_{12} particles, X-ray studies have been conducted on a beam-line X17A at the National Synchrotron Light Source at Brookhaven National Laboratory. Scattering intensity was measured from high energy X-rays at an energy of 67.419 keV using the rapid acquisition pair distribution function (RAPDF) technique [Chupas et al. 2003; Juhás et al. 2013]. A large area 2-D Perkin Elmer detector with 2048 pixels × 2048 pixels and 200×200 μm^2 pixel size was mounted orthogonal to the beam path with a sample-to-detector distance of 206.1371 mm. Two samples have been measured for comparison: the sample of conventionally grown elongated micron-size crystallites of Mn_{12} and the sample of Mn_{12} nanospheres described above.

Figure 4.6 shows the structure factors and pair distribution functions for the two samples. While distinct Bragg peaks of Mn_{12} [Cornia et al. 2002; Langan et al. 2001] are present in the microcrystalline sample, a very diffused intensity has been found in the nanospheres. The same differences have been observed in the RAPDF, indicating a high level of disorder in the nanospheres. They must be either extremely defected or amorphous. As we shall see from magnetic measurements, however, the Mn_{12} molecules are well preserved in the nanospheres despite of the structural disorder.

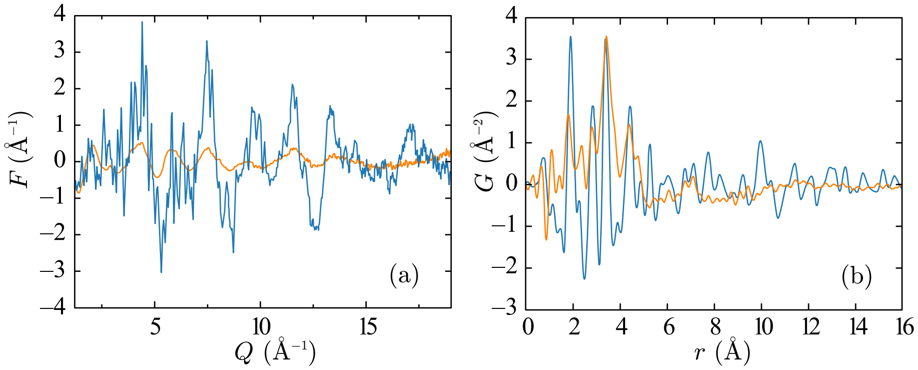

Figure 4.6: (a) Structure factors for microscrystals (blue) and nanospheres (orange) of Mn_{12}. (b) Superimposed pair distribution functions for microscrystals (blue) and nanospheres (orange) of Mn_{12}.

Magnetic Measurements

We prepared a compressed powdered sample and measured it at low temperature inside a commercial rf-SQUID Quantum Design magnetometer. Temperature can be varied in the range 1.8 K – 350 K, and field from −5 T to 5 T. Before doing the measurements reported here, we attempted to orient the nanoparticles in an epoxy with a high magnetic field (5 T) at room temperature, as had been done previously with μm-size crystals. In our experiments, measurements with and without the orienting procedure were equivalent, opposite to previous experiments with microcrystals. We can understand this behavior from the fact that micron-size crystallites of Mn_{12} grow elongated along the easy magnetization axis. The resulting anisotropy of the magnetic susceptibility then enables the alignment of the crystallites by a high magnetic field in a nonconductive epoxy resin, even though the molecules do not have magnetic moments at room temperature. This method, however, does not work for the Mn_{12} nanoparticles of spherical shape.

4.3.2 Results

We plot descending negative branches of hysteresis curves in Fig. 4.7. We ZFC the sample to the measuring temperature. Once the temperature was stable, we applied a field of 5 T. Then, we swept the field down to −5 T at a constant rate. At the same time, we recorded the magnetization. At the lowest temperature of 1.8 K, when thermal effects are weak, $M(0)$ is about one half of the saturation value M_S. This corresponds to the magnetic moments of Mn_{12} molecules looking randomly into a hemisphere, which follows from

$$\frac{M(0)}{M_S} = \frac{1}{4\pi}\int_0^{2\pi} d\phi \int_0^{\pi/2} \sin\theta d\theta = \frac{1}{2}. \tag{4.6}$$

This is true regardless of whether the disorder in the orientation of easy magnetization axes occurs at the level of individual Mn_{12} molecules inside amorphous nanospheres or at the level of the nanospheres, each having a coherent orientation of the easy axes of the molecules.

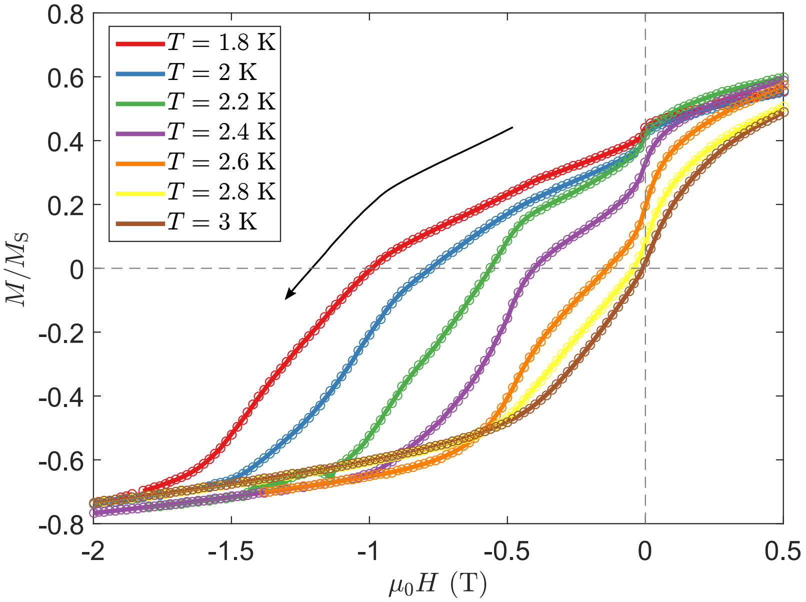

Figure 4.7: $\mu_0 H < 0$ branch of the hysteresis curves of the disordered powder of Mn_{12} nanospheres at different temperatures.

We measured field-cooled (FC) and ZFC magnetic moment ($\mu = MV$) curves, see Fig. 4.8. The ZFC curve was obtained after cooling the sample from 300 K to 1.8 K, at which point we applied a small measuring field of 10 mT. We then measured the magnetic moment as the temperature increased at a constant rate. The FC curve was recorded after the ZFC, as the temperature decreases from 16 K, above the blocking temperature. The high-temperature behavior is a $1/T$ Curie law, according to the superparamagnetic regime. From this curve, we obtain a blocking temperature $T_B \approx 3$ K.

Figure 4.9 shows the magnetic response of the Mn_{12} nanospheres to an ac field of 0.3 mT. The maximum in the imaginary part—also equal to the maximum of the real part derivative—corresponds to the blocking temperature T_B [Zélis et

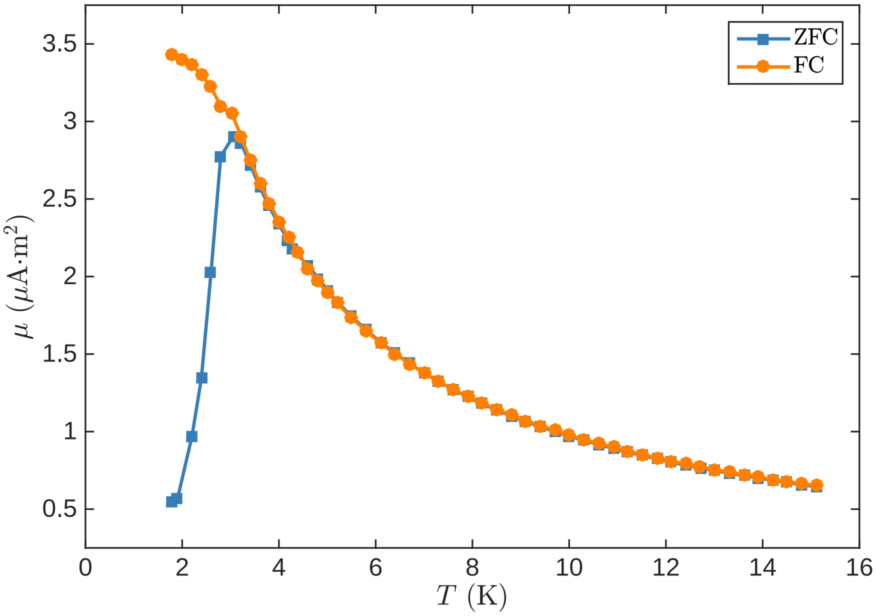

Figure 4.8: FC (orange) and ZFC (blue) magnetic moment vs temperature curves for a disordered powder of Mn_{12} nanospheres in the dc field of 10 mT.

al. 2015], determined by the magnetic moments that reverse their orientation on the time scale of the measurement, following Eq. (4.3). In the ac measurements $t_\mathrm{m} \sim 1/f$, so that T_B scales with the frequency of the ac field as $U(H)/\ln(1/t_0 f)$, as in Eq. (4.4). Our data shows this scaling behavior, as we can see from the inset in Fig. 4.9(b). In this inset we show the data fit to Eq (4.4), from which we get the estimated values $t_0 = (5 \pm 1) \cdot 10^{-8}$ s for the attempt time and $U(0) = (69 \pm 2)$ K for the energy barrier at zero field.

One-maximum structure of the curves in Figs. 4.8 and 4.9 contrasts with a pronounced two-maxima structure observed in Refs. [Carbonera et al. 2008; Imaz et al. 2008], with the second, lower maximum occurring at a lower temperature. According to the authors of Refs. [Carbonera et al. 2008; Imaz et al. 2008], where spherical nanoparticles of average size under 50 nm were studied, the low-temperature maximum corresponded to the presence of 40% fast-relaxing species of Mn_{12}. We argue that such a species would have a very low abundance in our highly amorphous, larger spherical particles. This simplifies the analysis of our data.

We plot the derivative of the magnetic moment with respect to the magnetic field $\mathrm{d}\mu/\mathrm{d}(\mu_0 H)$ in Fig. 4.10, for the negative branch of the hysteresis curve in Fig. 4.7. For all the measured temperatures we observe a maximum at zero field

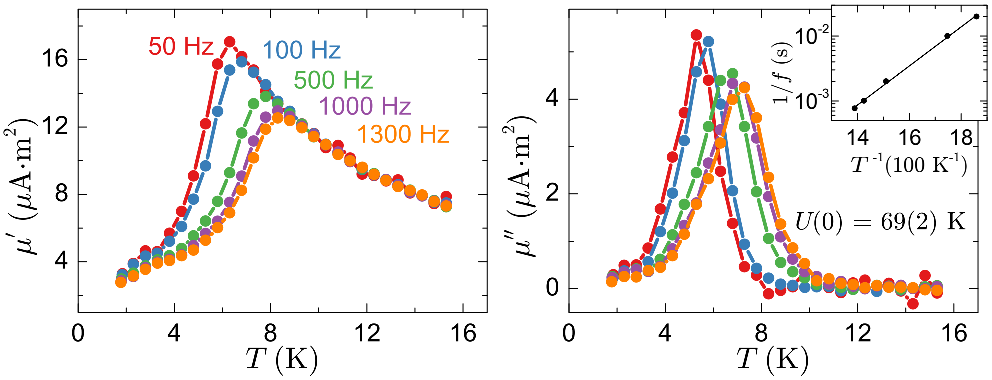

Figure 4.9: Real part (left-hand-side panel) and imaginary part (right-hand-side panel) of the ac magnetic moment in the frequency range 50 Hz – 1.3 kHz in the presence of a 0.3 mT ac field. The inset shows logarithmic dependence of the blocking temperature on $1/f$. The fitted value of the energy barrier in a zero field is $U(0) = (69 \pm 2)$ K.

with a width of ∼ 100 mT. This peak is narrower than the zero-field peak maximum observed in Refs. [Carbonera et al. 2008; Imaz et al. 2008] for a similar sample. Besides this maximum, there are two other maxima at the characteristic resonant field values ($\mu_0 H_n = -n\mu_0 H_{\rm R}$) of Mn_{12} in a negative field parallel to the easy axis $\mu_0 H_1 = -0.46$ T and $\mu_0 H_2 = -0.92$ T for a temperature $T = 2.4$ K, and at the first resonance for $T = 2.6$ K, despite the random orientation of the easy magnetization axes of the molecules. The analysis we shall see below reveals that this is indeed the expected behavior in randomly oriented magnetic molecules.

Thermally assisted spin tunneling illustrated in Fig. 4.11 takes place as the field becomes negative $\mu_0 H < 0$. If the easy axis of a particular molecule makes an angle θ with the negative direction of the field, then the condition of the n-th resonance is

$$H = -\frac{H_n}{\cos\theta}, \qquad 0 \le \theta \le \frac{\pi}{2}. \tag{4.7}$$

Thus, at any value of the field H the molecules that are on the n-th resonance satisfy

$$\cos\theta = -\frac{H_n}{H}. \tag{4.8}$$

Note that the zero-field maximum in the derivative of the magnetization, observed in all the temperatures, is due to molecules close to the $n = 0$ resonance. The width indicates the detuning effect due to local dipolar and hyperfine fields, of magnitude ∼ 100 mT or below. In the following we focus on the subsequent resonances $n = 1, 2, ...$, not previously reported for disordered powders.

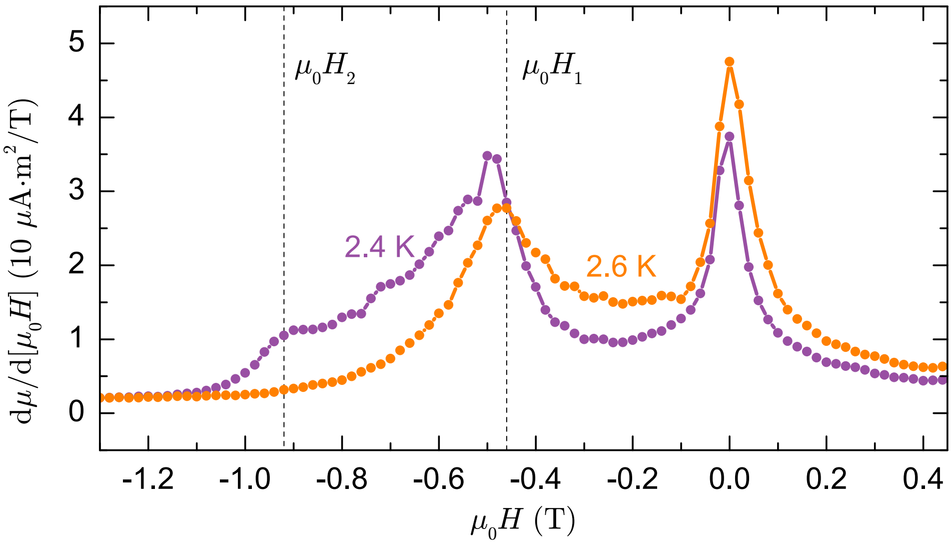

Figure 4.10: Derivative $d\mu/d(\mu_0H)$ for the $\mu_0H < 0$ branch of the hysteresis curve of the disordered powder of Mn_{12} nanospheres: $T = 2.4$ K (purple), and $T = 2.6$ K (orange).

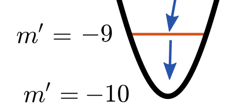

Figure 4.11: Thermally assisted tunneling between resonant spin levels in a Mn_{12} molecule, for $H < 0$.

Since the element of the spherical volume is proportional to $\sin\theta\,\mathrm{d}\theta = -\mathrm{d}\cos\theta$, the total number of molecules that enter the resonance condition when the field increases in the negative direction by a small increment $\mathrm{d}H < 0$ is

$$\mathrm{d}N_{\mathrm{res}} \propto -\mathrm{d}\cos\theta \propto -\frac{\mathrm{d}H}{H^2}\sum_{H_n\leq|H|} H_n > 0. \tag{4.9}$$

At low temperature, when the field sweep is sufficiently slow, the change in the magnetization, $\mathrm{d}M$, should be proportional to $-\mathrm{d}N_{\mathrm{res}}$,

$$\mathrm{d}\mu \propto -\mathrm{d}N_{\mathrm{res}} \propto \frac{\mathrm{d}H}{H^2}\sum_{H_n\leq|H|} H_n < 0. \tag{4.10}$$

This gives

$$\frac{\mathrm{d}\mu}{\mathrm{d}H} \propto \frac{1}{H^2}\sum_{H_n\leq|H|} H_n > 0 \tag{4.11}$$

The function in the right-hand-side of this equation has a jump-wise behavior. At $H_1 \leq |H| < H_2 = 2H_1$ it behaves as H_1/H^2. At $H_2 \leq |H| < H_3 = 3H_1$ it behaves as $3H_1/H^2$. At $H_3 \leq |H| < H_4 = 4H_1$ it behaves as $6H_1/H^2$, and so on. Its value at $H = H_n$ equals

$$\frac{1}{H_n^2}\sum_{H_n\leq|H|} H_n = \frac{1}{n^2 H_1}\sum_{k=1}^{n} k = \frac{1}{2H_1}\left(1+\frac{1}{n}\right). \tag{4.12}$$

This analysis leads to the following conclusion. Spin tunneling resonances in a system of randomly oriented magnetic molecules can be seen as maxima in $\mathrm{d}\mu/\mathrm{d}H$. However, only the $H = 0$ maximum is a narrow tunneling resonance for all molecules within dipolar/hyperfine window. Each subsequent n-th "resonance" begins at $H = -H_n$ and extends to all $H < -H_n < 0$ due to different resonance conditions for differently oriented molecules. If one neglects broadening due to dipolar and hyperfine fields, these "resonances" begin with a vertical jump in $\mathrm{d}\mu/\mathrm{d}H$ at $H = -H_n$, followed by the $1/H^2$ decrease of $\mathrm{d}\mu/\mathrm{d}H$. Dipolar and hyperfine fields must smear the initial vertical rise of the "resonance" by up to 100 mT. However, the $1/H^2$ post-resonance ($H < -H_n$) decrease of $\mathrm{d}\mu/\mathrm{d}H$ over the 460 mT range from $H = -H_n$ to $H = -H_{n+1}$ must be apparent. This is seen in Fig. 4.12, that shows the fit of the post-resonance $\mathrm{d}\mu/\mathrm{d}H$ by $1/H^2$ after crossing the first resonance. In the kelvin-temperature range the effect becomes less pronounced at higher n due to the exponential increased thermal relaxation as the field lowers the barrier.

Note that, for the same reason as discussed above, the evidence of spin tunneling in a disordered system can also be obtained by plotting the dependence of

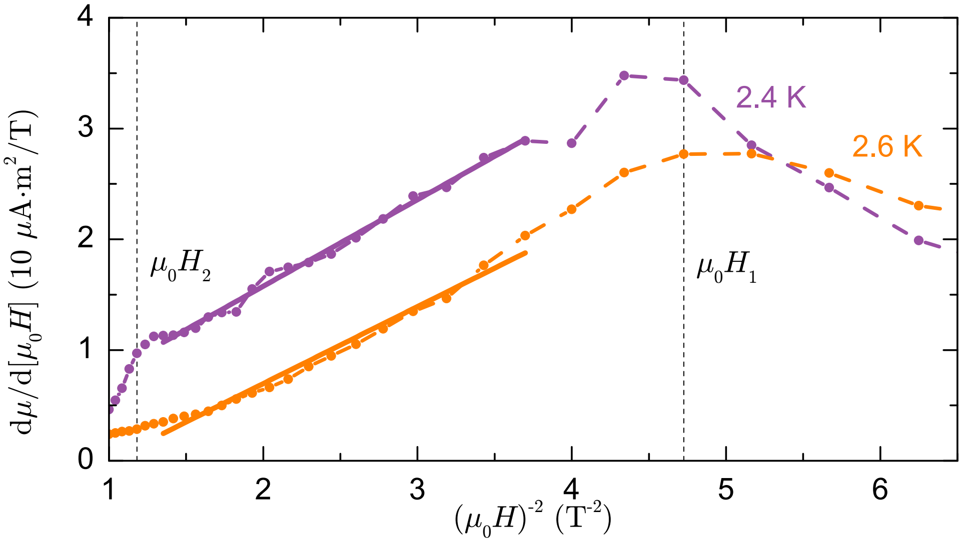

Figure 4.12: The $1/H^2$ fit (thick line) of $dm/d(\mu_0 H)$ between first and second spin tunneling resonances for a disordered powder of Mn$_{12}$ nanospheres: T = 2.4 K (purple), and T = 2.6 K (orange).

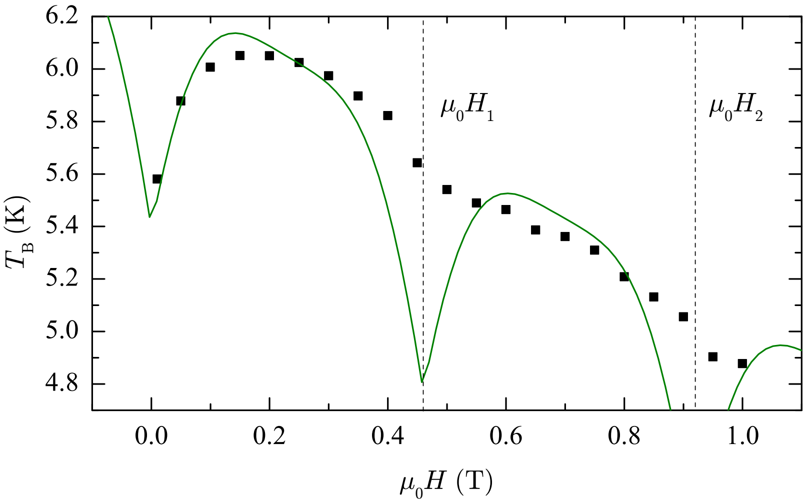

Figure 4.13: Dependence of the blocking temperature on the dc field in the ac field of 100 Hz.

the blocking temperature on the dc magnetic field, see Fig. 4.13. T_B is proportional to the energy barrier for the spin reversal $U(H)$, as expressed in Eq. (4.4). At $\mu_0 H = 0$ T the barrier is lowered due to thermally assisted quantum tunneling between resonant spin levels near the top of the barrier, see Fig. 4.11. The number of molecules on the zero-field resonance at a particular value of the field progressively drops as the field approaches the boundary of the dipolar/hyperfine window, which for Mn_{12} has a width on the order of 100 mT. At that boundary, T_B is approximately determined by the full 69 K classical energy barrier for the superparamagnetic spin flip. As the field continues to increase, the field dependence of the blocking temperature is dominated by the classical reduction of the energy barrier due to the growing Zeeman energy, which leads to the decrease of T_B on H. When the field reaches $\mu_0 H_1 \approx 460$ mT, randomly oriented Mn_{12} molecules begin to enter the first resonance. We can see the evidence of that in Fig. 4.13 in the change of the derivative of T_B on $\mu_0 H$ at $\mu_0 H = \mu_0 H_1$. The figure also shows the dependence of T_B adjusted with the phenomenological expression of Eq. (4.5). From this expression, we obtain that the dominating level of tunneling at zero field is $m_\mathrm{b} = -4$. At higher fields, the validity of the expression reduces, as it does not take into account possible dependence of the adjustable parameter c with field. One should keep in mind that the expression was obtained phenomenologically [Sales et al. 1999], and hence its applicability is limited.

4.3.3 Discussion

Amorphous or highly disordered structure of Mn_{12} nanospheres raises the question whether the easy axes of Mn_{12} molecules inside the spheres are aligned or disordered. One should notice in this connection that the direction of the easy axis is related to the orientation of the molecules while the Bragg peaks in the X-ray scattering are related to the translational order in a crystal. In an amorphous solid the orientation of local crystallographic axes is more robust than the translational order [Nelson 1984]. It may spread well beyond the amorphous structure factor. Evidence of the extended correlations in the orientation of local magnetic anisotropy axes has been previously reported in amorphous magnets [Chudnovsky and Tejada 1993]. For our conclusions, it does not matter whether the easy axes of the molecules are disordered at the level of individual nanospheres, due to the random orientation of nanospheres, or both.

Measurements of the FC and ZFC magnetization curves, and of the ac response of the magnetic moment, revealed the presence of only one magnetic species of Mn_{12}, which is in contrast with previous measurements on nanospheres containing comparable amounts of slow and fast relaxing species [Carbonera et al. 2008; Imaz et al. 2008]. The striking feature of the magnetization curve is the presence of well-defined sharp tunneling maxima in $\mathrm{d}M/\mathrm{d}H$ in a sample with random orientation of easy magnetization axes of the molecules. The maxima occur at the conventional resonant fields, $\mu_0 H_n = -n\mu_0 H_1$, with $\mu_0 H_1 \approx 460$ mT, for negative applied fields.

We give quantitative explanation to this observation. At any value of the field $\mu_0 H$ the molecules that are on the n-th resonance have their easy axis at an angle θ with the field, satisfying $\cos\theta = -H_n/H$. Thus, as soon as the field enters the range $\mu_0 H \leq -\mu_0 H_n$ a new set of molecules that satisfy the n-th resonance condition begins to reverse the magnetization. This results in the change of the slope of $M(H)$ every time the field reaches the value $\mu_0 H_n = -n\mu_0 H_1$, and in the corresponding peaks in $\mathrm{d}M/\mathrm{d}H$. However, only the $n = 0$ peak is the same tunneling resonance as in a crystalline sample, when all molecules achieve the resonance condition inside the dipolar/hyperfine field window. As our analysis show, all subsequent resonances are characterized by a steep jump of $\mathrm{d}M/\mathrm{d}H$ at $\mu_0 H_n = -n\mu_0 H_1$ followed by a $1/H^2$ decrease, which agrees with the experimental data.

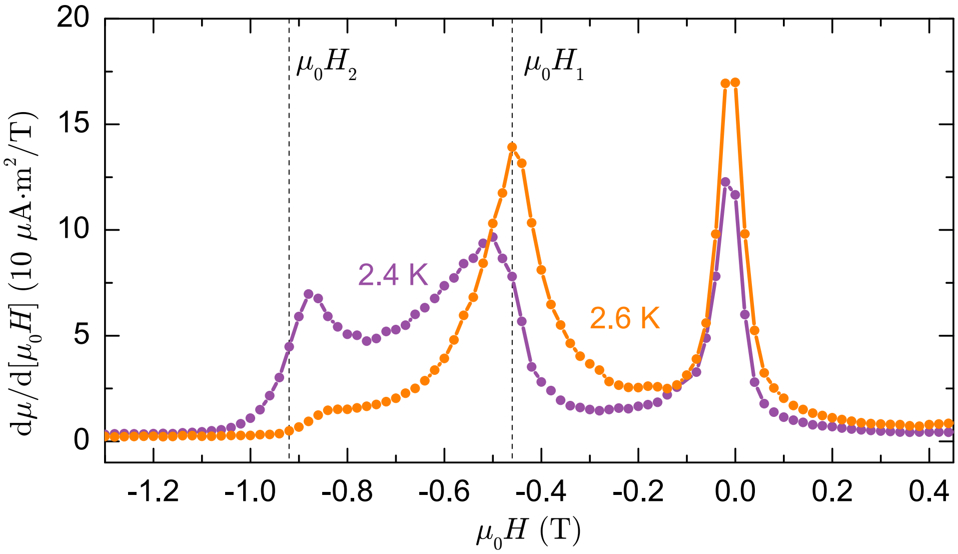

Figure 4.14: Magnetic moment derivative with respect to field in a sample of randomly oriented micron-size crystallites of Mn_{12}.

These results suggest that, to observe resonant spin tunneling, it is not necessary to align the microcrystals with an external intense field to obtain parallel easy axes. This procedure was used in the studies in [Friedman et al. 1996] that reported the discovery of the resonant spin tunneling in Mn_{12}, and it has been the standard process to study microcrystals of single-molecule magnets since then. In order to be able to fully validate the applicability of the results from randomly oriented nanospheres, we measured a sample of non-oriented powder consisting of microcrystalline Mn_{12}, nominally identical to the powder used in the aforementioned publication. The magnetization derivative is showed in Fig. 4.14, where we observe two tunneling maxima, besides the maximum at zero-field. This agrees with the Mn_{12} nanospheres reported above, see Fig. 4.10.

4.4 Conclusions

In this chapter we have studied the single-molecule magnet Mn_{12}, a system that has contributed to the understanding of magnetism at the nanoscale level, and how quantum phenomena can be observed at the macroscopic level. We have seen that this molecule is mainly described by the anisotropy term, as the exchange interaction can be neglected. Given the small spin of the macroscopic signal, the level quantization gives rise to steps in the magnetization, that we have observed in our measurements of Mn_{12} nanospheres and microcrystalline powder.

The nanosphere samples have been characterized by chemical, infrared, TEM, X-ray, and magnetic methods. While the structure of Mn_{12} molecules appears to be the same as in a crystalline sample, their easy magnetization axes are completely disordered. Random orientation of the easy axes has been confirmed by magnetic measurements. It occurs either at the level of individual molecules inside the nanospheres, or at the level of randomly oriented nanospheres, or both. Isotropic magnetic susceptibility of the nanospheres at room temperature, when Mn_{12} molecules do not possess magnetic moments, excludes any possibility of aligning their easy axes in a high magnetic field as was done for the sample of Mn_{12} consisting of elongated microcrystals [Friedman et al. 1996].

We have observed quantum tunneling in the magnetic measurements of randomly oriented samples, and given a model that describes the observed peaks. We have further verified this behavior with a microcrystalline sample, as the one used in the discovery of macroscopic quantum tunneling. These results are useful in the field of single-molecule magnets because it simplifies the effort of finding spin tunneling. The evidence of spin tunneling should appear as maxima in the magnetization derivative with respect to the external field, even in non-oriented samples. Also, from this study it follows that maxima in the derivative are not a unique consequence of an ordered material.

We, therefore, conclude that while single crystals are good for the in depth study of spin tunneling, the robust evidence of the effect can be obtained from the magnetization curve of any microcrystalline sample as long as the magnetic molecules preserve their structure. This should greatly simplify the effort by chemists and physicists to track spin tunneling effects in newly synthesized single-molecule magnets.

5

Magnetic Vortices in Elongated Patterns

Magnetic systems at zero field tend to split in domains to minimize their total magnetic energy, giving rise to a variety of possible configurations. Magnetic domains, despite the complex configuration of the magnetization, can be treated as a sole object, but their behavior will differ from that of a single spin. One of the configurations that has driven more attention in the past years is the magnetic vortex formed in thin, circular ferromagnetic materials. The vortex is characterized by a chiral configuration of the magnetization following the edges of the quasi-planar sample, with a central core of ≈ 10 nm in which the magnetization points out of plane. The process of core reversal, however, is still not well understood. It involves the generation of a vortex-antivortex pair. Finding new ways to excite magnetic vortices and finding new states in which the antivortex is stabilized may lead to a better understanding of the antivortex dynamics and the process of core reversal. Moreover, the dynamic control of the antivortex may lead to a different working regime than the single vortex and allow frequency selectivity in broader spectra. In this chapter we control the creation of antivortex states by exciting samples consisting of a single vortex. We generate the antivortex sending a high-power microwave pulse at the characteristic oscillating frequency of the vortex. We also study the complex frequency spectra of thick stadium-shape samples, which we associate to a thickness-dependent core. This non-rigid core may have different excitation modes.

5.1 Introduction

For the past decades, technological advances have allowed the study of the magnetization at a very high spatial resolution thanks to force microscopes and patterning of micron-sized structures by optical lithography and sub-micron-sized by electron beam lithography. The reduction of the lateral sizes in a thin film leads to domain formation. The magnetic configuration is affected by the shape of the structure. In thin disks, a possible ground state consists of a magnetic vortex. Some uses for these magnetic vortices have been suggested: bits for magnetic memories due to the high stability of the vortex core and high velocity of core reversion [Bohlens et al. 2008; Bussmann et al. 1999; Drews et al. 2009; Kasai et al. 2008; Uhlíř et al. 2013]; high-frequency oscillators of several GHz [Cowburn 2002]; cancer-cell destruction exploding the low dipolar interaction between disks and the mechanical movement of the vortex under an external modulated field [Kim et al. 2010; Rozhkova et al. 2009]; and magnonic devices to filter certain frequencies, given the possibility to modulate the frequency by fabricating arrays of interacting dots [Huber et al. 2011]. Magnetic vortices are also interesting from a fundamental point of view, as they show quantum phenomena at low temperatures [Zarzuela, Chudnovsky, Hernandez, et al. 2013; Zarzuela, Vélez, et al. 2012].

Micron- and sub-micron-sized ferromagnetic ellipses generate a ground state consisting of a single vortex, similar to disks, or two vortices with opposite chirality [Buchanan et al. 2005]. The direction of the saturation field changes the way the spins are configured to close the flux. A field on the long axis first produces an S-shape and a two-vortices ground state. A field on the short axis produces a C-shape and a single-vortex ground state.

The frequency behavior of the two vortices depends on their relative orientation —parallel $p_1 p_2 = 1$, or antiparallel $p_1 p_2 = -1$ [Buchanan et al. 2006]. The elliptical shape produces an asymmetric distribution of the barriers in the two axis. As a consequence, the frequency increases when the core moves in the long axis, and it is constant along the short axis, as in the disk-shape case. Depending on the phase of motion of the two vortices, the frequency splits. If the two vortices gyrate in phase, there is no splitting because the energy barriers on each vortex are not altered. However, if the two vortex gyrate out of phase, as the cores come together or separate the interacting spins change the energy barriers and a splitting appears. The phase of rotation is determined by the direction of the excitation field relative to the axis of the ellipse.

Jain, Novosad, et al. [2012] studied a system consisting of two coupled vortices. Exciting the system at a certain frequency favors a particular ground state. When the excitation is sent, the system undergoes continuous reversal of the cores at the resonant frequency. Because the characteristic frequencies of the $p_1 p_2 = 1$ and the $p_1 p_2 = -1$ are different, the system stops reversal once the non-resonant state is reached.

The antivortices, often found in cross-tie Bloch walls [Hubert et al. 1998], are the topological counterpart of vortices. There are a few reports where anti-vortices are created in patterned structures, for example, via an alteration of the sample geometry [Drews et al. 2009; Krüger et al. 2008; Mironov et al. 2010; Pues et al.

2012]. Novel ways to create and control the anti-vortices in model systems are highly desirable.

We have designed a new way to generate anti-vortices with a simple geometry. We have used ferromagnetic elongated shapes patterned on top of CPW to measure the characteristic spectral response and to excite the system, as in [Jain, Novosad, et al. 2012]. Hence, we prove the high applicability of this method to interacting vortices. We have used nanofabrication techniques, such as optical lithography, electron-beam lithography and evaporation, and sputtering. The dynamics of the ferromagnetic ellipses have been measured with a network analyzer connected to the CPW. This is sensitive to the thousands of patterns deposited on top of the CPW, which increases the signal and hence makes the measurement possible without any amplification of the signal. The static magnetic configuration is determined with MFM images, and compared to the simulated images.

5.2 Background

5.2.1 Formation of the Magnetic Vortex

The interplay between all the energies in a certain magnetic system determines the ground state of the magnetization. For the case of soft ferromagnets having small anisotropy fields H_K, such as iron (Fe), cobalt (Co), nickel (Ni) and some of their alloys, the main contributions are the exchange and magnetostatic energies. In this kind of samples, magnetic domains form, Fig. 5.1. As the thickness of the system is reduced, spins are limited to the film plane, as it is energetically favorable, and the domains form characteristic stripes on the film, with micron-size widths, Fig. 5.1. If the lateral dimensions are also shrunk, magnetization tends to align along the edges of the shape to minimize magnetostatic energy, but exchange interaction between opposed spins generates non-trivial magnetic configurations. The exchange length,

$$l_{\text{ex}} \sim \sqrt{\frac{2A}{\mu_0 M_{\text{S}}^2}}, \tag{5.1}$$

is a fundamental unit that measures the distance above which magnetostatic energy dominates above exchange. For Py that has a close-to-zero magnetocrystalline anisotropy, this value is ~ 5 nm. Depending on the relative sizes in each dimension, the magnetic configuration is different, and it is determined by minimization of the total energy.

In a cylinder, a magnetic vortex can be formed. The studies in [d'Albuquerque e Castro et al. 2002; S.-H. Chung et al. 2010; Cowburn et al. 1999] show how the ratio between the diameter, $2R$, and the thickness, L, of the disk determines

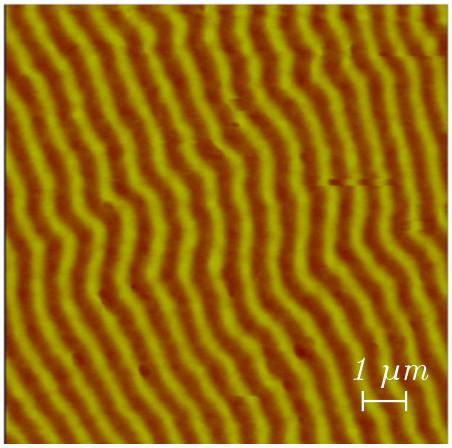

Figure 5.1: Image of magnetic domains on a Py film of 350 nm thickness. Reprinted with permission from McCord, J. et al., "Revisiting magnetic stripe domains — anisotropy gradient and stripe asymmetry," J. Appl. Phys. **113**, 073903 [2013]. Copyright 2013, AIP Publishing LLC.

the ground state, changing from single domain (SD) in the axis direction for long cylinders to a SD in the plane for thin disks. In between these two states there is one in which the magnetization curls around the center, following the circular shape of the edges; this is the *vortex state*. Figure 5.2 shows the formation of the vortex state depending on the size of the cylinder.

In the inner center, ~ 10 nm, of the curling spins the magnetization points out of plain because of the strong exchange interaction of the antiparallel neighbors. Magnetic force microscopes allowed the observation of the out-of-plane component of the magnetization in Py disks [Shinjo et al. 2000], and in-plane magnetization is also observable with other techniques, such as Lorentz microscopy [Schneider et al. 2000]. Hence, the vortex ground state is fully characterized by the clockwise (CW) or counterclockwise (CCW) orientation of the magnetization in the plane—the chirality, C—, and by the direction of the out-of-plane core, up or down—the polarity, p. In the axes coordinates where the core is in the center, the in-plane magnetization is characterized by:

$$\phi(\beta) = n\beta + C\frac{\pi}{2}, \tag{5.2}$$

where ϕ is the angle between the local magnetization and the X axis, β the angle between the position vector from the origin to the local magnetization and the X axis, and n is the winding number. For a vortex, the winding number $n = 1$, and the chirality $C = \pm 1$, see Fig. 5.3.

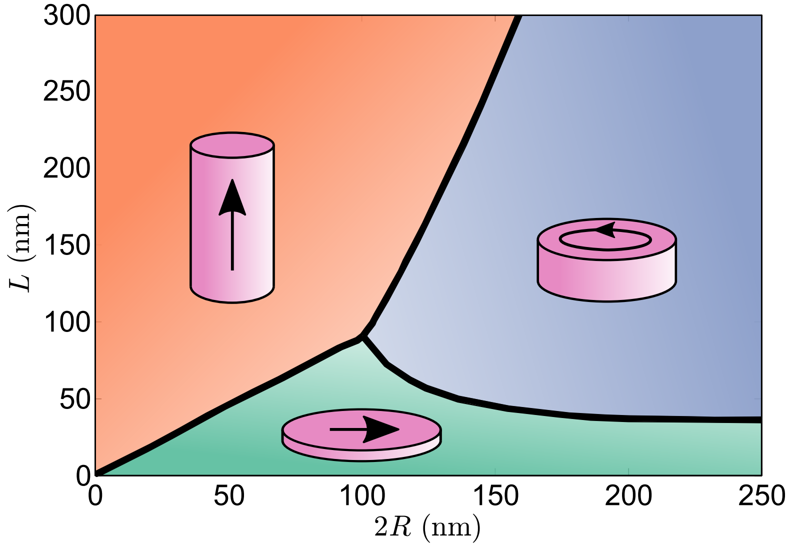

Figure 5.2: State diagram showing the magnetization configuration depending on the thickness L and diameter $2R$ of a cylinder, according to d'Albuquerque e Castro et al. [2002].

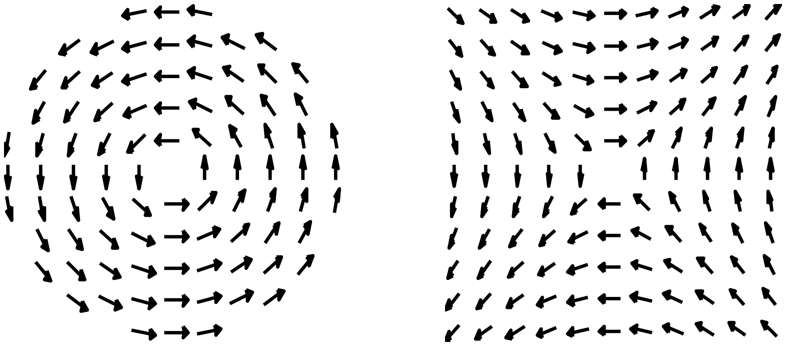

Figure 5.3: (Left-hand-side panel) Vortex state in a disk obtained with Eq. (5.2) with values $n = 1$ and $C = 1$. (Right-hand-side panel) Antivortex with values $n = -1$ and $C = 1$.

Because the spins curl around the center in the ground state, the average in-plane magnetization is zero. When an external in-plane magnetic field $\vec{H}_0$ is applied, the Zeeman term enters in the energy balance, and the disk domain with magnetization parallel to the field grows. This results in an effective in-plane displacement of the core perpendicular to the field. When the field is further increased up to the annihilation field H_{an}, all spins are eventually expelled from the disk, producing a step increase in the average magnetization, and the disk is in a SD state. When the field is reduced from the SD state, domains begin to form to reduce stray fields, but the initial shape of the magnetization can be many-fold. In C-shape configuration, a core is formed at one of the transverse edges of the disk, with spins beginning to curl around the core. In S-shape configuration, the spins deviate from the field direction forming two opposite vortex regions that collapse at lower fields, see Fig. 5.4. At the nucleation field $H_{\mathrm{n}} < H_{\mathrm{an}}$, the vortex is formed. A measured magnetization curve is showed in Fig. 5.5.

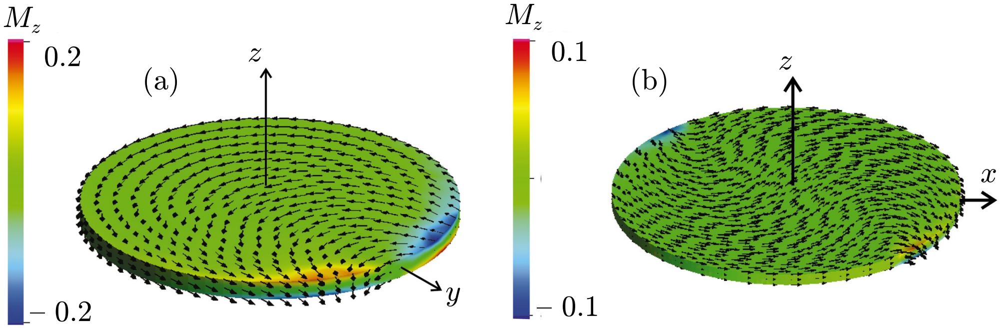

Figure 5.4: Simulation of a Py disk with the magnetization in (a) C-shape configuration, and (b) S-shape configuration. Reprinted figure with permission from Ha, J. K. et al., "Configurational stability and magnetization processes in submicron permalloy disks," Phys. Rev. B **67**, 064418 [2003] and Ha, J. K. et al., "Micromagnetic study of magnetic configurations in submicron permalloy disks," Phys. Rev. B **67**, 224432 [2003]. Copyright 2003 by the American Physical Society.

Note that if the winding number of expression (5.2) takes the value $n = -1$, an antivortex is produced, see the right-hand-side panel of Fig. 5.3. This state can be achieved by patterning and infinite shape in a permalloy sample, and with similar patterns [Mironov et al. 2010].

5.2.2 Motion of the Vortex Core

If the field is removed when the core is out of the center, the core evolves to its equilibrium position with a characteristic frequency: the *gyrotropic frequency* ω_0. The gyrotropic frequency is much lower than the characteristic resonance of the individual spins and than the propagation of spin-waves in the material.

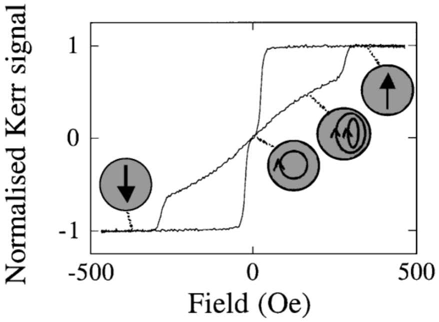

Figure 5.5: Hysteresis loop of a magnetic vortex measured using Kerr effect. Reprinted figure with permission from Cowburn, R. P. et al., "Single-Domain Circular Nanomagnets," Phys. Rev. Lett. **83**, 1042–1045 [1999]. Copyright 1999 by the American Physical Society.

Similarly, the core precession at ω_0 may be produced with an external excitation. This frequency is characteristic of the shape and materials. Guslienko, Ivanov, et al. [2002] proposed a model to determine the frequency as a function of the aspect ratio $\beta = R/L$. Choe et al. [2004] observed, with X-ray images, the different rotation direction of the core depending on the chirality. Novosad, Fradin, et al. [2005] used an array of patterned disks on top of a CPW to detect the motion.

The symmetrical shape of the disk causes the frequency to be mainly field independent. A deviation from this behavior occurs at fields in which the core is close to the disk border; in this case, the frequency increases because the core is confined to oscillate at a lower amplitude, and is finally suppressed.

Time evolution of a magnetization vector $\vec{M}$ of magnitude M_S under the influence of an effective field $\vec{H}_\mathrm{eff}$ is governed by the Landau-Lifshitz equation (2.30), described in Chapter 2. In the case of Py, the crystalline anisotropy is negligible and it does not enter in the effective field $\vec{H}_\mathrm{eff}$.

For a vortex, assuming the absolute values of the magnetization vectors remain constant $\vec{M}/M_\mathrm{S} = 1$, and integrating over the volume, the Thiele equation describing movement of the core position $\vec{X}$ is obtained [Guslienko, Ivanov, et al. 2002; Thiele 1973]:

$$\frac{\mathrm{d}\vec{X}}{\mathrm{d}t} \times \vec{G} + \frac{\partial W(\vec{X})}{\partial \vec{X}} - \hat{D}\frac{\mathrm{d}\vec{X}}{\mathrm{d}t} = 0, \tag{5.3}$$

where $\vec{G}$ is the gyroscopic vector, $\hat{D}$ the dissipation tensor, and $W(\vec{X})$ the energy of the vortex that takes into account exchange, magnetostatic and Zeeman energies. The first term, the gyroscopic force, acts perpendicular to the velocity of the core, similar to the Lorentz force acting on an electron moving through a magnetic field.

The second term is a restoring force due to the potential $W(\vec{X})$. The third term is a dissipative force. With this approach, the movement of the vortex magnetization pattern is simplified to the vortex core in a potential with an external force, and a characteristic frequency can be obtained [Guslienko, Ivanov, et al. 2002]:

$$\omega_0 = \frac{1}{2}\gamma\mu_0 M_{\mathrm{S}} \frac{\xi^2}{\chi(0)}, \tag{5.4}$$

where γ is the gyromagnetic ratio. The values of ξ and the initial susceptibility $\chi(0)$ depend on the model used to obtain the equation, i.e. the rigid vortex model (RVM) or the two vortex model (2VM). The RVM assumes that the entire vortex moves rigidly, but it has magnetic side surface charges. The 2VM avoids this issue, and fits better the experimental results. In this case, $\xi = 2/3$ and the susceptibility is

$$\chi(0)^{-1} = 9(4\pi \mathrm{F}_v(\beta) - (l_{\mathrm{ex}}/R)^2/2), \tag{5.5}$$

$$f(x) = 1 - \frac{1-e^{-x}}{x}, \quad \mathrm{F}_v(x) = \int_0^\infty \mathrm{d}t \frac{f(xt)}{t}\left(\int_0^1 \mathrm{d}\rho\rho \mathrm{J}_1(\rho t)\right)^2 \tag{5.6}$$

where J_1 is the Bessel function of first kind and order 1. For small values of the aspect ratio $\beta \ll 1$, the approximation $\mathrm{F}_v \simeq 5\beta/(18\pi)$ holds, and the term $l_{\mathrm{ex}}/R \ll 1$ can be neglected. In this case, Eq. (5.4) is reduced to

$$\omega_0 = \frac{20}{9}\gamma\mu_0 M_{\mathrm{S}}\beta, \tag{5.7}$$

which shows a linear dependance of the gyromagnetic frequency with the aspect ratio for small values of β, see Fig. 5.6.

5.2.3 Excitation of the Vortex Core

Following the experimental observation of the gyrotropic mode, Van Waeyenberge et al. [2006] achieved polarity reversal exciting the disk with a short burst of an alternating field at the characteristic frequency. In this scheme, a permalloy square with flux closure domain was excited at the characteristic frequency with a small 0.1 mT sinusoidal field, and the gyroscopic motion of the domain walls was time recorded with XMCD. As the square was excited, a short burst (4 ns) of high field, 1.5 mT, at the same characteristic frequency was sent. Before the burst, they observed a circular CCW motion of the center of the domains. After the burst, the motion was reversed to CW. Because the sense of gyration is solely determined by the polarization of the core, it follows that the core had been reversed.

Posterior experiments showed the possibility to produce the core reversal with other kind of excitations, such as spin-polarized currents [Caputo et al. 2007], in-plane rotating magnetic fields [Curcic et al. 2011], or high-frequency excitations

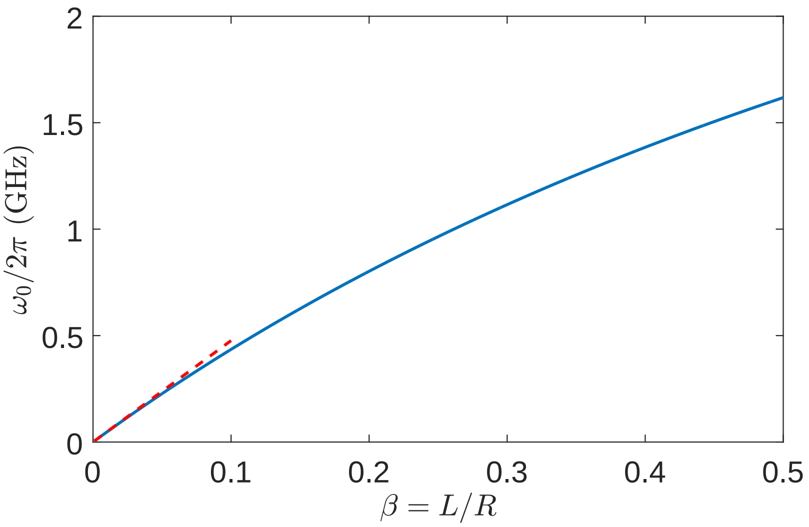

Figure 5.6: Frequency as a function of aspect ratio according to Eq. (5.4) and substitutions of the 2VM of Eq.(5.5). (Dashed red) Linear approximation for small values of β, according to Eq. (5.7). Values for calculation are typical for Py: $M_{\mathrm{S}} = 7.65 \cdot 10^5$ A/m, $\gamma/2\pi = 28$ GHz/T, and $A = 13 \cdot 10^{-12}$ J/m.

[Kammerer et al. 2011]. In this case, the reversal is produced due to the interaction between the spin waves on the system and the domain wall. The senses of gyration (CW or CCW) of the vortex chirality and the high-frequency excitation determine whether the reversal is produced.

Physics of the reversal process is complex because it involves thousands of interacting spins. The reversal process is nonlinear, contrary to the linear motion explained in the previous section. For the case of an excitation at ω_0, the reversal process begins once the excitation on the vortex core is large enough to overcome a critical velocity of the core, v_{c} [K.-S. Lee et al. 2008]. Then, a region with opposite magnetization begins to grow in the magnet, up to the point in which a vortex-antivortex pair with opposite magnetization is created. Finally, the new antivortex collapses with the old vortex and spin waves are generated [Kammerer et al. 2011]. The characteristic frequency of the new state is the same as the old one, but the core oscillates in the opposite sense. With the spin-wave excitation scheme, the critical velocity is not a valid threshold to determine the reversal because of the spin wave-vortex interaction.

Barman et al. [2010] reported the frequency splitting in magnetostatically coupled magnetic vortices. They attributed the splitting to magnetostatic interactions produced by the in-plane magnetization. The volume charges on each dot change as the vortex core rotates. Because the sense of rotation is determined by the core polarity, the volume charges between parallel and antiparallel cores of the interacting dots are different and produce a frequency splitting of the gyrotropic mode. Jain, Novosad, et al. [2012] drove the interacting dots to a high microwave power of 10 dBm at the characteristic frequency of one of the modes. After reducing the power, only the peak associated to the other mode was observed. During the excitation, the cores continuously reverse their polarization until, eventually, the relative polarization is reversed. When this occurs, the excitation is no longer at the characteristic frequency of the system and, hence, the system remains stable. With this excitation scheme, a controllable ground state is achieved.

5.3 Experiments on Ferromagnetic Ellipses

5.3.1 Experimental Details

First, we patterned shorted CPW on a GaAs substrate using optical lithography (with an MA6 mask aligner), sputtering 100 nm of Au and doing lift-off. Second, we patterned ellipses of 2.2 x 1.3 μm^2 on top of the central line using electron beam lithography (with a Raith 150), used electron beam evaporation to deposit 50 nm thick Py ($Ni_{81}Fe_{19}$), and lift-off. The long axis of the ellipses is along the direction of the CPW, and hence perpendicular to the rf field, and there are about one thousand in the 3-mm-long central line.

The CPW is mounted between the poles of an electromagnet that can apply fields up to 300 mT. The sample can be rotated to change the direction of the field. A probe contacts the sample to a vector network analyzer (Agilent Technologies E5061A), used to measure the spectral properties and to send excitation pulses. Figure 5.7 shows the typical measuring configuration. The domain structures are imaged with MFM (DI 3000) operating in the lift mode and using a low-moment magnetic tip to avoid tip-sample interactions.

Reflection spectra are measured as a function of field, using the broadband-FMR technique [Denysenkov et al. 2003]. In this technique a broad frequency range is measured at fixed field steps. In order to obtain the spectra, a reference is always taken at -100 mT. This field is high enough to saturate the sample, and hence the recorded spectrum is produced by the impedance of the circuit and the sample. The reference spectrum is used to normalize the subsequent spectrum. As the field is reduced and the vortex is created, the magnetization precession changes the impedance of the circuit. At the resonant frequencies, the change in impedance is maximum and it appears as maximum in the normalized spectrum.

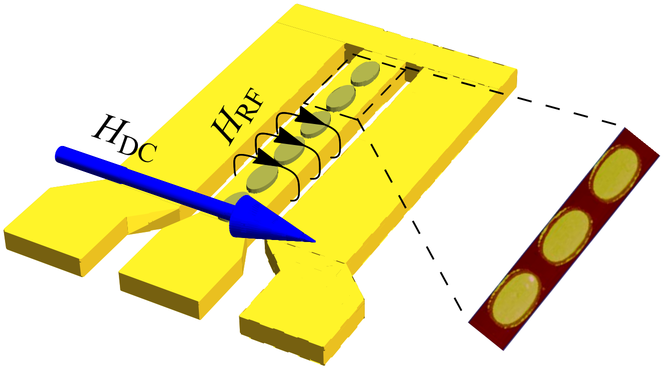

Figure 5.7: Schematics of the grounded CPW with $2.2 \times 1.3\ \mu\mathrm{m}^2$ ellipses on top of the central line. The rf and dc fields are perpendicular to the long axis.

5.3.2 Results

Figure 5.8 shows a measurement in which the field was swept up from -100 mT, with the field parallel to the short axis. Three distinctive peaks can be observed. First, an almost symmetric, intensive peak around 0 mT that increases linearly with the magnitude of the external field (V shape), beginning at 100 MHz and dying out at around 300 MHz. Second, a nearly flat peak from -15 mT to 20 mT (tilde-shape), at 300 MHz. And third, a small peak that increases linearly from -10 mT to 20 mT, starting at 200 MHz and dying out at 300 MHz.

The resonance frequency of a single vortex in an ellipse increases linearly for both positive and negative fields, producing the V shape [Buchanan et al. 2006]. On the other hand, if the external field is applied along the long axis, the vortex core moves on the perpendicular, short axis, and the frequency is neatly field-independent. This is related to the energy landscape of the ellipse in each direction. In the long axis, a different profile is met as the core is moved. At the center, the core moves in a broad movement but, as it is moved to the edge, the movement is narrower and hence the frequency increases. This is not the case in the short axis, where the movement is almost the same in all the process. This latter case is similar to the vortex in a disk.

The other two peaks are related to the resonances of a two-vortex state. In this case, the frequency increases with the applied field, but not as much as in the one-vortex state, as it was studied in [Buchanan et al. 2005; Jain, Novosad, et al.

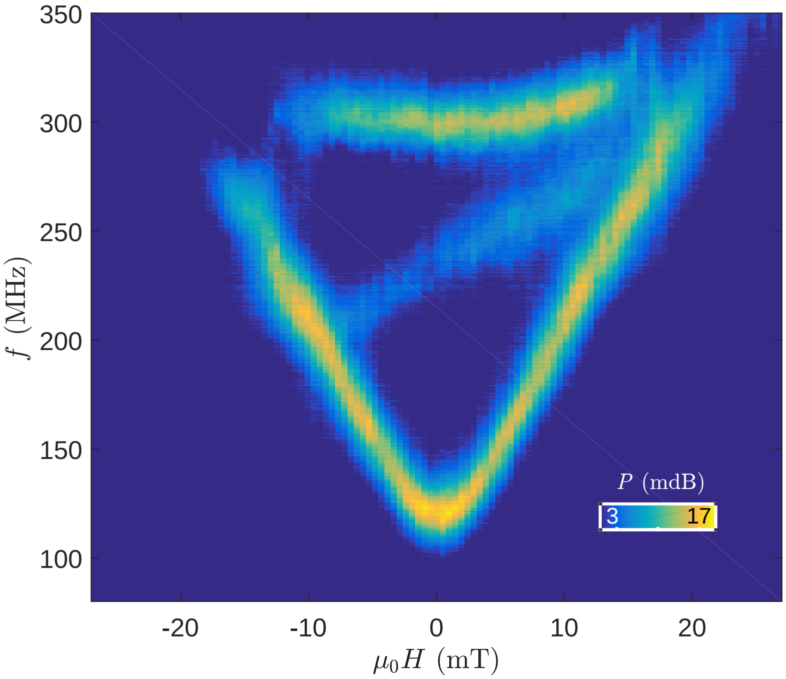

Figure 5.8: Reflection spectra map of an array of 2.2×1.3 μm^2 ellipses, with an applied field in the short axis.

2012; Jain, Schultheiss, et al. 2012]. Figure 5.9 shows the spectra of an array of ellipses with the long axis perpendicular to the CPW central line; the rf and dc fields are applied along the long axis. Two peaks appear at 200 MHz and 300 MHz, corresponding to the two-vortex state, and at similar frequencies as in Fig. 5.8. In the two-vortex resonance, the field dependance of the peak is less pronounced than in the one-vortex resonance, as expected. Difference in the peak position is attributed to ~ 10 % difference of sample sizes. Difference in field dependance is due to the relative angle between rf field and the axis of the ellipse.

The first sample was also imaged with MFM after saturation in the long axis, and the images confirmed the presence of ellipses with one and two vortices, Fig. 5.10. Because the MFM is sensitive to field gradient, it is not a direct image of the magnetization pattern. We simulated the field gradient produced by one and two vortices at a distance of 100 nm from the sample surface to have a clear image of the expectable images. The simulated and measured images (Fig. 5.10) are essentially the same, only differing in experimental noise and the imperfect shape from fabrication.

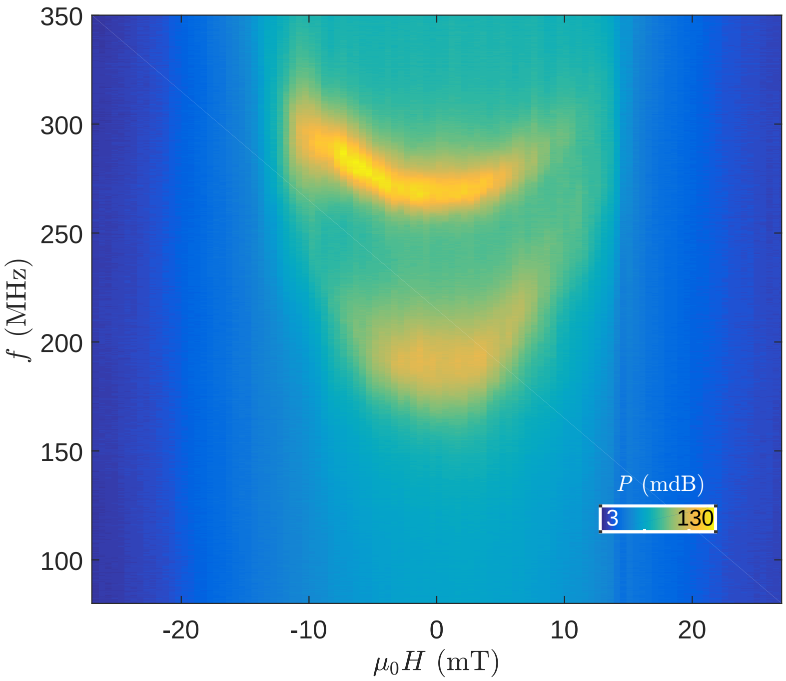

Figure 5.9: Reflection spectra map of an array of 2.2 x 1.3 μm^2 ellipses, with an applied field in the long axis.

Ellipses with two vortices resemble the system of two interacting dots, thus we expect similar behavior to studies in [Jain, Novosad, et al. 2012; Jain, Schultheiss, et al. 2012]. We excite the ellipses with the resonant spin ordering technique (ReSO) [Jain, Schultheiss, et al. 2012]; first, we fix the frequency of the excitation sent to the dots, then the power is increased (up to 10 dBm) so the vortex core reverses continuously. Finally, the power is decreased back to the linear regime. By doing this, only one of the two peaks associated to the two different relative polarizations survives: all the ellipses have switched from $p_1 p_2 = +1$ (-1) to $p_1 p_2 = -1$ $(+1)$. This is shown in Fig. 5.11 for the two excitation frequencies. When one peak is excited, the height of the other one increases, indicating transition between states.

We do now excite the system at 120 MHz—the one-vortex frequency. In this case, the one-vortex peak disappears, as shown in Fig. 5.12. In this case, however, we do not observe the appearance of any peak in the measured frequency range, and the height of the two other peaks remain unchanged. This confirms that the excitation is weaker than the stray fields determining the outer spins

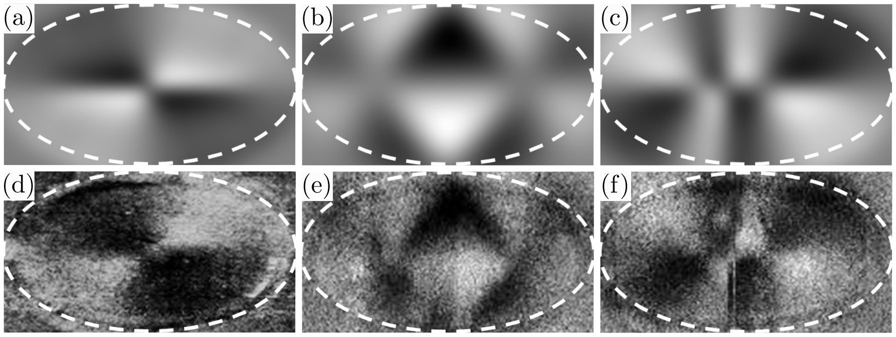

Figure 5.10: Simulated (a)–(c) and measured (d)–(f) MFM images of the ellipses using a low-moment tip, corresponding to one vortex (a) and (d), two vortices (b) and (e), and a vortex-antivortex-vortex (c) and (f).

circulation—winding number—, and transition to the two vortex state is impossible. We characterize the post-ReSO state with MFM images. The images do not reveal the presence of even a single ellipse possessing the one-vortex state. Instead, we can see the appearance of a new MFM pattern, Fig. 5.10(f). Comparing the measured image with a simulated MFM of the v-av-v state we can conclude that we produce this state, Fig. 5.10(c).

5.3.3 Discussion

We prove that subjecting a single vortex to a large amplitude rf field results in a v-av-v state. As explained in [Curcic et al. 2011; Kammerer et al. 2011], the dynamically driven core reversal is a strongly non-linear process. It is accompanied by the nucleation and annihilation of the v-av pair [Guslienko, K.-S. Lee, et al. 2008; Hertel et al. 2006; Van Waeyenberge et al. 2006; Xiao et al. 2006], followed by a spike of spin wave generation. When a disk-shaped structure is subjected to a continuous rf excitation with a strong enough amplitude, the core undergoes reversal twice during one period on average, and the switching lasts indefinitely since the vortex remains resonantly coupled to the excitation field independent of the core polarity. In an ellipse, the geometry favors lateral motion of the vortices along an easy axis, and, therefore, it is possible to encounter a situation when two vortices and an antivortex are physically separated far enough to avoid collision and subsequent annihilation. As soon as this scenario occurs, the system decouples from the excitation fields and stabilizes in a newly acquired state. The winding number for the initial (one vortex) and final (v-av-v) states remains the same.

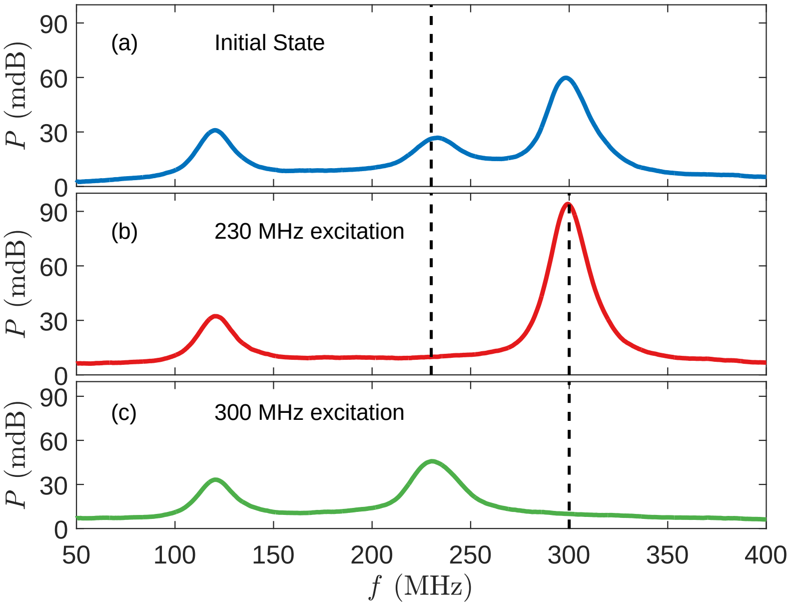

Figure 5.11: Reflected power as a function of frequency after saturation of the ellipses along the short axis at zero field (a). After ReSO excitation at 230 MHz (b) and 300 MHz (c), the corresponding peak disappears.

5.4 Experiments on Stadium-Shape Ferromagnets

Our studies from the previous section, however, leave an unanswered question. The v-av-v state is characterized by three cores, and we should be able to dynamically excite them with the same experimental arrangement as used in our studies of single- or double-vortex states. Thus, it is not clear why, after suppression of the 120 MHz resonance, there were no new peaks detected that could be assigned to the v-av-v state. While the inter-dot dipolar interaction in closely spaced dot arrays induces an additional in-plane anisotropy [Novosad, Guslienko, et al. 2002] and affects the vortex stability [Kakazei et al. 2003], it is not expected to play any significant role here since the ellipses are separated an enough distance. Previous studies show that the magnetization reversal modes in ferromagnetic ellipses [Vavassori et al. 2004], as well as in stadium-shaped elements [Castillo-Sepúlveda et al. 2012; Corona et al. 2012], may include nucleation of one or two vortices depending on the geometric aspect ratio. Hence, we fabricated stadium-shape samples to avoid two-vortex state formation. This would significantly simplify the analysis and might help to improve the detection limits of the experiment.

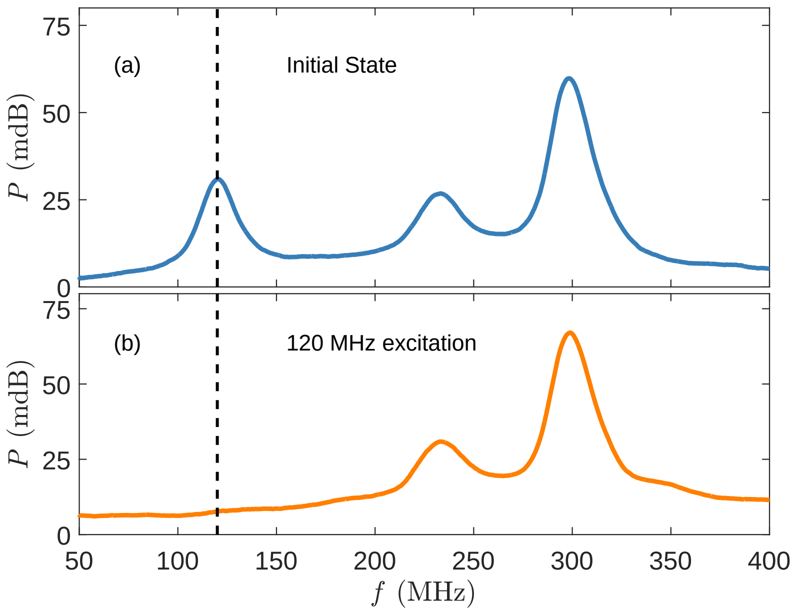

Figure 5.12: Reflected power as a function of frequency after saturation of the ellipses along the short axis at zero field (a). After ReSO excitation at 120 MHz (b), the corresponding peak disappears.

5.4.1 Experimental Details

We fabricated stadium-shape ferromagnets on top of CPW. The fabrication process is the same as in the previous section. As it was studied in [Castillo-Sepúlveda et al. 2012; Corona et al. 2012] with micromagnetic simulations, these shape favors the formation of v-av-v structures. The stadium shape is formed by two semicircles joined by a rectangle.

We fabricated two sets of $1 \times 2\ \mu\text{m}^2$ Py samples of 70 and 90 nm thickness, each set consisting of samples aligned parallel and perpendicular to the CPW. The broadband-FMR technique explained above was used to obtain the spectra of the stadium-shape samples. In this case, the reference was taken at -300 mT. We measured the spectra with an Agilent Technologies E8361A Network analyzer. MFM images of the stadium-shape samples are taken with an AFM model MFP-3D from Asylum Research.

5.4.2 Results

We took MFM images of the samples to identify their magnetization configurations. In the 70 nm set, we identified samples being in the two-vortex and v-av-v states, Fig 5.13. It is surprising that the v-av-v state is a ground state of the system without any previous manipulation.

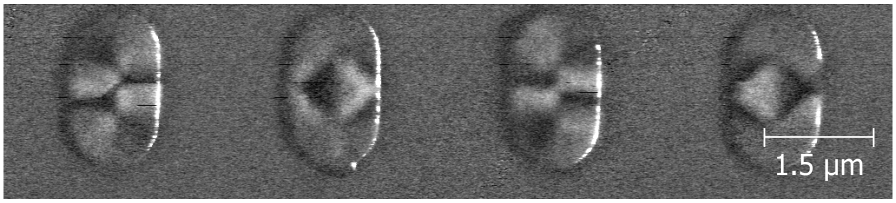

Figure 5.13: MFM image of the samples with 70 nm thickness. Two different ground states can be observed: v-av-v (first and third samples), and two-vortex states (second and fourth samples). Different contrast means that the in-plane curling magnetization can also be in every possible configuration (CW and CCW).

We measured reflection spectra as a function of the magnetic field, Fig. 5.14. The spectral measurement shows peaks (red in Fig. 5.14) and valleys (blue in the figure) in the region -40 mT $< \mu_0 H <$ 40 mT and around frequencies of 400 MHz, and they are not symmetric around zero field. These are signs of flux-closure domain formation and excitation. However, we cannot identify traces of any of the previously studied excitation frequencies. Because the measured spectra of the v-av-v is rather complex, it is necessary to simulate further the system to reproduce the field dependency of the characteristic frequencies. A recent study [Ding, Jain, et al. 2015] suggests that the excitations in these systems are manyfold, with characteristic frequencies for all the relative orientations of the cores.

Images of the 90 nm set revealed a different configuration, Fig. 5.15(c). In these images we see an in-plane magnetization, characterized by the low contrast, and an out-of-plane magnetization along a central line, characterized by the dark region. We measured samples with opposite magnetization of the central line. As explained before, it is not possible to easily make correspondence between an MFM image and the magnetization distribution of a sample, because the MFM is sensitive to the field gradient perpendicular to the plane, $\partial m_z / \partial z$.

5.4.3 Micromagnetic Simulations

With the goal of identifying the magnetization distribution, we simulated the samples micromagnetically using MuMax3 [Vansteenkiste et al. 2014]. The simulated

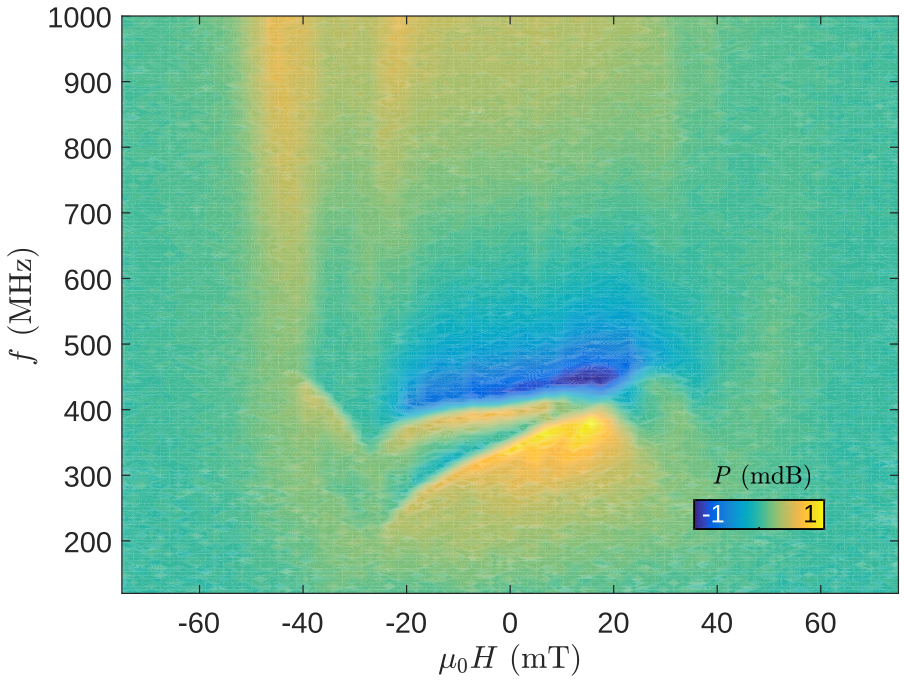

Figure 5.14: Reflection spectra of a stadium-shape sample after saturation. The field is applied in the short axis.

shape was chosen to be the same as in our samples. Magnetization was initialized to a vortex state around the center, and we let the system relax to the equilibrium remanent state with a small out-of-plane field to break symmetry between positive and negative out-of-plane direction (Z axis). The simulations revealed a state in which magnetization curls following the edges, but a central line points out of the plane, Fig. 5.15(a). A computation of the field gradient at a 100-nm distance from the sample, equivalent to the MFM tip distance used in the measurements, revealed that this is indeed the state of our samples, Fig. 5.15(b). A different code is needed for this computation, because MUMAX3 code is only valid for MFM images of 2D samples. The code for the MFM of the 3D sample was adapted from OVF2MFM code by R. Boardman, K. Lebecki and H. Fangohr under GPLv3. A deeper analysis of the simulated state reveals that the central line (or stripe) moves along the thickness of the sample. On one surface, the magnetization of the stripe comes out at a single point and it is in the other side on the opposite surface —these are the magnetization caps—, see the white central region of Fig. 5.15(d). If the magnetization distribution is observed at only one surface, it may seem a vortex centered on one of the semi-circles.

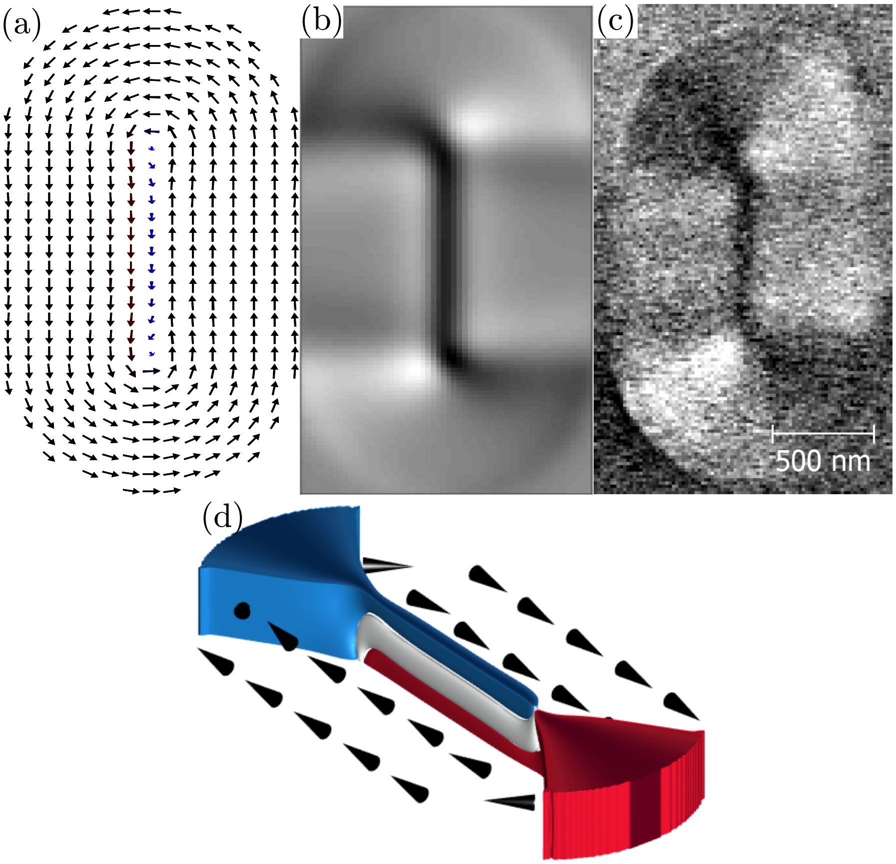

Figure 5.15: Comparison between the simulated MFM image at 100 nm (b) of the magnetization configuration of (a) with the measured MFM image (c), for a sample of 90 nm thick. (d) Thickness dependence of the simulated magnetization. The blue color represents regions where $m_y \geq 0.8$, the red color regions where $m_y \leq 0.8$. A central line can be observed, with $m_z \geq 0.7$, that propagates through the sample.

The magnetization of the stadium-shape samples was also simulated as a function of field in both long-(X-) and short-(Y-) axis directions. The initial magnetization configuration is the one showed in Fig. 5.15(d)—also showed in Panel 0 of Figs. 5.16 and 5.17—. For the case of an applied field in the X axis, H_x, the increasing m_x displaces the central line towards the edge in the perpendicular Y axis and, at the same time, m_z increases (Panel 1 on Fig. 5.16). At a field value H_{an}, the line reaches the edge and breaks; a sudden decrease in m_z is observed, along with an step increase in m_x indicating the particle is almost in the SD state (Panel 2). However, a small out of plane component decreases and becomes negative (Panel 3) before becoming a complete SD (Panel 4). As H_x is decreased, the SD becomes a flux-closure magnetization at H_n. In this case, the closure structure consists of two vortices with opposite chiralities and polarities (Panel 5), and hence the total m_z remains close to 0 along all the sweep down. Note that, even in this state, there is a thickness-dependent structure.

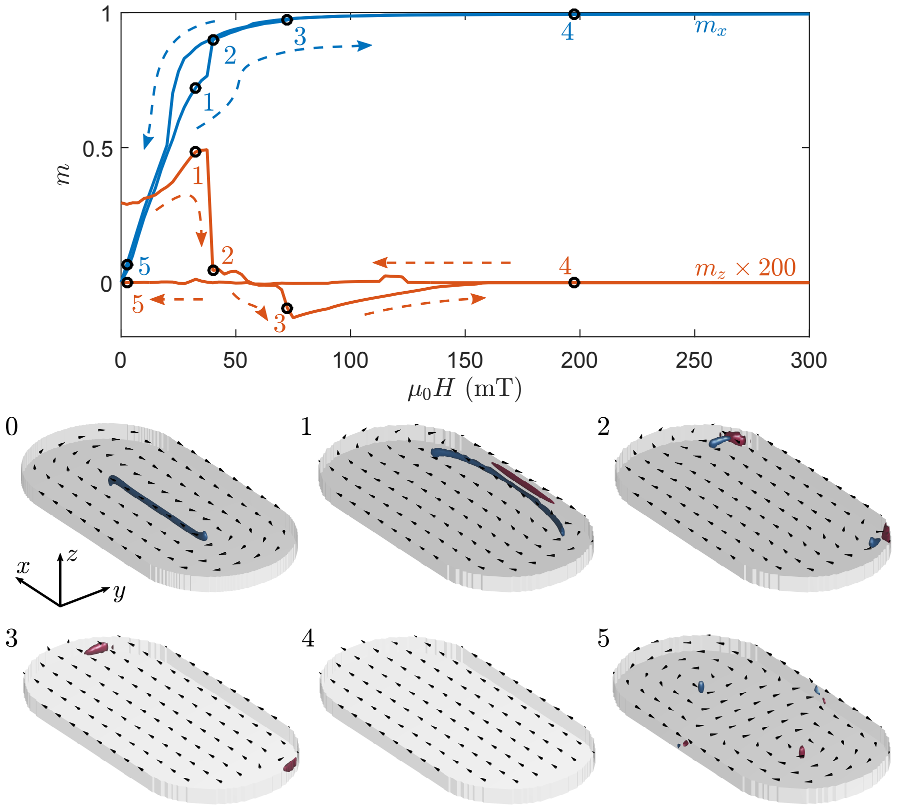

Figure 5.16: Magnetization as a function of field in the X direction, for a sweep 0 mT → 300 mT → 0 mT. m_x (blue curve) and m_z (orange curve) are plotted. The arrows indicate the direction of the sweep. The magnetization state at the beginning and at the 5 indicated points in the sweep are plotted in panels 0 to 6.

Figure 5.17 shows the case of an applied field in the short axis, Y. In this case, the elongated stripe with m_z moves to the edge in the Y axis (Panel 1). Near the edge, the stripe deforms and elongates following the circular shape (Panel 2) until it brakes and a SD is formed (Panel 3) at field value H_an. When the field is swept down, the flux-closure magnetization begins to form in the edges, with small regions having opposite m_z (Panel 4). The flux-closure domain is formed at H_n. In this case, the formed stripe with m_z has the caps in the same semi-circle on both surfaces (Panel 5). If the field is further decreased, one of the caps shifts to the opposite semicircle and a step decrease in m_z is produced, being the final state the same as the initial.

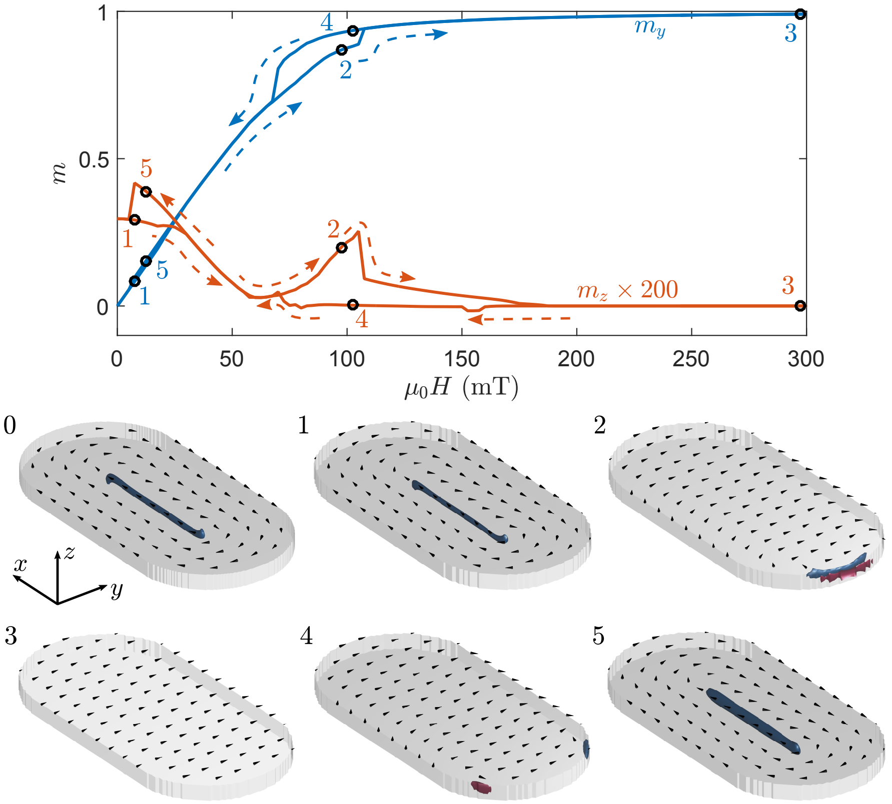

Figure 5.17: Magnetization as a function of field in the y direction, for a sweep 0 mT → 300 mT → 0 mT. m_y (blue curve) and m_z (orange curve) are plotted. The arrows indicate the direction of the sweep. The magnetization state at the beginning and at the 5 indicated points in the sweep are plotted in panels 0 to 5.

5.4.4 Discussion

Three-dimensional micromagnetic simulations of magnetic confined elements were done in [Boust et al. 2004; Lv et al. 2013; Pribiag et al. 2007; Vukadinovic and

Boust 2007; 2008; Vukadinovic, Boust, and Labbé 2007; Yan et al. 2007; B. Zhang et al. 2010] and experimentally observed in [Cheynis et al. 2009; Ding, Jain, et al. 2015; Ding, Kakazei, et al. 2014; Masseboeuf et al. 2012]. In particular, Arrott et al. [2010], Cheynis et al. [2009], Lv et al. [2013], Masseboeuf et al. [2012], and Yan et al. [2007] studied elongated samples as the ones studied here. Yan et al. [2007] simulated rectangular samples and presented a simple model in which the 3D gyrotropic mode rotates as a string with different nodes. For the fundamental mode, the 3D object rotates in phase. In the first-order mode, characterized by a node in the center of the 3D core, the top and bottom surface rotation has a phase of π rad. For the second-order mode, characterized by two nodes, there is again no phase difference. Alongside with this simple scheme, there are more complicated excitation modes that come from other inhomogeneous magnetization regions such as corners and 90° domain walls. In their study, these modes are typically higher in frequency. Cheynis et al. [2009] controlled the magnetization in the central region—the Néel cap– using an external magnetic field. The magnetization in the central region is a Néel domain because the magnetization rotates between opposite directions in the plane. Without an external field, it is of opposite sign on the other surface. Our simulation of stadium-shape samples reveal a similar magnetization configuration.

In our simulations, we also observed an state characterized by the formation of a vortex-antivortex-vortex-antivortex-vortex (v-a-v-a-v), with m_z propagating through the thickness. However, in the center of the thick sample, there are no defined out of plane cores, but an elongated line similar to the state described above, see Fig. 5.18. In this case, the simulated MFM image shows a similar pattern to the one measured in thin samples, with rigid cores, as the one in Fig. 5.10(c). However, a small difference appears: in the case of rigid vortex, there is a straight line separating the regions with high contrast along the Y directions, while in the case of thick vortex a sinuous shape is observed.

Let us bring our attention back to Fig. 5.13. The first and third samples are attributed to v-av-v configurations. A comparison between these two samples, though, shows that the first one has a sinuous modulation of the center (dark contrast region) while in the third there is a straight line. We attribute this to the two different possibilities: in the first sample the cores would propagate through the thickness and elongate in the center, and the third sample would have rigid cores. This would prove that even if the MFM images are very similar, the difference would still be measurable.

MFM measurements and simulations show the importance of taking into account the thickness of the samples. On a thin sample, the vortex core can be modeled as rigid along the thickness. However, if the thickness is increased, the magnetization on the core widens on the central part of the sample, and the dynam-

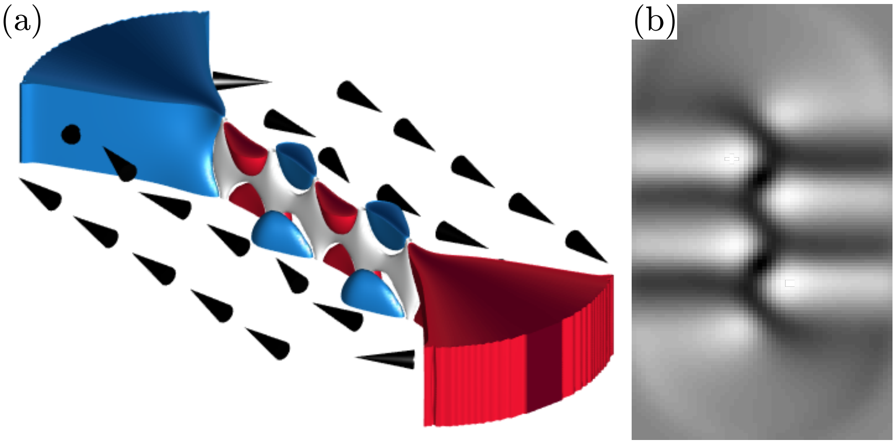

Figure 5.18: (a) Simulated thickness dependence of a v-a-v-a-v configuration in a thick sample.The blue color represents regions where $m_y \geq 0.8$, the red color regions where $m_y \leq 0.8$. The cores, with $m_z \geq 0.7$, propagate through the sample and join in the center.(b) Simulated MFM image at 100 nm from the surface

ics must take it into account. Zarzuela, Chudnovsky, and Tejada [2013] propose the appearance of a characteristic frequency due to the thickness, and it was measured in experiments of thick disks in [Ding, Jain, et al. 2015; Ding, Kakazei, et al. 2014]. However, in elongated samples, it is much more difficult to identify the excitation modes in the experimental spectra. Not only does a single element have various excitations, but also the modes from different ground states—such as the ones proposed in [Yan et al. 2007]— contribute to the total measured spectra.

Our MFM measurements with an applied field also reveal the possibility to fully reverse the central line with an external perturbation (the MFM tip), and the possibility of partial reversal of the central line. The mechanisms of this reversal should be further studied, because they imply high-energy changes.

5.5 Conclusions

We have studied the vortex system in different geometries measuring the reflection spectra as a function of field and taking MFM images. We have used nanofabrication techniques to pattern the samples on top of CPW for this purpose. Two different elongated systems have been studied: ellipses and stadium-shape ferromagnets. In ellipses, we found a reflection spectra that we could identify with the magnetization being in the one-vortex or two-vortices states. We have driven the system to a high-power excitation and produced transition from one-vortex to v-av-v state. We have observed the appearance of the new magnetization states in the MFM images and in a change in the reflection spectra. However, we have not been able to identify the characteristic frequencies of the new state. We argue that the presence of the two-vortex mode is hiding the new state.

We have fabricated stadium-shape samples because they are good candidates to stabilize the v-av-v configuration in the ground state. We have measured reflection spectra and taken MFM images. We could not identify any characteristic frequencies in the reflection spectra. We attribute this to the fact that the samples can be in a variety of states, as revealed by MFM. Moreover, these states have 3D magnetization patterns and more modes appear in the excitation. We have simulated the system using micromagnetics and obtained the behavior when an external field is applied, which is in good agreement with the MFM measurements.

Further studies are required to understand better both systems. First, a better shape for the observation of v-av-v. We have observed that the stadium shape stabilized the v-av-v state, so finding the optimal parameters of thickness and aspect ratio would improve the experiment. Second, thickness of ferromagnetic elements should be taken into account.

6

Magnetic Doplet Solitons in Thin Films

Under certain factors, magnetic domains can also be generated with electrical currents. Dissipative droplet solitons are generated in nanocontacts to thin films with low current densities and low external magnetic fields, which supposes a great advantage over magnetic storage devices due to their scalability. Solitons are interesting dynamical systems because of their stability. It was not until a few years ago that these objects could be detected experimentally. However, in those experiments they observed a partial reversed magnetization that was not completely explained. We have studied the droplet generation at room temperature in dc and ac regimes. Specially, we have studied the low-frequency response that had not been previously reported. The low-frequency dynamics in this kind of objects typically reveal the existence of a domain wall movement. Such a movement may be due to the droplet as a whole, showing the high stability of the object. This may lead to new ways of controlling the droplet, and being able to move it would allow transport of information. Our low-frequency spectral measurements and micromagnetic simulations reveal that the droplet drifts due to asymmetries in the nanocontact, which explains why the fully-reversed droplet was not measured in previous experiments. Further, we argue that , at lower temperatures, the increased pinning effects would fix the reversed spins and, hence, stabilize the droplet.

6.1 Introduction

Solitons are localized excitations that occur in dynamical systems. In the case of magnetic solitons, these local excitations are produced by an attractive potential of the spin waves occurring from the precession of the magnetization around equilibrium, when there is no damping [Kosevich et al. 1990]. They consist of localized reversed spins that are stabilized due to a dynamic balance of energies. These solitons can be characterized by the topological charge. Magnetic vortices studied in the previous chapter have a topological charge $\mathcal{Q} = 1/2$, and are magnetically stable. Droplet solitons, on the other hand, are nontopological excitations. Real materials have non-zero damping, making complicated the existence of magnetic solitons. Dissipative droplet solitons, however, can be generated in materials with damping thanks to the spin-torque effect [Slonczewski 1996] that allows excitation of spin waves in a magnetic stack [Slonczewski 1999] and compensates the damping [Hoefer, Silva, et al. 2010]. These short-wave localized excitations are produced with a nanocontact to a thin film, in opposition to long-wave propagating excitations as the ones studied in Chapter 5. Because this short-wave excitation is produced with a current, an additional term must be included in the Landau-Lifshitz equation to account for the magnetotransport: the Sloncwezski term. Several applications for such objects have been proposed [Bonetti and Åkerman 2013; Locatelli, Cros, et al. 2014], based not only on the capability to store magnetic states [Macià, Kent, et al. 2011], but also exploiting the dynamic behavior of the droplets as oscillators. Droplet solitons are an interesting and recently discovered system englobed in the field of spintronics. Spintronics is the field that exploits the transport of the spin in materials, whereas electronics uses the transport of the charge of electrons. Spintronics is an exciting field because it adds a controllable degree to electronics, hence empowering the applicabilities. The dynamics of the spins in this field is of great importance because it allows faster devices.

First measurements of magnetic droplet solitons at room temperature proved the abrupt threshold of the excitations and showed that precession frequencies were below the FMR frequency [S. Chung et al. 2014; Mohseni, Sani, Dumas, et al. 2014; Mohseni, Sani, Persson, et al. 2013], but there was no evidence for fully reversed magnetization beneath the nanocontact. On the other hand, measurements at low temperature showed that the predicted reversal of the magnetization occurs almost completely [Macià, Backes, et al. 2014].

Backes et al. [2015] and Bonetti, Kukreja, et al. [2015] imaged the droplet excitation with XMCD. A difference between the absorption of light with opposite helicities beneath the nanocontact reveals the presence of a region with reversed magnetization, i.e. a droplet. This technique allows the measurement of the time evolution of the magnetization with 50 ps time resolution.

Our goal is to characterize the stability of the droplet soliton and give explanation to the discrepancy in the amount of reversed magnetization. We have measured point contacts in a ferromagnet and observed hysteretical behavior in the droplet even at room temperature. Furthermore, by measuring the low-frequency dynamics in the soliton—detected electrically—we argue to have observed drift instabilities in the droplet. This kind of instabilities are caused by small asymmetries in the system, which generate an effective in-plane field. Micromagnetic simulations of the system confirmed that the drift instabilities force the solitons to shift out of the nanocontact and to annihilate as a new soliton is created in the center of the contact.

6.2 Background

6.2.1 Giant Magnetoresistance and Spin-Transfer Torque

Magnetoresistance (MR) is the change in the electrical resistance of a material when an external magnetic field is applied. This dependance may have different origins, and different types of MR are named in accordance: *anisotropic magnetoresistance* (AMR) [McGuire et al. 1975], *giant magnetoresistance* (GMR) [Baibich et al. 1988; Binasch et al. 1989], or *tunneling magnetoresistance* (TMR) are some examples [Julliere 1975; Miyazaki et al. 1991].

GMR is observed in multilayers that can have their relative magnetizations parallel (P) or antiparallel (AP). In the P-state, the resistance is lower than in the AP-state, and may take variations of up to 50 %. This is produced by a difference in the scattering properties of electrons having their spins parallel or antiparallel to the magnetization of the layer, see Fig. 6.1. Electrons with their spin antiparallel to the magnetization (*majority electrons*) have a lower scattering, and hence produce a low resistance. On the contrary, electrons with their spin parallel to the magnetization (*minority electrons*) have a higher scattering, and hence produce a high resistance. This is showed in the bottom of Fig. 6.1. An incident current, in general, is a superposition of electrons with parallel and antiparallel spins, so one must take into account the scattering of both components when traversing the multilayer. In the P-state, the circuit sketched in the bottom part of Fig. 6.1 has a total resistance lower than the circuit corresponding to the AP-state. This effect is specially useful because the magnetization of one layer may be controlled with, for example, an external field, which allows a control on the measured resistance. This led to a revolution in electronics, and Albert Fert and Peter Grünberg jointly received the Nobel Prize in 2007 for the discovery of GMR [Baibich et al. 1988; Binasch et al. 1989].

In 1996, Slonczewski [1996] described the *spin-transfer torque* (STT), a consequence of the difference in transmission and reflection of majority and minority electrons. STT appears when a magnetic layer is traversed by a spin current with polarization $\vec{m}_{\mathrm{p}}$. The STT is produced at the interface between a non magnetic metal (NM) and a ferromagnet (FM). Majority electrons will transmit to the FM and minority electrons will reflect easier. Each electron is, in fact, a quantum superposition of the parallel and antiparallel components to the FM magnetization

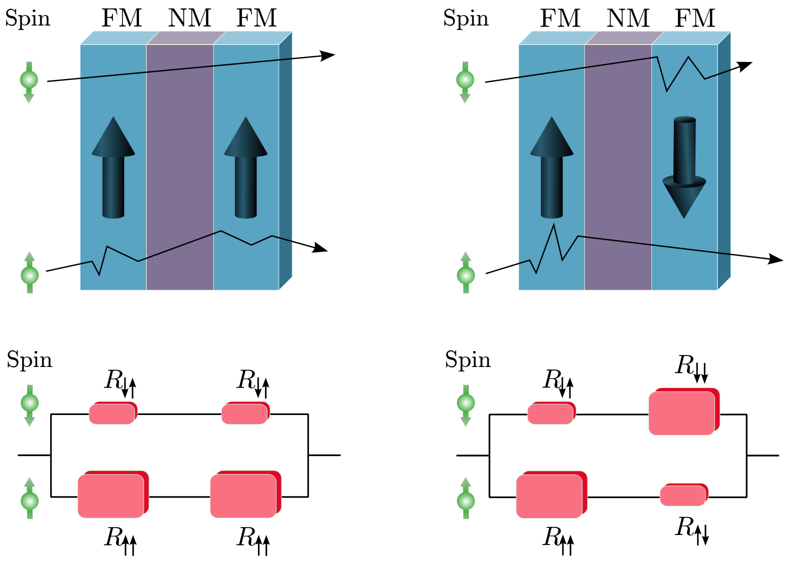

Figure 6.1: GMR effect in a multilayer consisting of two ferromagnetic (FM) layers and a non magnetic layer in between (NM). Electrons scatter differently according to the orientations of their spins. The scattering may be considered as an equivalent resistance. Adapted from "Spin-valve GMR" by Guillom, used under CC BY-SA 3.0.

$\vec{m}$. As a consequence, the transverse part of the incident spin current is absorbed by the FM interface. Because of conservation of the angular momentum, a response torque $\vec{\tau}$ is exerted on the FM, its direction defined by

$$\vec{\tau} = a_J \vec{m} \times (\vec{m} \times \vec{m}_{\mathrm{p}}) + b_J \vec{m} \times \vec{m}_{\mathrm{p}} \,. \tag{6.1}$$

The first term is the STT, acting in the same direction as the damping, and the second term is known as the *field-like torque* because it acts in the same direction as the effective field. Typically, the field-like torque term is much smaller than the STT term [Brataas et al. 2012; Xia et al. 2002; Zimmler et al. 2004] and contributes to slow down or accelerate the dynamics, see Fig. 6.2. The subindex J of the parameters a_J and b_J denotes the dependance of the torque on the current density, i.e. the parameter changes strength and sign according to the current density.

The most common configuration for spin-transfer torque devices is a layer stack made of two FM layers separated by a NM layer that decouples the two FM layers. The first FM has a fixed magnetization and acts as a *polarizing layer* (PL), aligning all the electron spins in the same direction. The polarized electrons act on the other FM layer—the *free layer* (FL)—via the STT. Depending on the direction of the current, the net force acting on the FL changes the relative orientation between the

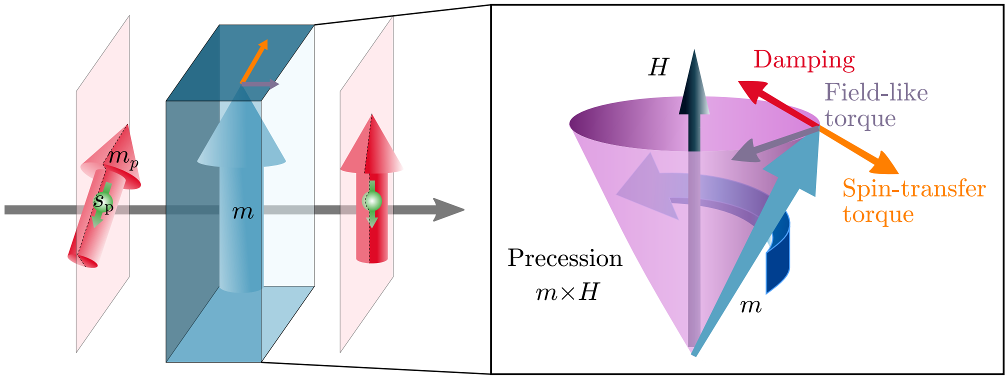

Figure 6.2: (a) Direction of the spin-transfer torque and the field-like torque caused by an incident polarized electron and (b) damping acting on the rotation of the magnetization $\vec{m}$ around the effective field $\vec{h}_{\text{eff}}$.

magnetic layers, and hence produces a change in the resistance, typically through the GMR. Fixing the layer magnetization of the PL is typically achieved by making the layer thickness higher than the other layer's, therefore the STT that produces the FL is small to initialize dynamics in the PL.

High-current densities are needed to produce the excitation in the FL, $\sim 10^6$ – 10^7 A/cm^2. In order to achieve these high densities, different configurations are used, see Fig. 6.3, which allow dissipation of the heat produced by this high-current densities. In the *nanocontact* configuration (Fig. 6.3(a)) a non-magnetic material is used to make contact with a small region—the nanocontact—of an extended magnetic layer. In the *nanopillar* configuration (Fig. 6.3(b)) the high density is achieved by directly patterning the magnetic layers in a small region [Brataas et al. 2012]. In this thesis we use the nanocontact approach.

When a current traverses a nanocontact, excitations produced in the magnetic field under the nanocontact region may propagate through the extended magnetic layer up to some extension via spin waves [Slonczewski 1999]. This way, the magnetization under the nanocontact oscillates around the equilibrium position, due to the high exchange produced by all the magnetization in the layer; these are *spin-torque nano-oscillators* (STNO). The exchange in the nanopillar is lower, and hence the magnetization of the entire FL may reverse.

The oscillation of the FL magnetization in STNOs is produced at the characteristic ferromagnetic frequency, and when the torque overcomes the damping a fast switching of the FL magnetization occurs. These systems are interesting because the relative orientation of the layers can be determined with the measurement of the dc resistance, they can work at low fields, and the magnetization reversal is

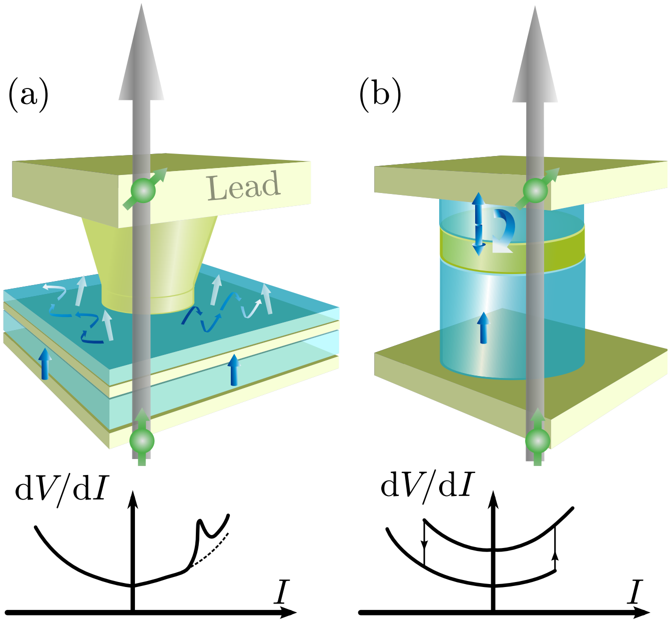

Figure 6.3: Two different approaches to obtain STT on a free layer. (a) Nanocontact, (b) nanopillar with two ferromagnetic materials.

fast ($\sim$ 10 ns). Moreover, because the free layer oscillates around its equilibrium position, an smaller time-dependent change in resistance appears.

Taking into account only the STT and droping the field-like torque, an extra term may be introduced in the LL equation—the Slonczewski term—and the equation turns into

$$\frac{\mathrm{d}\vec{m}}{\mathrm{d}t} = -\vec{m} \times \vec{h}_{\mathrm{eff}} - \eta \vec{m} \times (\vec{m} \times \vec{h}_{\mathrm{eff}}) + \sigma \vec{m} \times (\vec{m} \times \vec{m}_{\mathrm{p}}) \,, \tag{6.2}$$

where magnetization $\vec{m}$ and fields $\vec{h}_{\mathrm{eff}}$ are normalized by the saturation magnetization M_{S}, time is normalized by $2\pi/|\gamma|\mu_0 M_{\mathrm{S}}$, and space by the exchange length l_{ex}. η is the damping, σ is proportional to the normalized current $\sigma = \sigma_0 \kappa(m_z)$ [$\kappa(m_z)$ being the spin torque asymmetry], and $\sigma_0 = I/I_0$ with

$$I_0 = \frac{2M_{\mathrm{S}}^2 e \mu_0 \delta \pi r_{\mathrm{c}}^2}{\hbar \epsilon} \,, \tag{6.3}$$

δ being the thickness of the magnetic layer, r_{c} the point contact radius, and ϵ the efficiency of the spin torque. The spin torque asymmetry is defined as

$$\kappa = \frac{2\lambda^2}{(\lambda^2+1) + (\lambda^2-1)\vec{m} \cdot \vec{m}_{\mathrm{p}}} \,. \tag{6.4}$$

We can see that the second (damping) and third (spin torque) terms of Eq. (6.2) have the same direction when $\vec{h}_{\text{eff}} \parallel \vec{m}_{\text{p}}$, their relative orientations determined by the current polarization, see Fig. 6.2. If the spin torque is parallel to the damping, the magnetization decays to its stable position. On the other hand, if the spin torque is antiparallel to the damping, it compensates the damping for a certain threshold current and the magnetization will not be stable and eventually switch its direction.

6.2.2 Magnetic Solitons

In 1977, Ivanov and Kosevich studied the excitation states of a ferromagnet with an easy axis and without dissipation [Ivanov et al. 1976; 1977]. They found that the magnons generated by the oscillation of the magnetization in an uniaxial ferromagnet interacted in an effective attractive potential that localized the excitation. Kosevich et al. [1990] generalized the problem to 1, 2 and 3 dimensions and studied different anisotropies and antiferromagnets.

Magnetic solitons are defined as stable solutions of the Landau-Lifshitz (LL) equation

$$\frac{\mathrm{d}\vec{m}}{\mathrm{d}t} = -\vec{m} \times \vec{h}_{\text{eff}} - \eta \vec{m} \times (\vec{m} \times \vec{h}_{\text{eff}}) \,, \tag{6.5}$$

$$\vec{h}_{\text{eff}} = \nabla^2 \vec{m} + \vec{h}_0 + \vec{h}_{\text{p}} \,; \tag{6.6}$$

where $\vec{h}_{\text{p}} = (h_K - 1) m_z \hat{z}$ is the normalized effective anisotropy field. In the case of a 2D ferromagnet, as is the case of thin films, and the study in this chapter, the solutions are of the form [Kosevich et al. 1990]

$$\theta = \theta(\rho), \qquad \varphi = \nu\chi + \omega t \,, \tag{6.7}$$

where θ and φ are the angles of the components of the local magnetization vector $\vec{m}$, ρ and χ the polar coordinates, see Fig. 6.4, and ν is an integer $\nu = 0, \pm 1, \pm 2, \ldots$ The function $\theta(\rho)$ satisfies

$$l_0^2 \left(\frac{\mathrm{d}\theta}{\mathrm{d}\rho^2} + \frac{1}{\rho}\frac{\mathrm{d}\theta}{\mathrm{d}\rho} - \frac{\nu^2}{\rho^2} \sin\theta \cos\theta \right) + \frac{\omega}{\omega_0} \sin\theta - \sin\theta\cos\theta = 0 \,, \tag{6.8}$$

with boundary conditions $\theta(\infty) = 0$ and $\frac{\mathrm{d}\theta}{\mathrm{d}\rho}(0) = 0$, $l_0 = \sqrt{A/K}$ being the magnetic characteristic length, ω_0 the ferromagnetic resonance frequency.

This equation does not have a general analytical solution, and must be calculated numerically. However, the solutions have the following properties. The angle of the magnetization θ varies with radial distance ρ and is independent of time. Hence, the spatial distribution of m_z is static and azimuthally symmetric. Localized solutions are found only for $0 < \omega < \omega_0$, which correspond to

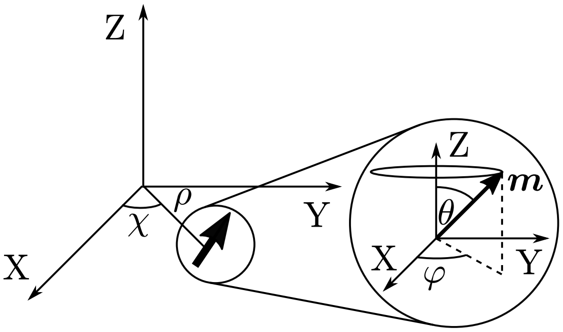

Figure 6.4: The angular variables of the magnetization $\vec{m}$ and the polar coordinates.

non-propagating spin waves. In the case $\nu = 0$, a *nontopological soliton* is created; the magnetization direction does not depend on the polar angle χ, and the value $\theta_0 \equiv \theta(\rho = 0) < \pi$. We will refer to this kind of nontopological solitons as *droplet solitons.* For topological solitons the values are $\nu \neq 0$, $\theta_0 = m\pi$, with $m = 0, \pm 1, \pm 2, \ldots$ an integer.

The topological charge (or invariant) $\mathcal{Q}$ of the magnetization vector $\vec{m}$ in two dimensions is defined as [Heinze et al. 2011]

$$\mathcal{Q} = \frac{1}{4\pi} \int \vec{m} \cdot \left(\frac{\partial \vec{m}}{\partial x} \times \frac{\partial \vec{m}}{\partial y} \right) \mathrm{d}x \, \mathrm{d}y \,. \tag{6.9}$$

If a certain distribution of $\vec{m}(x, y)$ can be brought by continuous deformation to the ground state, this will consist on the trivial mapping $\mathcal{Q} = 0$. If not, the distribution with $\mathcal{Q} \neq 0$ will be topologically stable, the so-called *skyrmions.*

In this thesis, only the nontopological $\mathcal{Q} = 0$—droplet soliton—case will be considered.

6.2.3 Dissipative Droplet Soliton

In the previous section we presented a set of solutions for uniaxial ferromagnets without damping consisting of droplet solitons. However, real materials have damping. Damping dissipates any excitation, which leads to a final quasi-static state. The STT term, however, can compensate the effects of the damping, leaving the possibility to form a soliton as in a damping-free ferromagnet. In this case, where damping and STT are balanced, in addition to the balance between exchange and anisotropy, a *dissipative droplet soliton* may form. Hoefer, Silva, et al. [2010] presented a theory describing this kind of solitons excited by STT in a thin ferromagnetic layer with perpendicular magnetic anisotropy (PMA). The theory

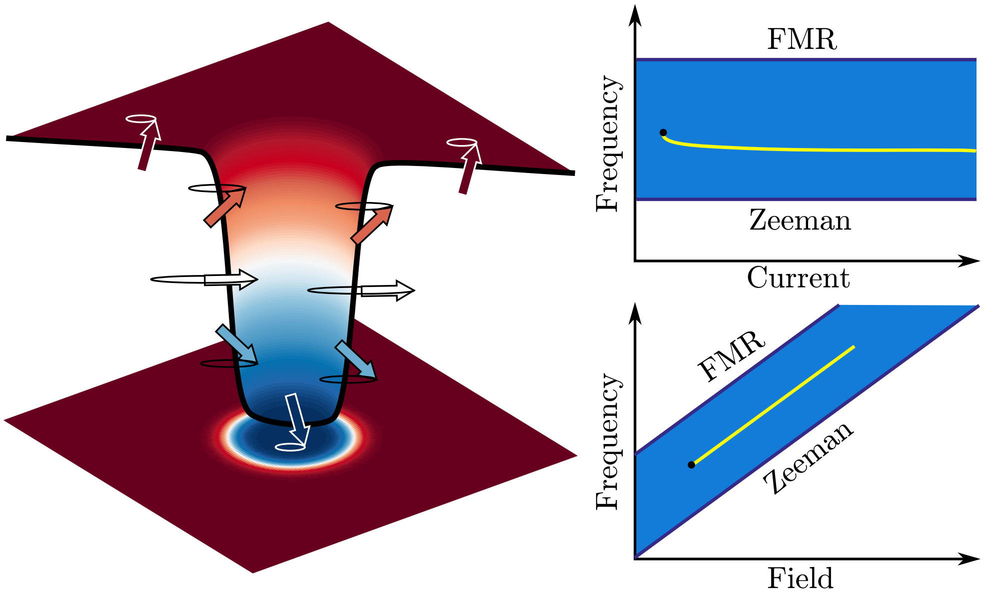

Figure 6.5: (Left-hand-side panel) Schematics of the Z component of the magnetization of a droplet. The spins rotate in the middle of the droplet. (Right-hand-side panels) The characteristic frequency of the droplet lays between f_{Zeeman} and f_{FMR}.

analyzes asymptotic solutions of the the LL equation with the Slonczewski STT term, Eq.(6.2).

An experimental approach to observe this kind of droplet solitons uses a fixed, polarizing magnetic layer with magnetization $\vec{M}_{\mathrm{p}}$ to polarize the current, a free layer with magnetization $\vec{M}$, and a nanocontact to flow electrons through the layers. The angle between the free and the polarizing layers determines the direction of the spin torque. In order to produce the instability that leads to droplet formation, a parallel component in the alignment of the fixed and free layers is required.

The current at which the damping is balanced by spin torque is called the *sustaining current*. When the sustaining current is reached, the droplet is created and the magnetization oscillates at a characteristic frequency above the Zeeman frequency—oscillation frequency characteristic of the external field, $f_{\mathrm{Zeeman}} = \gamma\mu_0 h_0$— and below the ferromagnetic frequency, $f_{\mathrm{Zeeman}} < f < f_{\mathrm{FMR}}$. As the current is further increased, the characteristic frequency of the droplet will decrease, see Fig. 6.5.

For increasing angles of the free layer, the component of the polarized electrons producing the instability with the spin torque is reduced, and hence a higher sustaining current is required. A magnetic field parallel to the free layer magnetization shifts the characteristic frequency. An increasing field costs Zeeman energy on the reversed magnetization of the droplet state, and it eventually causes the droplet to collapse. A perpendicular component of the applied field displaces the droplet from the nanocontact area and eventually annihilates it when the droplet is moved outside the region in which the damping is compensated by spin torque.

Magnetization switching by the effect of the STT was reported using dc measurements as evidence [Katine et al. 2000; Myers 1999]. The authors of those experiments used a trilayer of Co/Cu/Co. The Cu spacer layer was fabricated to reduce exchange interactions between the Co FM layers. Myers [1999] used a nanocontact scheme, whilst Katine et al. [2000] used a pillar stack. The relative orientation of the two layers was measured via the GMR effect. As the current is increased, a step in the measured resistance R—or a peak in the differential resistance $\mathrm{d}V/\mathrm{d}I$—is observed as the FL and PL magnetization orientation rotate and spin waves are generated at a threshold current. Because the STT is asymmetric with the applied current, this step—or peak—appears only for a current sign, see Fig. 6.3.

High-frequency dynamics in the presence of in-plane fields were directly measured in [Kiselev et al. 2003; Rippard et al. 2004]. Bonetti, Tiberkevich, et al. [2010] observed the appearance of an excitation at a frequency lower than the FMR that redshifted with increasing current, corresponding to a localized excitation.

S. Chung et al. [2014], Mohseni, Sani, Dumas, et al. [2014], and Mohseni, Sani, Persson, et al. [2013] used a nanocontact to a FL with PMA to produce localized excitations, and observed an step decrease in the precessional frequency as the field was increased. At the same time, MR had a step and a change of trend from negative to positive. This behavior is produced when the dissipative droplet soliton forms below the nanocontact. In these experiments, the magnetization of the PL is in plane, so an external out-of-plane magnetic field is needed to tilt the magnetization of the PL and produce a spin torque that drives the magnetization of the FL out of equilibrium. As a consequence, there is a threshold field above which the spin torque is sufficient to produce the droplet, and this is current dependent. Moreover, because the spin torque depends on the current direction, the droplet is only created when the torque acts against the damping, which is produced only for one polarity, corresponding to electrons going first through the free layer, see Fig. 6.6.

Macià, Backes, et al. [2014] measured the same kind of nanocontacts at low temperatures. In this case, a higher change in MR with respect to previous studies indicates an almost full reversal of the spins in the nanocontact. Also, a large hysteretical behavior is observed, confirming the high stability of the droplet once it is generated. From the analysis of the stability of the magnetization states in

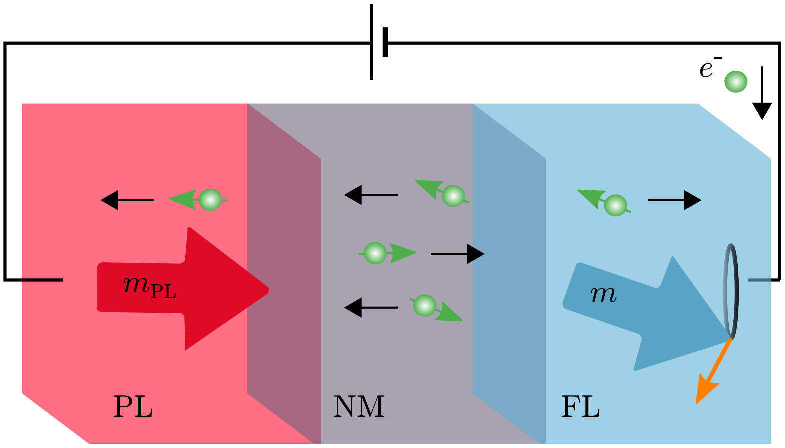

Figure 6.6: Direction of the spin torque (orange arrow) for an electron flowing from the FL (blue) to the PL (red), in the case the PL is completely tilted out of plane. The electrons (green) get spin polarized as they traverse the ferromagnetic layers. At the interface, the majority electrons are transmitted and minority electrons reflected. Conservation of angular momentum dictates the STT direction.

the parallel ($m_z = 1$) and antiparallel ($m_z = -1$) states, they derive an expression of the size of the hysteretic region, for a fixed current σ_0:

$$\Delta h_0 = \frac{\sigma_0}{\alpha}(\lambda^2 - 1) + 2h_{\mathrm{p}}. \tag{6.10}$$

From the same analysis, the size of the hysteresis for a fixed field h_0 is found to be

$$\Delta \sigma_0 = \frac{\alpha}{\lambda^2}\left[(1-\lambda)^2 h_0 - (1+\lambda^2)h_{\mathrm{p}}\right]. \tag{6.11}$$

In the case without an asymmetric torque, Eqs. (6.10) and (6.11) turn into

$$\Delta h_0 = 2h_{\mathrm{p}}, \tag{6.12}$$

$$\Delta \sigma_0 = -2\alpha h_{\mathrm{p}}. \tag{6.13}$$

6.3 Experiments at Room Temperature

6.3.1 Experimental Details

We fabricated samples consisting of FL with PMA and an in-plane PL, see Fig. 6.7. The FL is a 4-nm-thick multilayer of CoNi, and the PL layer a 10-nm-thick Py.

A Cu spacer layer was fabricated to avoid exchange interactions between the FL and the PL, hence magnetically decoupling the two layers. Silicon dioxide (SiO_2) was used as a dielectric, and Au for the contacts and pads. Circular contacts with diameters ranging from 80 nm to 150 nm were patterned through the dielectric by electron-beam lithography. In a previous study [Macià, Warnicke, et al. 2012], FMR was done, and the effective anisotropy field from the CoNi multilayer resulted in $\mu_0 H_\mathrm{p} = 0.25$ T.

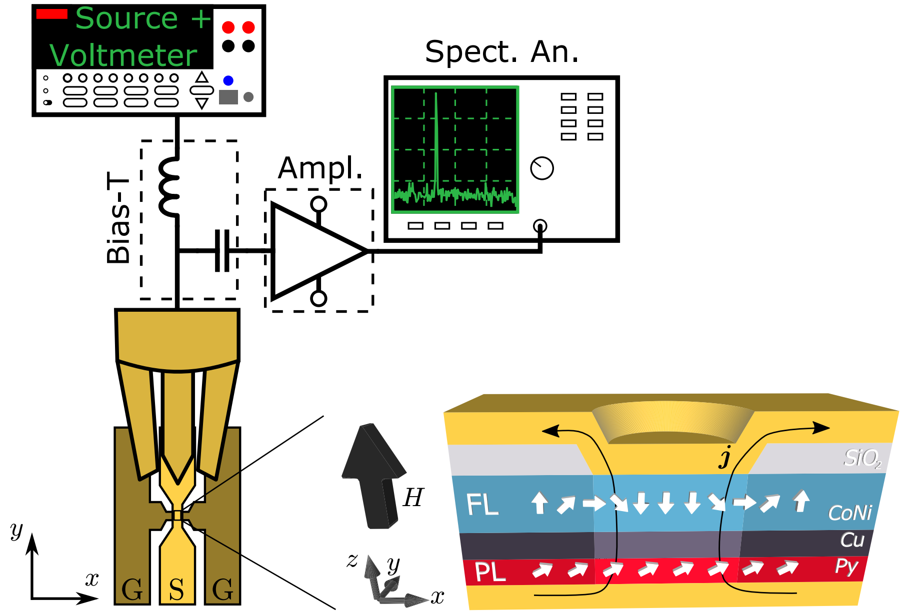

Figure 6.7: Schematic drawing of the experimental setup. In the left hand side panel, the pads with a 50 μm pitch are shown. A *Picoprobe*® is used to contact the sample. In the right hand side panel, the region with the nanocontact has been zoomed in and sliced to show the layer stack.

The resistance of the samples was measured by contacting a probe to the gold pads. The pads were patterned in a CPW shape, i.e with a source (S) stripe in between two ground (G) contacts, with a patch distance of 50 μm. Each nanocontact can be measured from two sides, allowing for 4 probe measurements, see Fig. 6.7. Due to the thick layer of dielectric, current flows between the gold pads only through the nanocontact diameter, because it is a low-resistance area in comparison with the dielectric area. The probes are *Picoprobes*® from GGB industries, and specially designed to be non-magnetic, and larger to decrease any interaction between the magnetic field and the connectors. The probes allow us to measure low- and high-frequency response of the samples. Low-frequency response (< 1 MHz) can also be measured with direct bonding of the samples.

We placed the sample between the poles of an electromagnet that allowed us to apply magnetic fields up to 1.5 T. The angle between the field and the film plane could be adjusted by rotating the sample holder. The sample was connected to a Keithley 2400 SourceMeter, that acts as a current source and voltmeter, and to a HP 8565E spectrum analyzer (SA), with working frequencies in the range 10 MHz – 50 GHz. A bias-tee was used to filter the dc and the ac signals coming from the sample. The current source and voltmeter was connected to the ac filtered end of the bias-tee, the sample to the end without any filtering, and the SA to the dc filtered end. Before entering the SA, and after the bias-tee, the signal is amplified by 20 dB with a high- or low-frequency low-noise amplifier, depending on the measurement. The low-frequency amplifier has nominal operational frequency range (0.1 – 1000) MHz, and the high-frequency amplifier 500 MHz – 30 GHz, see Fig. 6.7.

The GMR effect produces a measurable change in the electrical response as a current is applied. Hence, the measured resistance allows us to detect variations of the FL magnetization direction with respect to the in-plane PL in the nanocontact region. The resistance depends on the relative orientation of the magnetization of the FL $\vec{m}_{\mathrm{FL}}$, and PL $\vec{m}_{\mathrm{PL}}$

$$\bar{R} = R_0 \frac{1 - \vec{m}_{\mathrm{FL}} \cdot \vec{m}_{\mathrm{PL}}}{2}, \qquad \bar{R}_0 = \frac{R_{\mathrm{AP}} - R_{\mathrm{P}}}{R_{\mathrm{P}}}, \tag{6.14}$$

with $R_{\mathrm{AP,P}}$ being the resistance between the device antiparallel (AP) and parallel (P) magnetization states. We denote with $\bar{R}$ the resistance normalized by the P-state resistance R_{P}.

Figure 6.8 shows schematically the effect of an external field on the resistance of the point contact. When an out-of-plane—Z direction—field is applied (left-hand-side panel in the figure), the resistance decreases linearly with the applied magnetic field as the Py magnetic moments tilt out of the film plane, $\vec{m}_{\mathrm{PL}} \cdot \vec{e}_z = H/M_{\mathrm{S}}$ for $\mu_0 H < \mu_0 M_{\mathrm{S}}$ with $\mu_0 M_{\mathrm{S}} \approx 1$ T; the CoNi magnetization remains perpendicular to the film plane. Therefore, at large applied fields, $\mu_0 H > \mu_0 M_{\mathrm{S}}$, the magnetization of the two layers forms a P state. The measured overall change in resistance of the STNO ($\bar{R}_0 = 0.2$ %) corresponds to twice the difference between resistance at zero field and resistance when the magnetization of the PL and FL are orthogonal. The dashed curve in the left-hand-side panel of Fig. 6.8 illustrates the expected MR for a reversed FL magnetization—i.e. magnetization opposite to the applied field. This curve is obtained by reflecting the measured MR about the horizontal line, $R(H = 0)$. A positive slope is characteristic of an increasing angle between the FL and the PL.

When the field is applied in plane—X or Y direction—, the resistance again decreases linearly as the CoNi magnetic moments (the FL) tilt to the plane, $\vec{m}_{\mathrm{FL}} \cdot \vec{e}_z = H/M_{\mathrm{S}}(\mathrm{CoNi})$ for $\mu_0 H < \mu_0 M_{\mathrm{S}}(\mathrm{CoNi})$. The Py magnetization (the

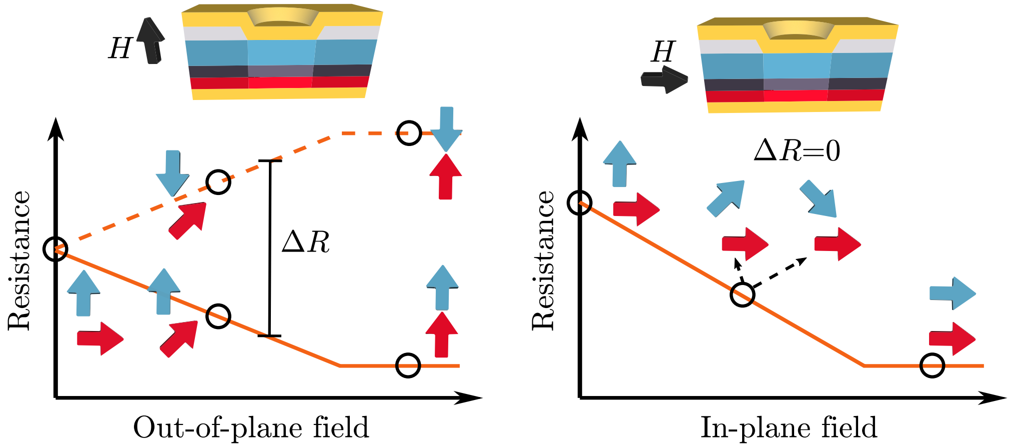

Figure 6.8: Magnetoresistance of the layer stack. In the left-hand-side panel, the field is applied out of plane, and in the right-hand-side panel the field is applied in plane. The difference in resistance when the FL magnetization reverses is noted.

PL) remains in the film plane. At large applied fields $\mu_0 H > \mu_0 M_\mathrm{S}(\mathrm{CoNi})$, the magnetization of the two layers are in a P state, and the resistance is minimum. Note that in this case, a reversal in the FL magnetization does not produce a change in the measured resistance, because the product $\vec{m}_\mathrm{FL} \cdot \vec{m}_\mathrm{PL} = \cos\phi$ in Eq. (6.14) remains constant, i.e. the angle between the FL and PL, ϕ, does not change despite the reversal.

We measured step changes in the dc resistance that we attributed to the onset of droplet soliton excitations, when the magnetization of the FL reverses as the PL remains fixed. This onset is produced at a threshold current, when the field is fixed, or at a threshold field, when the current is fixed. In addition to this dc response, we measured variation on the voltage response with the SA (coming from a change in resistance), due to the change in the angle between the FL and the PL when the FL oscillates around equilibrium. The SA filters the signal and gives the spectral response. As a consequence, a peak appears at the frequency of the signal, if any, and its height is related to the amplitude of the oscillation, in our case the change in the angle between FL and PL $\Delta\phi$. This voltage signal is produced at fields lower than the saturation field of the PL, and vanishes as the field increases and the magnetization direction of the two layers align, as there is no change in ϕ during the oscillation, see Fig. 6.9. The oscillation of the magnetization around its equilibrium position is typically on the GHz range.

Further, by changing the working amplifier, we were able to measure a variation of the resistance at a lower frequency (in the MHz range), which we associated to movement of the soliton structure beneath the nanocontact at a characteristic

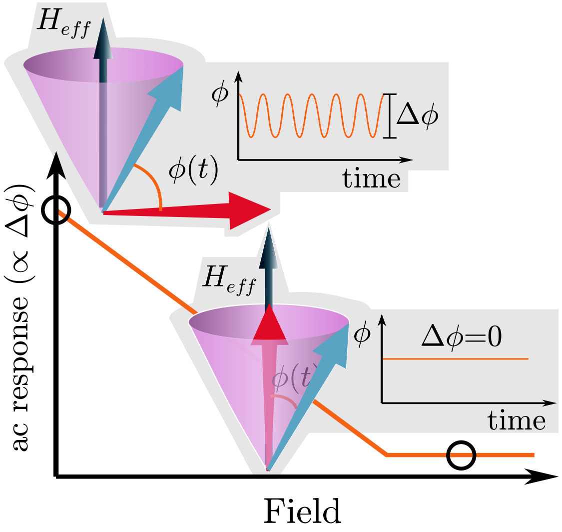

Figure 6.9: Schematics of the ac response measured with the SA, as a function of the out-of-plane field. As the field is increased, the ac response due to the oscillation of the FL around the equilibrium vanishes.

frequency; contrary to the previous case, this signal does not vanish when the PL is saturated. Movement of the droplet beneath the nanocontact produces a change in the measured dc resistance, even if the droplet still exists, because the only measurable quantity in a dc technique is the average resistance beneath the nanocontact area, where the current flows and its polarization affected by the FL and PL, as shown in Fig. 6.10.

6.3.2 Results

We measured the dc response of resistance for the two current directions. Only a current direction produced the onset and annihilation of the droplet soliton, which we assign to positive currents, and corresponding to electrons getting polarized by the PL as shown in Fig. 6.6. Samples are first measured fixing an out-of-plane field and sweeping the current. An abrupt change in resistance appears as the droplet creates or annihilates. When the current is swept up, a step increase in resistance is measured; when the current is swept down, the resistance decreases.

These measurements are shown in Fig. 6.11, where the resistance as a function of the currents for different fields is plotted. Each set of measurements is done at a fixed field, and the current is swept from 0 mA to 35 mA, and back to 0 mA; during the current sweep, resistance is measured. The onset of the droplet is detected at fields $\mu_0 H > 0.4$ T. The position of the onset varies as the field is changed. For fields 0.5 T $< \mu_0 H <$ 0.9 T (red, blue and green curves in Fig. 6.11)

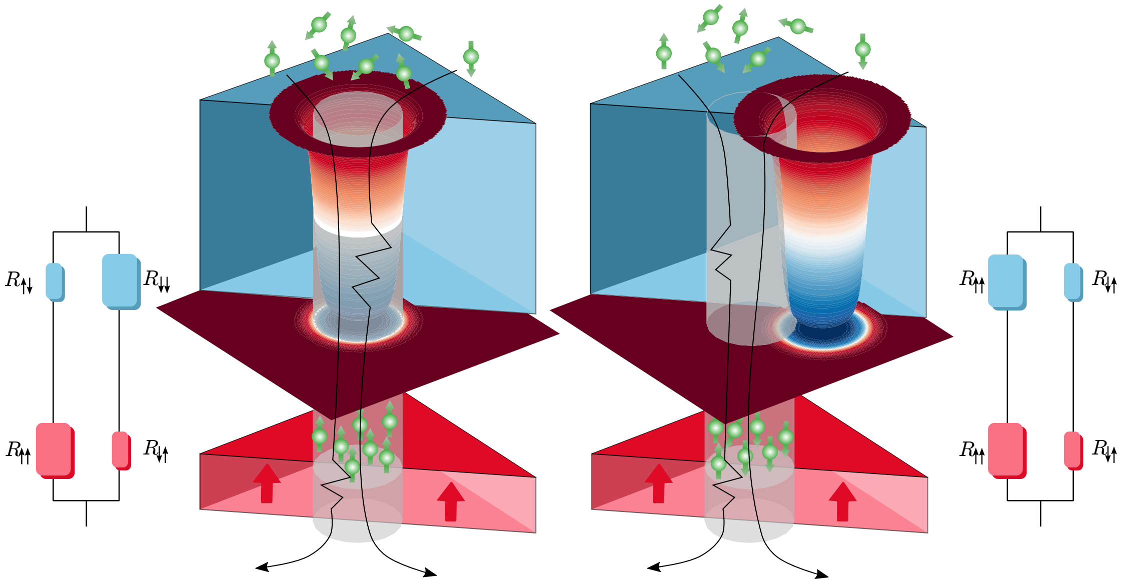

Figure 6.10: Resistance variation as the droplet moves out of the nanocontact region. The electrons flowing only inside the nanocontact have different scattering depending on the orientation of the magnetization in the nanocontact.

the PL is not saturated; the PL tilts as the field is increased. In this regime, the onset current decreases for increasing fields for $\mu_0 H < 0.6$ T, and increases for increasing fields for $\mu_0 H > 0.6$ T. Moreoever, at larger field values $\mu_0 H > 0.9\,\mathrm{T}$, when the PL saturates, hysteresis is observed: the onset current corresponding to droplet creation is higher than the current at which the droplet is annihilated during the down sweep (purple and orange curves). Figure 6.12 shows a state map representing the creation and annihilation currents for all the measured fields. In the area to the right of the creation current (orange in the figure), the system is always in a droplet state, while in the area to the left of the annihilation (purple in the figure) the current and field combinations do not produce enough STT to create the droplet. For fields $\mu_0 H > 0.9\,\mathrm{T}$, a hysteretic region appears (green area in the figure), where the droplet exists only if coming from the droplet state.

Macià, Backes, et al. [2014] reported on hysteresis measurements at low temperature. Room temperature measurements, however, showed much smaller hysteretic effects [Mohseni, Sani, Persson, et al. 2013]. We will further study temperature dependance of the droplet in Section 6.4. Measurements of several devices show similar onset maps for the droplet excitation, but the hysteretic response differs considerably: on all samples, hysteresis appears at large fields, $\mu_0 H > 0.9$ T, but the size of the hysteresis ranges between 0.5 mA and 5 mA.

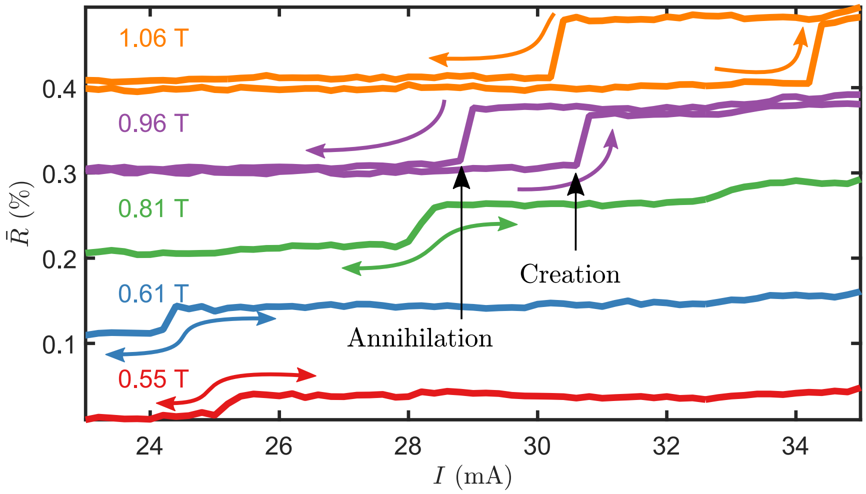

Figure 6.11: Measured MR as a function of applied current for fields ranging from 0.5 T to 1.1 T.

As illustrated in Fig. 6.8, the overall change in resistance ΔR—accounting for the difference in resistance when the droplet is created—is field dependent because the angle of the PL increases with field. MR changes during droplet creation are measured to be up to $\Delta\bar{R} \approx 0.08\,\%$, produced at fields above the saturation of the PL magnetization ($\sim$ 1 T). This changes corresponds to only a fraction ($\approx 1/3$) of the maximum total change of resistance, $\bar{R}_0 = 0.2$ %, corresponding to the AP configuration of the magnetizations of the FL and PL. From this, it follows that the spins in the droplet state are not fully reversed during the measuring time. One possible explanation is that the magnetization of the FL precesses at a lower effective angle of ≈ 70 degrees; another explanation is that the droplet excitation is smaller than the nanocontact, or that it moves, resulting in a lower effective resistance. This movement can come from drift instabilities [Hoefer, Silva, et al. 2010; Hoefer, Sommacal, et al. 2012].

In addition to the dc measurements reported so far, we have measured the high-frequency response of the resistance. Figure 6.13 shows high-frequency spectra at a field of $\mu_0 H = 710$ mT. When the droplet is generated, the frequency of the excitation is measured to be $f \approx 20.3$ GHz, below the FMR frequency at the same field ($f_{\text{FMR}} = 27.5$ GHz), and above the so-called Zeeman frequency ($f_{\text{Zeeman}} = \gamma\mu_0 H = 19.9$ GHz) as corresponds to a droplet excitation [Hoefer, Silva, et al. 2010]. The frequency increases (blueshifts) with the current, with jumps (below 0.3 GHz) to lower frequencies at certain current values. The peak widths of

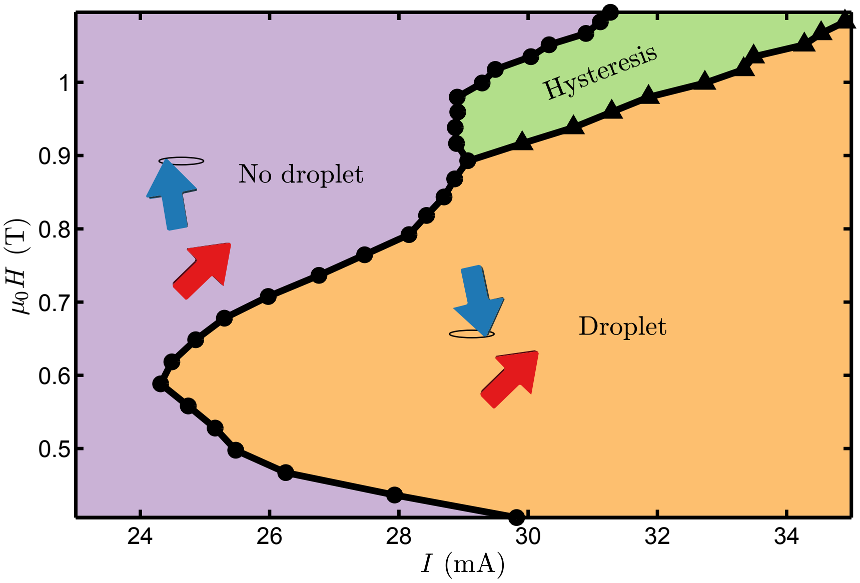

Figure 6.12: Stability map of the droplet soliton: red triangles show creation of the droplet, and blue dots annihilation.

the droplet excitations are about 10 MHz, with quality factors of $Q \approx 2000$, see the inset of Fig. 6.13 where the power spectra at a fixed applied current of $I = 30$ mA is plotted. As the field increases, so does the excitation frequency, with values always below the corresponding FMR frequency (5–8 GHz below FMR). When the field is further increased, the microwave signal vanishes because the magnetization of the PL saturates perpendicular to the film, in the same direction as the FL, giving no effective change in the ac response when it oscillates, see Fig. 6.9.

As deduced from the dc measurements of the resistance, the magnetization in the droplet state is only partially reversed. One possible explanation is that the droplet as a whole moves beneath the nanocontact, reducing the effective measured resistance. This movement would be similar to the movement of domain walls, with characteristic frequencies on the order of 100 MHz [Chikazumi et al. 1997]. To elucidate if this is the case, we measured the variations in resistance at lower frequencies, on the order of hundreds of MHz. In this case, as the droplet is generated, a broad oscillating signal at about 300 MHz appears, having a weak dependance on the applied field and current, see Fig. 6.14. This broad, low-frequency signal appears at the same current as the step in dc resistance—explained above—, and hence we associate it to the droplet excitation. The shape of the low-frequency signal differs from sample to sample, in some cases having well-defined peaks and broader structures in others, but the dynamics are always present in

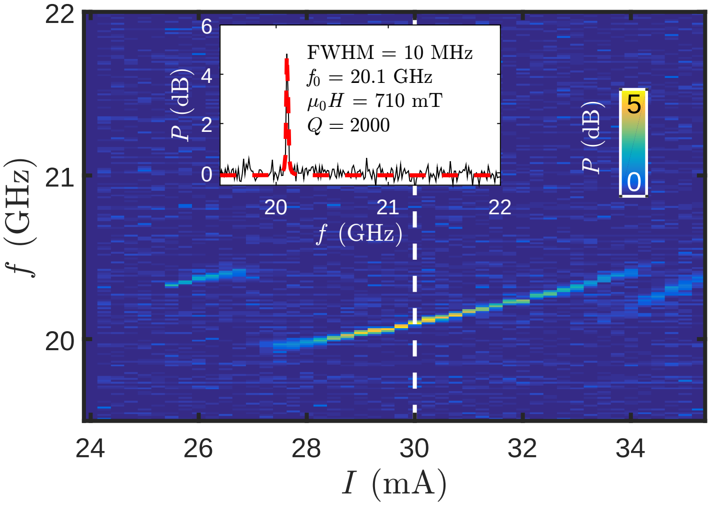

Figure 6.13: High-frequency spectra as a function of applied current for a field of 710 mT. The inset shows the signal, in dB above noise, at a fixed current of $I = 30$ mA, following the white dashed line in the main figure. The fitted data (red dashed line) shows a narrow peak with a FWHM ≈ 10 MHz, and a quality factor $Q \approx 2000$.

the range of 100 MHz – 800 MHz. The hysteresis observed in the dc signal is also observed in the presence of the low-frequency dynamics.

At fields below the saturation of the PL, different excitation modes appear as the current increases (see Fig. 6.14(a)–(c)), and, opposed to the high-frequency mode, the signal remains strong at fields above the saturation, see Fig. 6.14(d)–(f). This proves that the origin of the low-frequency dynamics does not come from the precession of the FL magnetization around the equilibrium, but to the droplet object as a whole.

Next, we measure the dependence of the droplet excitation with the angle of the applied field. We first fixed the applied field strength and, at each angle, we measured the low-frequency spectra and the dc resistance. Droplet excitations are present only when the applied field is perpendicular to the film and we found that the maximum angle we can tilt the field before the excitation annihilates is about 15°. As we tilt the angle the low-frequency spectra becomes stronger. Figure 6.15 shows both the dc resistance and the low frequency spectra of the nanocontact as a function of the applied field angle. We see that the low-frequency spectra is larger at angles between 5° and 15°. Further, we observe in the measurements shown in Fig. 6.15 that the tilt in one direction produces a stronger low-frequency signal. We also notice that for the stronger low-frequency signal, at positive angles

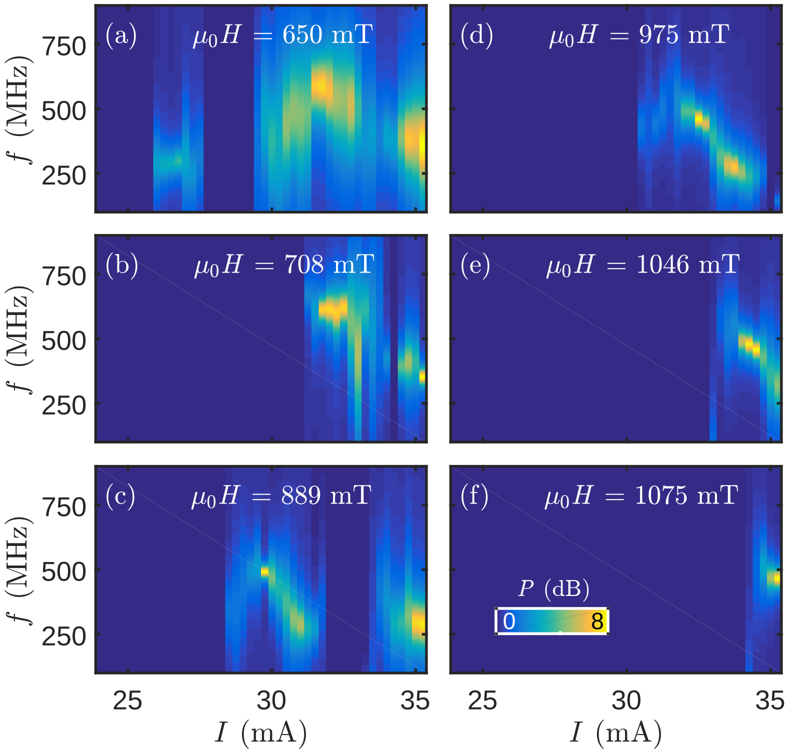

Figure 6.14: Low-frequency spectra as a function of applied current for fields of 650 mT (a), 708 mT (b), 889 mT (c), 975 mT (d), 1046 mT (e), and 1075 mT (f).

between 5° and 15° the dc resistance signal also decreases, being consistent with the fact that the low-frequency dynamics lowers the averaged resistance value.

6.3.3 Micromagnetic Simulations

We modeled the nanocontact and the droplet excitations with micromagnetic simulations using the open-source MuMax code [Vansteenkiste et al. 2014], and performed parallel calculations with a graphics card with 2048 processing cores.

We fixed the material parameters to the values we measured experimentally with FMR ($M_S = 500 \cdot 10^3$ A/m, $K = 200 \cdot 10^3$ J/m^3, $A = 10 \cdot 10^{-12}$ J/m) in a circular nanocontact of 150 nm in diameter. We used a damping parameter $\alpha = 0.03$ and adjusted the STT efficiency to obtain a droplet onset map similar to the measured in Fig. 6.12. We also considered the effects of the Oersted fields.

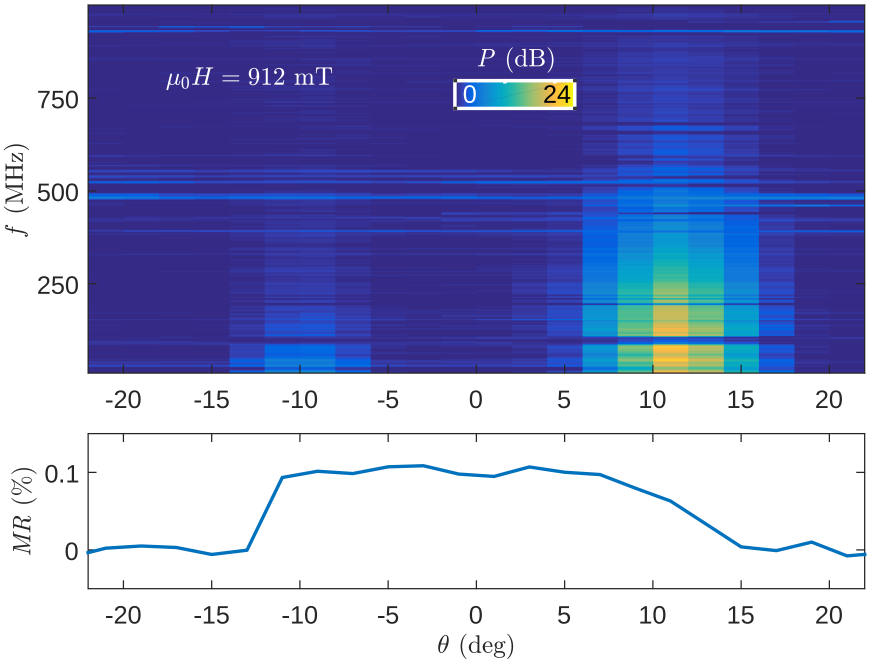

Figure 6.15: (Top panel) Low-frequency spectra as a function of the angle of the applied field for a field of 912 mT. (Bottom panel) MR as a function of the angle of the applied field for the same sample. The two measurements were taken at the same time for an applied current of 40 mA.

Simulations show the difference in current values of the onset and annihilation of the droplet soliton. As in the experimental results, this hysteresis happens due to the stability of the droplet, with a value larger than twice the anisotropy field, $2\,\mu_0 H_\mathrm{p} = 0.5$ T [Macià, Backes, et al. 2014]. As showed in Fig. 6.12, the measured hysteresis in our samples, however, has smaller values of ≈ 0.1 T. With these simulation parameters, there is no presence of drift instabilities, characteristic for the low-frequency dynamics, see the first upper panels of Fig. 6.16.

Slow motion of the droplet appears by applying a small in-plane field ($\mu_0 H \approx 0.15$ T), in addition to an out-of-plane field of 1.1 mT, see Fig. 6.16. This field is equivalent to a field forming an angle $\theta \approx 8$ degrees with the sample. The upper panels of the figure show the out-of plane m_z and in-plane m_x magnetization around the nanocontact area. In this simulation, all the magnetization is initially pointing in the same direction, $m_z = 1$. At $t = 0$ ns the out-of-plane magnetic field of 1.1 mT is applied and the droplet is formed during the first 5 ns, characterized by a reversal on the magnetization $m_z = -1$. At this point ($t = 5$ ns), an small in-plane field of 0.15 T is applied. The droplet initially shifts in the direction

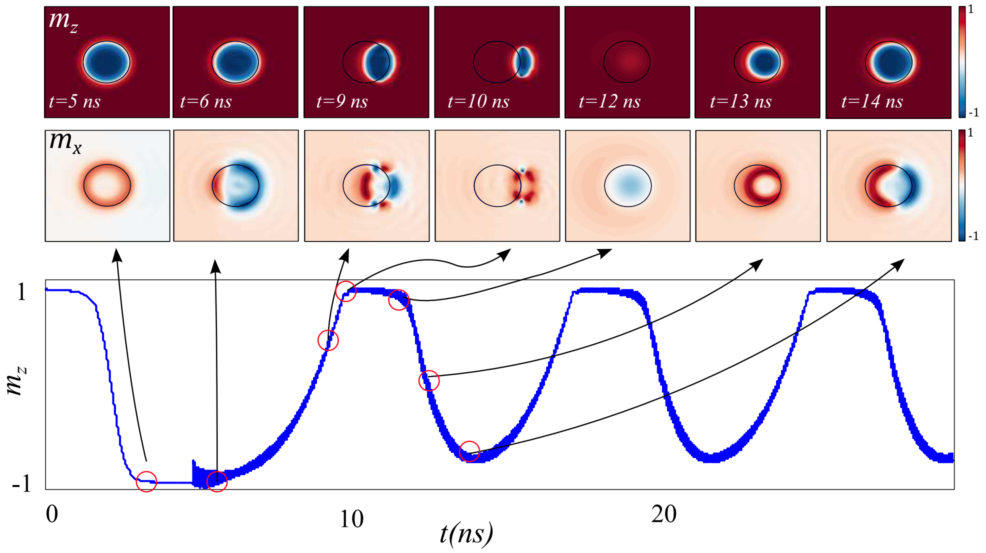

Figure 6.16: Time evolution of the droplet soliton upon an applied field of 1.1 T perpendicular to the film plane first and then with an additional in-plane field (Y direction) of 0.15 T. The upper panels show magnetization maps for m_z, and m_x, at particular times of the simulation. Images correspond to a 400 × 400 nm^2 field view. The contact region is outlined in black. The lower panel shows the time evolution of the perpendicular component of the magnetization, m_z, in the nanocontact area.

perpendicular to the applied in-plane field (6 ns to 10 ns) and dies out as it moves away of the nanocontact region because of the damping ($t = 12$ ns). At the same time, a new droplet soliton appears beneath the nanocontact region (12 ns to 14 ns). The whole process has a frequency of about 150 MHz for the simulated parameters (seen in the evolution of the m_z magnetization in the lower panel), and is nearly independent of the out-of-plane field and applied current. We notice that the time average of m_z beneath the nanocontact—that is the measurable quantity using any dc technique—is only a 36 % of the total, or equivalent to a precessing angle of 73 degrees [Backes et al. 2015].

So far, simulations show a drift instability when an in-plane field is applied. However, our experiments showed low-frequency dynamics even at a 0 degree angle. We introduced asymmetric parameters in the simulations and found that a variation in the anisotropy K of only 3 % between the halves of the nanocontact produces a drift instability with almost the same annihilation and creation frequency, see Fig. 6.17. In this simulation, the right half of the nanocontact has an anisotropy constant $K_1 = 200 \cdot 10^3$ J/m^3, and the left half $K_2 = 206 \cdot 10^3$ J/m^3. The droplet moves away from the nanocontact during the first 16 ns and dies out.

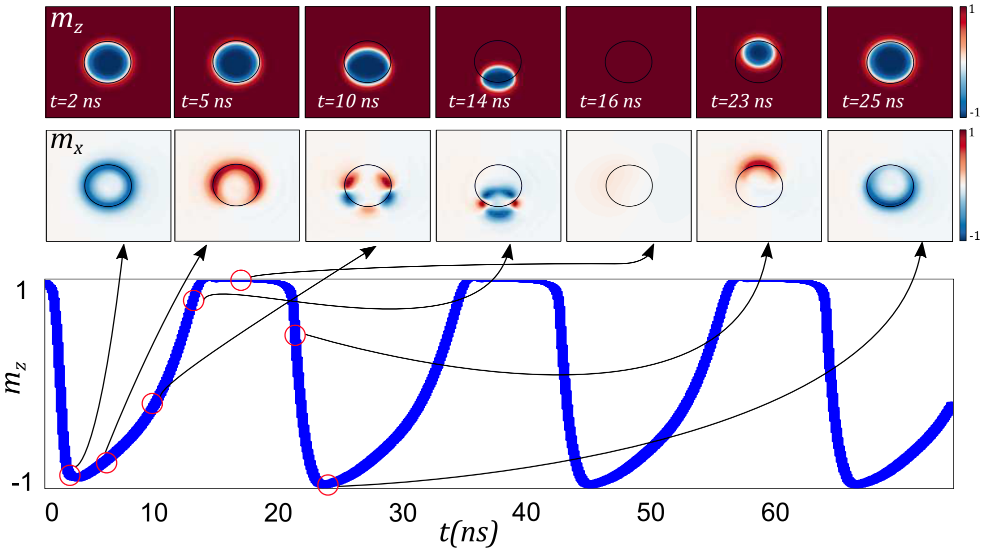

Figure 6.17: Time evolution of the droplet soliton upon an applied field of 1.1 T perpendicular to the film plane and with an anistropy that varies 3 % in the two halves of the nanocontact. The upper panels show magnetization maps for m_z, and m_x, at particular times of the simulation. Images correspond to a 400 × 400 nm^2 field view. The contact region is outlined in blue. The lower panel shows the time evolution of the perpendicular component of the magnetization, m_z, in the nanocontact area.

From $t = 20$ ns to $t = 25$ ns a new droplet is created beneath the nanocontact, and the cycle is repeated with a frequency similar to the case of an in-plane field.

Furthermore, we found that any asymmetry in the effective field causes the drift instability, resulting in annihilation and creation of the droplet soliton oscillating at a frequency on the order of hundreds of MHz.

It is also worth noting that, even when the droplet is moved by drift instabilities and is continuously created and annihilated, there is hysteresis in the creation and annihilation characteristic values. This is produced by the precession of the magnetization beneath the nanocontact, being larger in the case a droplet exists in the system—even if it has moved away from the nanocontact—than in the absence of any excitation. The size of the hysteresis, however, is affected by the drift instability, and reduces from ∼ 0.6 T to ∼ 0.1 T in our simulations.

6.3.4 Discussion

Drift instabilities were described as a consequence of magnetostatic interactions between the effective dipole moment of the droplet and an effective field gradient, associated with the Oersted field [Hoefer, Silva, et al. 2010] or with differences in the anisotropy. A small in-plane field or a small gradient in the effective field creates an asymmetric landscape that dephases the precession of magnetization between edges in the soliton boundaries resulting in a magnetic force that acts on the soliton and shifts the overall soliton. Some experiments have shown the presence of side bands in the high-frequency precession magnetization in droplet soliton excitations [Mohseni, Sani, Persson, et al. 2013] suggesting that the soliton might be undergoing drift instabilities and micromagnetic studies have also predicted the side bands and attributed them to drift instabilities [Mohseni, Sani, Persson, et al. 2013; Puliafito et al. 2014]. However, those measurements cannot be disentangled from the spin precession and thus were not directly attributed to drift of the soliton.

Our direct observation of the low-frequency dynamics proves the existence of drift instabilities and explains why dc measurements fail to measure magnetization reversal on droplet solitons—showing just a fraction of the magnetization reversed. Additionally, our simulations took time frames of hundreds of nanoseconds in order to resolve the slow motion of the solitons.

We notice that the measured high-frequency dynamics, associated with the spin precession, increases slowly with the applied current, different to predictions and micromagnetic results. We cannot explain it with our model and we attribute such effect to the appearance of an effective field perpendicular to the film plane due to the applied current (likely an Oersted field effect from the leads). The overall change is always smaller than 500 MHz that would correspond to a magnetic field of 20 mT.

6.4 Experiments at Low Temperatures

As was reported in [Macià, Backes, et al. 2014], low-temperature measurements of dissipative magnetic droplet soliton showed changes in the MR signal corresponding to an almost full reversal of the magnetization [Mohseni, Sani, Persson, et al. 2013]. Further, low-temperature measurements indicate a high stability of droplet solitons with a much larger hysteresis compared with the measured at room temperature. In particular, experiments at room temperature [S. Chung et al. 2014; Mohseni, Sani, Dumas, et al. 2014; Mohseni, Sani, Persson, et al. 2013] have shown a step in resistance that corresponded to small precession angles and small or none hysteresis. Studies reported in the previous section give an explanation on why the measured MR is lower than a full reversal, i.e. the drift instabilities continuously move the droplet out of the contact and, as it is destroyed by the damping, a new droplet generates beneath the nanocontact, where the damping is suppressed by STT; this results in an effective reduction in the total MR. However, how this mechanism depends on temperature, and how temperature affects the creation of the droplet, has not been studied before.

In this section we report temperature dependent measurements of dissipative droplet solitons. The studies were done measuring the dc response of the MR signal to magnetic field and applied current, at different temperatures. We observe a decrease in hysteresis as the temperature increases, as well as a variation of the creation and annihilation currents and fields. We measure differences in the annihilation and creation processes. In the case of annihilation, the characteristic currents and fields have a broader distribution. Further, a random telegraph noise is observed and characterized, which indicates switching between levels, as has been previously observed in STNOs [Locatelli, Mizrahi, et al. 2014; Tsoi et al. 1998; Urazhdin et al. 2003].

6.4.1 Experimental Details

The same samples used in section 6.3 were wire-bonded onto a chip and introduced into a PPMS® cryostat that allowed us to sweep temperature in the range 2 K – 350 K and apply fields of up to 9 T. The angle between the film plane and the field can be varied by rotating the sample holder. We used a current source and a voltmeter combination to measure dc-resistance response. The measurements of the resistance allow us to determine the relative orientation of the magnetization in the free and polarizing layers via the GMR, see Fig. 6.8.

Unless otherwise noted, experimental results showed in the following are done with a field perpendicular to the film plane ($\theta = 0$).

6.4.2 Results

Results with Fixed Current

We first study the creation and annihilation of the droplet through dc measurements of the magnetoresistance. The current was fixed and the external field swept from -3 T to 3 T and back. As explained above and showed in Fig. 6.8, when the droplet is created, the nanocontact resistance increases (with a step), as the FL magnetization reverses and the nanocontact is in an AP state. On the contrary, when the droplet is annihilated, the resistance has a step decrease, as the FL and PL magnetizations align, forming the P state.

As the field is swept up from 0, the droplet is nucleated at small field values, when the STT is large enough to change the FL magnetization direction, Fig. 6.18. When the field is further increased, the STT is no longer able to overcome the high Zeeman energy of the external field and the droplet annihilates. Sweeping the field down, the droplet is created at lower fields than the annihilation of the sweep up, showing a hysteresis, and it annihilates when the field decreases further, as the STT is too small to maintain the droplet. The annihilation at low fields can also have hysteresis [Macià, Backes, et al. 2014], although we have not observed it in any of our measurements. For the sake of clarity, analysis is reduced to the annihilation of the droplet when sweeping the field up, and creation when sweeping it down, i.e. in the high-field range, and we will refer to the value of these fields as annihilation and creation fields, respectively. In the following we report only the case of one polarity of the applied field, as the results with the other polarity are analogous.

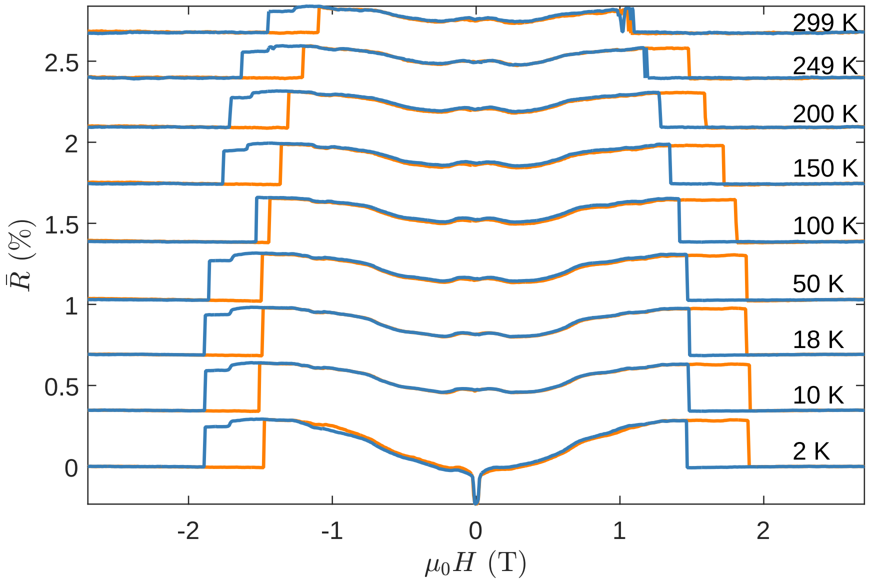

Figure 6.18: MR measurements as the field is swept up from -3 T to 3 T (orange) and down from 3 T to -3 T (blue), for different temperatures in the range 2 K – 300 K, at $I = 31$ mA, showing the creation and annihilation fields as the droplet is formed.

In order to evaluate the change in the characteristic resistance as the temperature is varied one has to take into account the intrinsic change in MR as the temperature changes, typically caused by, but not only, spin-wave excitation of the magnetization, which follows a $T^{3/2}$ law—Bloch law [Ashcroft et al. 1976; Chikazumi et al. 1997; Chudnovsky and Tejada 2006; Kittel 2004]. In order to take this into account, we measured the MR at a current value of -2 mA. The sign of the current was chosen to avoid excitations in the FL, i.e. it favors damping and stabilizes the FL magnetization. Moreover, a small value of 2 mA minimizes the STT, yet allowing for a measurement of the resistance. The top right-hand-side panel of Fig. 6.19 shows the measured MR at different temperatures. Note that for the lower temperature of 2 K, there is a change in resistance at low field values which cannot be explained in the picture of the FL being perpendicular to the PL. We attribute this to pinning of the magnetization arising at low temperatures. The step at small negative values visible for $T \geq 10$ K is due to the reversal of the FL in the direction of the external field, corresponding to the anisotropy field. A line is fitted to the descending part of the MR up to saturation—thicker line in the figure—, and the value at $\mu_0 H = 0$ T is then found from the fit. $\bar{R}_0$ is then computed as twice this value, and corresponds to a complete reversal of the FL. The bottom right-hand-side panel of Fig. 6.19 shows the dependance of $\bar{R}_0$ with temperature.

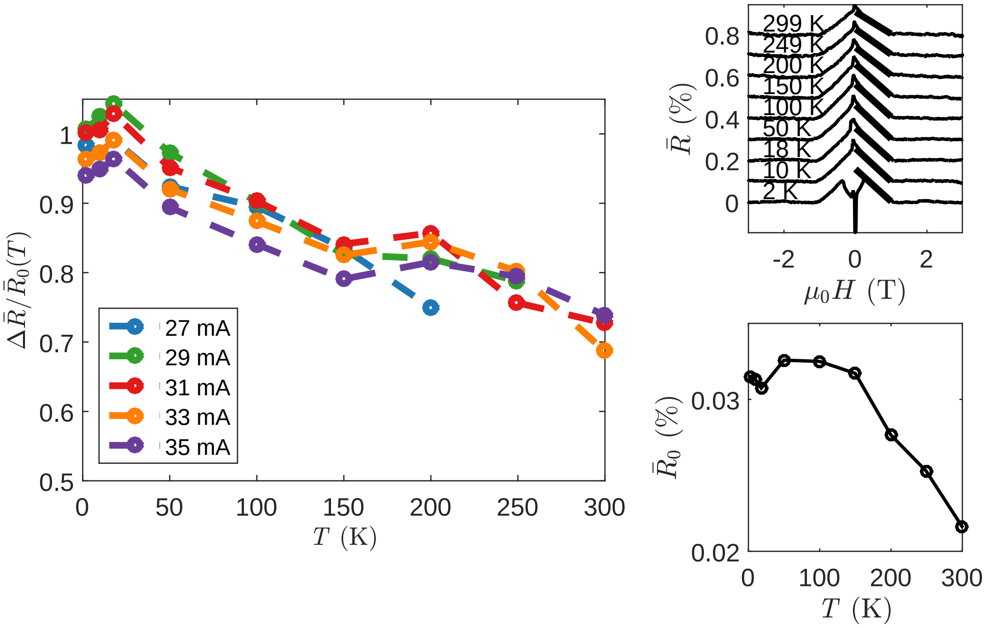

Figure 6.19: (Left-hand-side panel) Normalized height of the jump $\Delta\bar{R}/\bar{R}_0(T)$ as a function of temperature for current values of 27 mA (blue), 29 mA (green), 31 mA (red), 33 mA (orange), and 35mA (purple). (Top right-hand-side panel) MR measurements as the field is swept, for different temperatures in the range $(2 - 300)$ K, at $I = -2$ mA, where the droplet is not created. The thicker lines are fitted to find the overall change $\bar{R}_0$. (Bottom right-hand-side panel) Evolution of the overall change in magnetoresistance with temperature $\bar{R}_0(T)$.

The variations in resistance coming from the change in the droplet state are normalized by the intrinsic change $\bar{R}_0(T)$ at that particular field value in order to remove any temperature dependence of the MR. The left-hand-side panel of Fig. 6.19 shows the temperature dependence of the normalized variation in resistance. A value of 1 means that the FL and PL magnetizations are antiparallel. We can see that, as temperature increases, the reversal decreases from almost full reversal at low temperatures, to around 0.7 (corresponding to an effective precession angle of ≈ 130 degrees).

Next, we analyze the dependence on temperature of the creation and annihilation fields. Figure 6.20 shows the creation field $\mu_0 H_\mathrm{c}$ (left-hand-side panel) and the annihilation field $\mu_0 H_\mathrm{an}$ (right-hand-side panel) as the temperature is increased. Both fields present a decreasing trend with temperature indicating that the excitation becomes less stable as we increase the temperature. We notice that the annihilation field oscillates in some cases whereas the creation field is much more steady with temperature. The difference between creation and annihilation fields gives the hysteresis. In the case of lower currents 27 mA, and 29 mA, the two characteristic fields are the same, i.e. there is no hysteresis. A general trend to reduce and eventually suppress hysteresis with increasing temperature is observed for all current values. However, the hysteresis oscillates between high and low values at intermediate temperatures in some cases, as shown in the current values of 31 mA and 35 mA. This corresponds to the oscillation on the annihilation current. We observed that the value of current annihilation may take a broad distribution of values, while the onset current remains stable across measurements. Further measurements to increase statistics and determine the exact probability distribution would be needed.

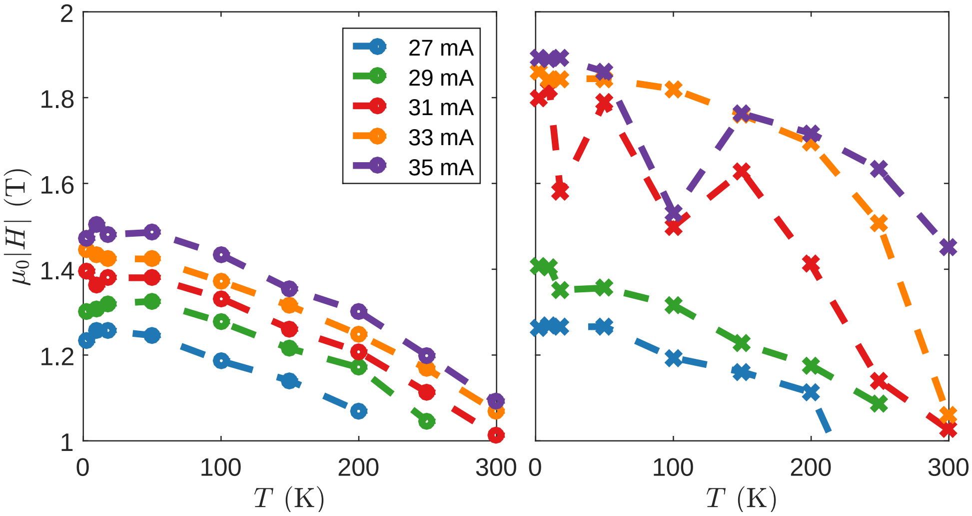

Figure 6.20: Value of the creation (left-hand-side panel) and annihilation (right-hand-side panel) fields as a function of temperature for currents values of 27 mA (blue), 29 mA (green), 31 mA (red), 33 mA (orange), and 35 mA (purple).

Results with Fixed Field

Let us now compare these results with the resistance measurements obtained fixing the field and sweeping the current. The current sweeps were repeated for increasing temperatures from 2 K to 350 K, as showed in Fig 6.21 for a field of $\mu_0 H = -1.25$ T. For this field value (and the electrical currents we applied), the droplet is created only below 200 K, and we can observe how the the creation and annihilation values of droplet solitons varies with temperature, as well as the height of the jump.

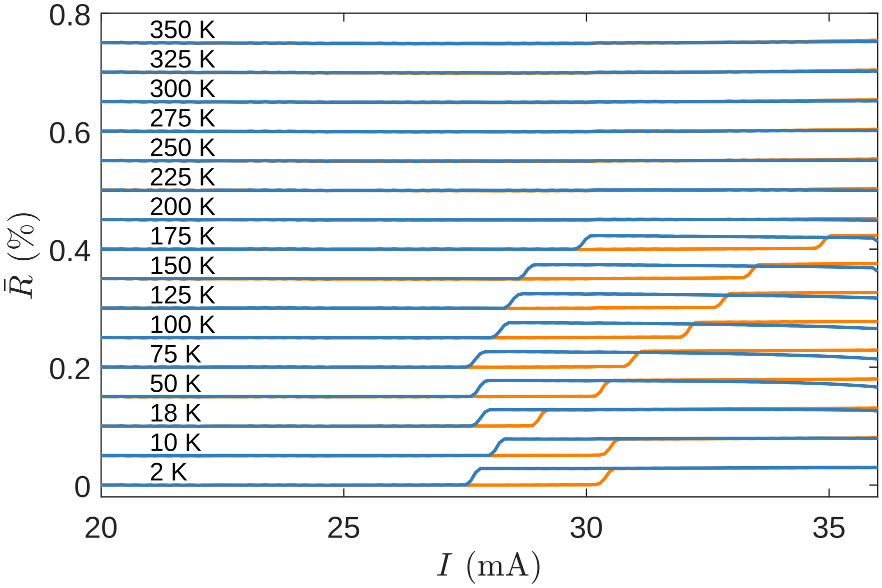

Figure 6.21: Resistance measurements as the current is cycled, for different temperatures, at a field $\mu_0 H = -1.25$ T, showing the droplet creation as the current is increased (orange curve) and annihilation when it is decreased (blue curve).

At low temperatures, the step in resistance is higher, similar to what we have observed in measurements where the current was fixed and we swept the field. This change, however, must be normalized by the characteristic change in MR due to temperature effects, as described previously, and the data should be normalized by $\bar{R}_0(T)$ showed in Fig. 6.19. Nevertheless, values corresponding to the temperatures measured in this case have been interpolated and, in the case of 350 K, an extrapolation is needed. Temperature dependance of the normalized variation obtained this way is showed in Fig. 6.22. For high fields $\mu_0 H \gtrsim 0.9$ T, the dependance on the normalized change is similar to the one showed in Fig 6.19, with a decrease with temperature to values close to 0.7 at 300 K. On the other hand, for lower fields, an opposite trend is observed, where the variation increases with temperature from a low value to, again, around 0.7 at 300 K.

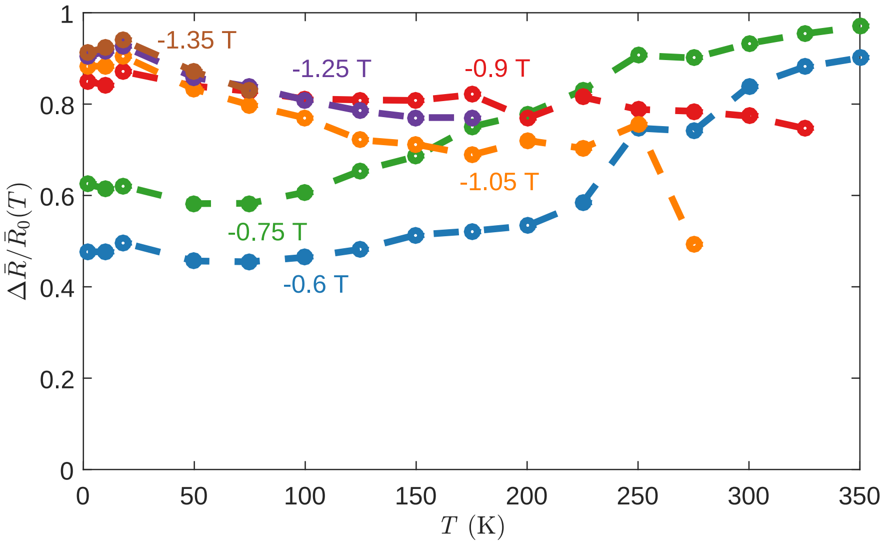

Figure 6.22: Variation in the normalized resistance as a function of temperature, for field values of −0.6 T (blue), −0.75 T (green), −0.9 T (red), −1.05 T (orange), −1.25 T (purple), and −1.35 T (brown).

Figure 6.23 shows the evolution of the onset (dark) and annihilation (light) currents with temperature, for some fixed fields. Note that for higher fields, the creation and annihilation currents increase and differ more, indicating an increasing hysteresis with field. Also, curves at high fields are only visible for low temperatures, as the droplet is not produced for these currents when the temperature is increased, as can be seen in Fig. 6.21.

6.4.3 Discussion

In order to further discern the temperature stability of the excitations in the nanocontact, we plot a stability map in Fig 6.24. In this map the information of both field and current is plotted at the same time, similar to Fig. 6.12 from section 6.3. In this case, however, we have measured various temperatures, indicated with colors from dark blue, corresponding to 2 K, to dark red, corresponding to 350 K. In the region to the right of each line, the system is in the droplet state, while in the region to the left, the droplet is not created. We have only plotted the creation time because, as we have previously discussed, the values of the annihilation fields have a broader distribution and thus the line separating one state or the other is

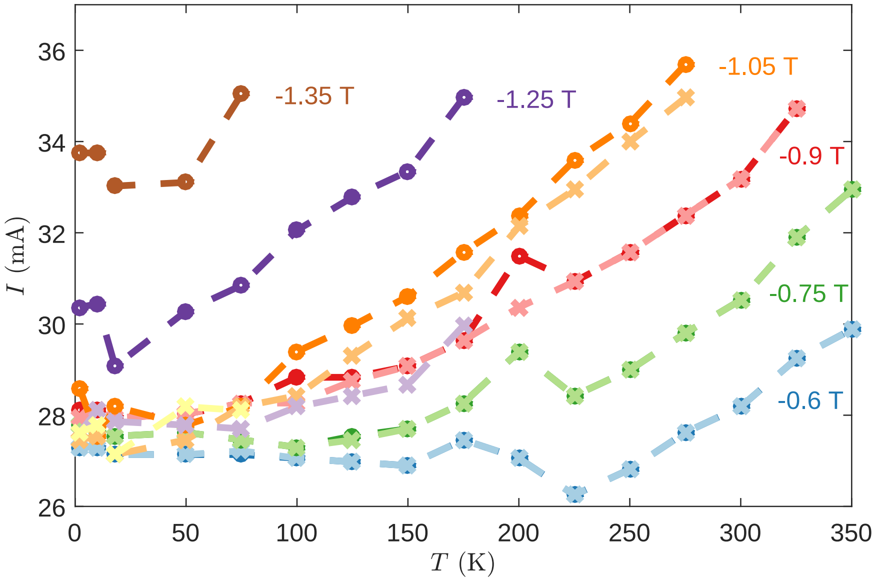

Figure 6.23: Creation (dark) and annihilation (light) currents as a function of temperature, for field values of -0.6 T (blue), -0.75 T (green), -0.9 T (red), -1.05 T (orange), -1.25 T (purple), and -1.35 T (brown).

not clearly defined. In this kind of plot all the temperature behavior of the droplet is summarized. For a fixed current, i.e. following a vertical line in the plot, we observe how the creation field decreases as the temperature increases. For a fixed field, i.e. following a horizontal line in the plot, the corresponding current value increases as the temperature increases. The critical field and current values follow opposite trends, but the trends are consistent in this map.

In summary, we have detected the dependance of the droplet characteristic parameters with temperature. The droplet solitons become less stable with increasing temperature; onset currents increase and the onset fields (coming from a high field) decrease. Also, in order to find the change in resistance ΔR associated to the droplet formation we have normalized the measured change by the change in MR at the corresponding field and temperature. Once this analysis is done, we observe a variation of the normalized change in resistance $\Delta\bar{R}/\bar{R}_0(T)$ with temperature.

In all our measurements we have observed that the droplet cannot be generated if the temperature is too high (around 350 K). This might be due to two effects. The first is that, as the temperature increases, the onset current also increases, and hence we do not reach such high values in the experiments. The other effect is due to the reduction in MR as the temperature increases. It would be possible

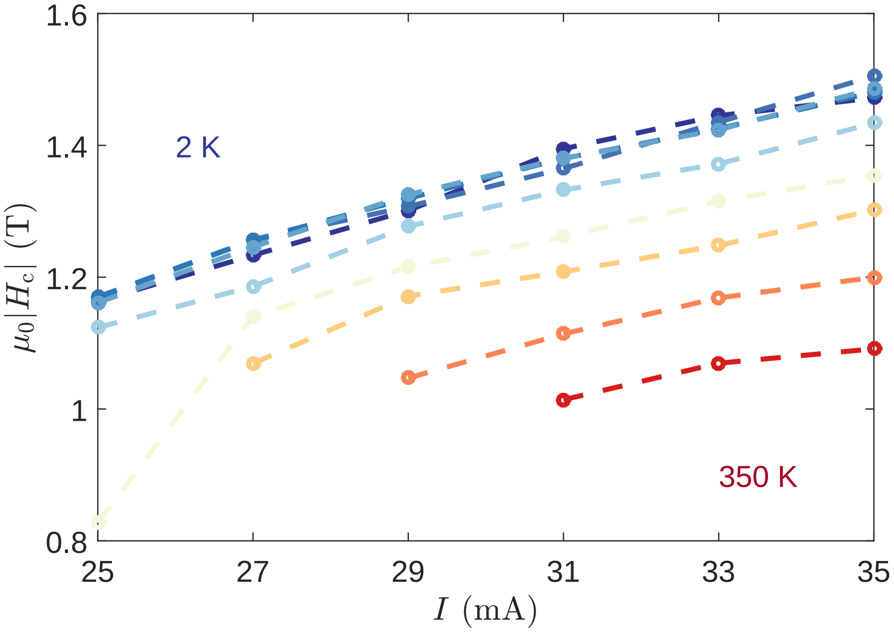

Figure 6.24: Change on the creation and annihilation currents as the temperea-ture is increased, from the measurements with fixed current.

that the droplet is generated, but the change in MR is smaller than the sensitivity in our equipment.

Moreover, the increase in the onset current with temperature contradicts the behavior in spin-valve magnetization switching, in which the increase temperature helps magnetization to reverse by lowering the effective barrier between states.

We may understand this behavior in the frame of drift displacements, as observed in the previous section. As temperature is lowered, pinning effects gain importance, hence helping to fix the droplet. This would have the effect of fixing the droplet once it is generated, not allowing it to move outside the nanocontact and being destroyed, resulting in an effective lower creation current. As temperature increases, the drift displacements become more important, and hence a higher current is needed to keep the droplet under the nanocontact. At the same time, the effective resistance is reduced, as the droplet goes out the nanocontact region for longer times. Spectral measurements at different temperatures are needed to elucidate this point.

The decrease of the resistance variation occurs always for fields higher than the saturation, as expected in the described framework. For fields below saturation, however, the variation increases with temperature, something that cannot be accounted for in this framework. We suggest that the current sweeps are not the most accurate kind of measurements for temperature-dependent data, because the current may heat the nanocontact region. Hence, the temperature on the nanocontact would not be stable during the current sweep.

6.5 Experiments of Random Telegraph Noise

In certain samples, we observed a continuous switching of the resistance between the values corresponding to droplet and no-droplet states (see Fig. 6.25) for some combinations of field, current, and temperature. This switching is typical of metastable systems, in which the system goes between levels at varying rates [Ralls et al. 1984]. This is known as *random telegraph noise* (RTN) [Simoen, Kaczer, et al. 2011]. The analysis of this noise allows determination of the energy barriers in a system [Kirschenbaum et al. 1995], and it was used to provide possible evidence of Macroscopic Quantum Tunneling in ErAs nanowires [Coppinger, Genoe, Maude, Gennser, et al. 1995; Coppinger, Genoe, Maude, Kleber, et al. 1998]. RTN typically appears in semiconductor CMOS [Hung et al. 1990] and MOSFETs [Simoen and Claeys 1999], and GMR read heads [Hardner et al. 1999]. It has also been detected in system excited with spin-transfer torque [Cascales, Herranz, Ebels, et al. 2015; K.-J. Lee et al. 2004]. The RTN in magnetic tunnel junctions [Cascales, Herranz, Sambricio, et al. 2013] has grown interest during the past years.

6.5.1 Experimental Details

To characterize this switching, the MR was measured continuously for around 60 s, at fixed values of temperature and field, and the current was step increased every ≈ 60 s. Depending on the conditions, the resistance during the 60 s measurement interval kept constant or continuously switched between different levels with different dwell times, see Fig 6.26. The measurements were repeated at three different temperatures (10 K, 150 K, and 300 K). At each temperature, the field needed to be adjusted to find the switching between states.

6.5.2 Results

The value of the resistance oscillates mainly between distinct discrete levels. The value of each level was found by first subtracting the increasing parabolic trend in resistance due to heating, and then counting the number of points at small resistance intervals, and plotting the distribution. The resulting histogram was adjusted to a gaussian centered at each maxima, which gives the mean value of the level. A value of resistance was accounted in a certain level if within 3σ of the

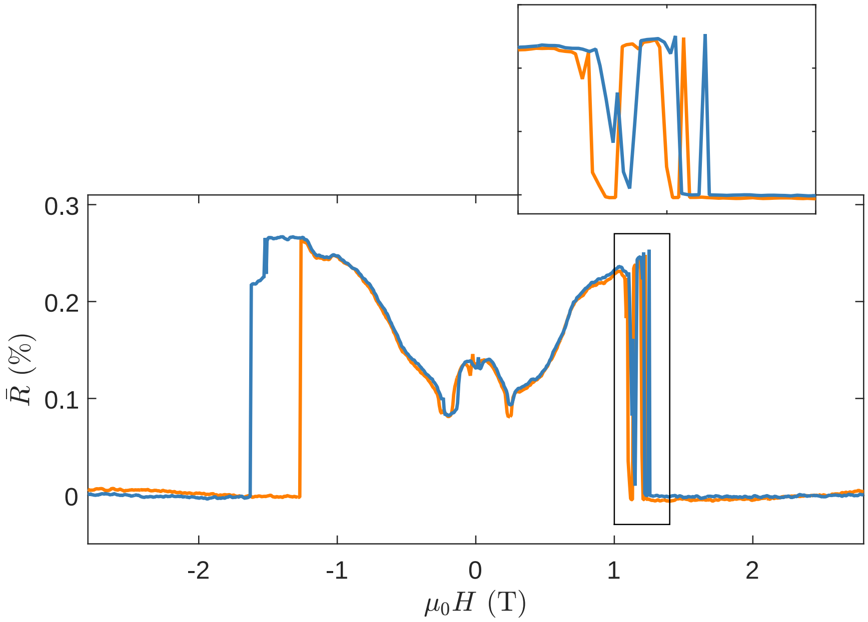

Figure 6.25: Magnetoresistance measurements in which random telegraph noise is observed only in the positive magnetic field branch, corresponding to $T = 100$ K and $I = 31$ mA.

corresponding mean resistance. For each 60 s sweep, the total time at each level, the dwell time and the number of switchings were accounted for.

The normalized population is the probability to find the system in a level is calculated by taking the total time in the level and dividing by the total measuring time of 60 s. Figure 6.27 shows the probability to find the system with no excitation and with an excitation, for the second set of measurements (at 150 K). We see that they are opposite, as expected. For low currents $I < 23.5$ mA the system is in the non-excited (NE) level. As the current is increased, there are more switching events from the NE level and the population of the NE level decreases as the E levels increase, and the switching events last for the next ≈ 2 mA. At $I \approx 25$ mA the population of the NE and E levels is the same. When the current is higher than 27 mA the system is in the E level corresponding to the droplet state.

This picture, however, does not describe the stability of the system in each state. In order to evaluate the stability one should obtain the rate at which the system switches. In order to obtain it, we average the dwell time τ—i.e. the time of remanence at a certain level before it switches to another level—at each current. The rate, hence, is the inverse of the dwell time $1/\tau$. Kirschenbaum et al. [1995] suggested an Arrhenius law to describe the characteristic rates of each state, since

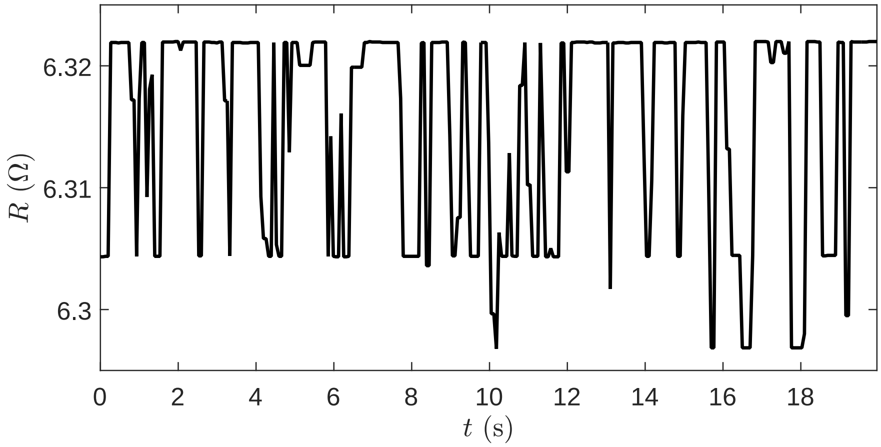

Figure 6.26: MR measured during ≈ 20 s, at a field $\mu_0 H = -1$ T, temperature $T = 150$ K, and current $I = 26.1$ mA.

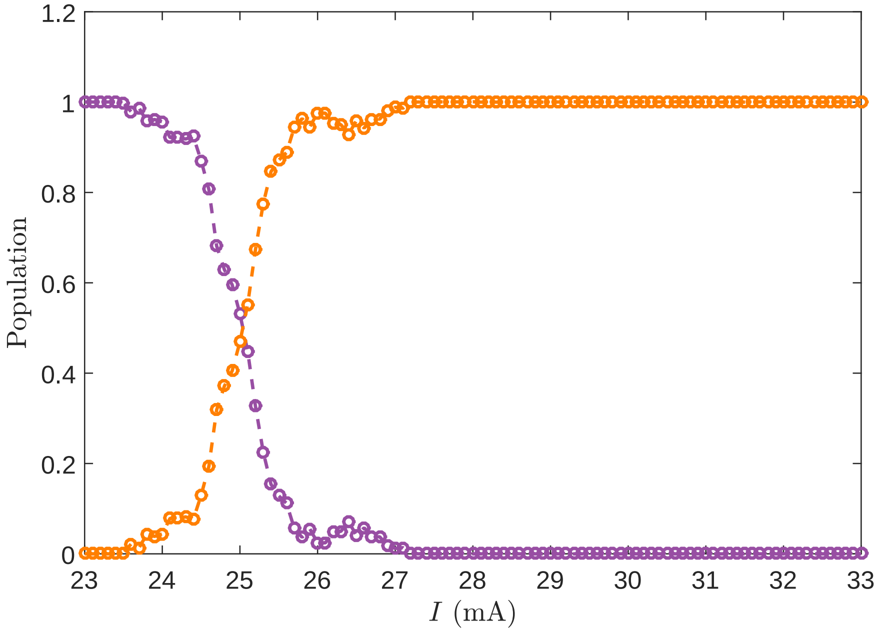

Figure 6.27: Population of the system without excitation (purple) and with excitations (orange) as a function of current, at field $\mu_0 H = -1$ T and temperature $T = 150$ K.

many two-level systems show thermally activated rates:

$$\frac{1}{\tau} = \frac{1}{\tau_0} \exp\left[-\frac{E(H,I,T)}{k_{\mathrm{B}}T}\right], \tag{6.15}$$

where $1/\tau_0$ is the characteristic frequency, $E(H, I, T)$ is the energy of the state which, in general, depends on field, current and temperature, and k_B is the Boltzmann constant. According to this, measurements at a fixed field and temperature will yield information on the dependance of the energy on current $E(I)$. Correspondingly, measurements at fixed current and temperature will give information on the energy dependance with field $E(H)$. This dependance comes from the Zeeman term and, hence, will give information on the variation of magnetization producing the fluctuations. Finally, temperature-dependent measurements will give information on the activation energy.

Figure 6.28 shows the mean of the dwell time as a function of current for the NE and E levels. The error bars represent the corresponding relative uncertainty, calculated as σ_τ/τ, with σ_τ the standard deviation of the dwell time. We observe that the relative uncertainty is higher for the excited level. This trend is also observable in the other sets of measures. A high relative uncertainty agrees with a broad distribution of dwell times, i.e. the system switches to another level with characteristic times that differ more.

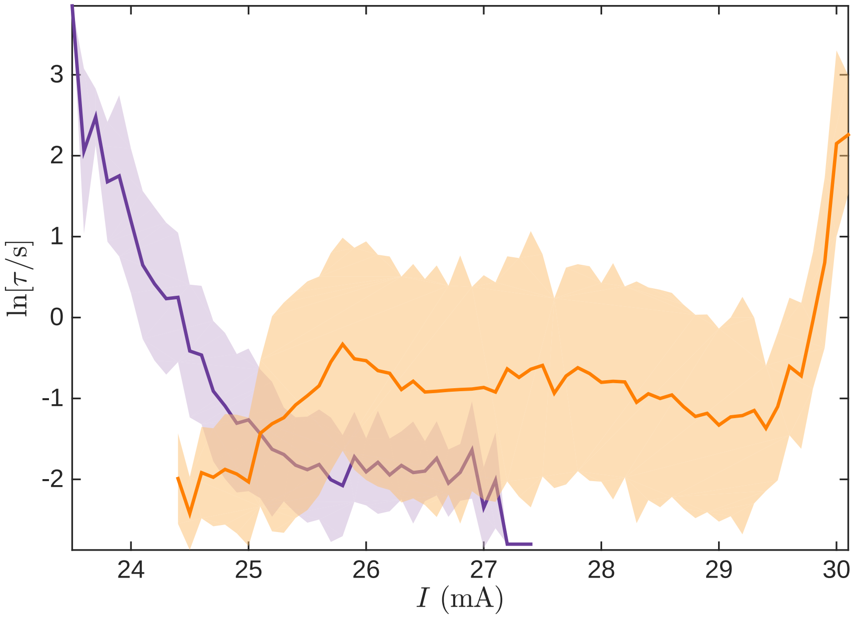

Figure 6.28: Plot of the dwell time dependence with current for the non-excited (purple) and excited (orange) levels at $T = 150$ K. The clear area corresponds to the distribution of dwell times at each current.

In order to evaluate this distribution of dwell times, we calculate the mean of the relative uncertainty along the entire current range for the NE and E levels

$\langle \sigma_\tau / \tau \rangle$. The corresponding values are summarized in Table 6.1, for the three different sets of measurements (T = 10 K, T = 150 K, and T = 300 K). The obtained mean value of the relative uncertainty, $\langle \sigma_\tau / \tau \rangle$, in the NE level hardly depends on temperature whereas the corresponding value for the E level increases with temperature.

Table 6.1: Summary of the distribution of dwell times.

Set	T (K)	$\mu_0 H$ (T)	$\langle \sigma_\tau / \tau \rangle$ [NE]	$\langle \sigma_\tau / \tau \rangle$ [E]
1	10	-1	0.62	1.29
2	150	-1	0.63	1.38
3	300	8.9	0.60	1.68

6.5.3 Discussion

The appearance of this RTN is not in contradiction with the drift resonances described in Section 6.3. We have indeed measured the low-frequency signal at the same time we measured RTN in samples at room temperature.

The broader distribution of relative uncertainties in the E level is in agreement with the higher instability of the annihilation field reported in Section 6.4. A broad distribution of the E level means that the system decays to the NE level with more randomness; a narrower distribution of the NE level means that the droplet creation is a more deterministic process. Notice that this is related with the energy barriers involved in both processes. It is interesting to observe that the barriers are different. We suggest that statistical measurements might help to determine the nature of the energy barriers.

Physics of this process involves a dynamic equilibrium, as shown in Fig 6.29. When the droplet is created, the resistance increases and, as a consequence, heat generation rises. A higher temperature means that a higher onset current is needed to generate the droplet, as reported in Section 6.4. If the applied current is not sufficient to stabilize the droplet at this higher temperature, the droplet annihilates and the temperature drops at the same time, which produces the cooling down of the sample, lowering the threshold current and allowing to droplet creation. In this frame, the droplet continuously creates and annihilates giving rise to the RTN, besides the drift instabilities reported before.

An striking feature that we have not studied for simplicity is the appearance of intermediate excited levels between the purely low-resistance non-droplet state, and the high-resistance droplet state with the FL and PL magnetization reversed, see Fig. 6.30. These states play an important role at lower temperatures (noticeably the measured 10 K and 150 K), and not so much at 300 K. As the system

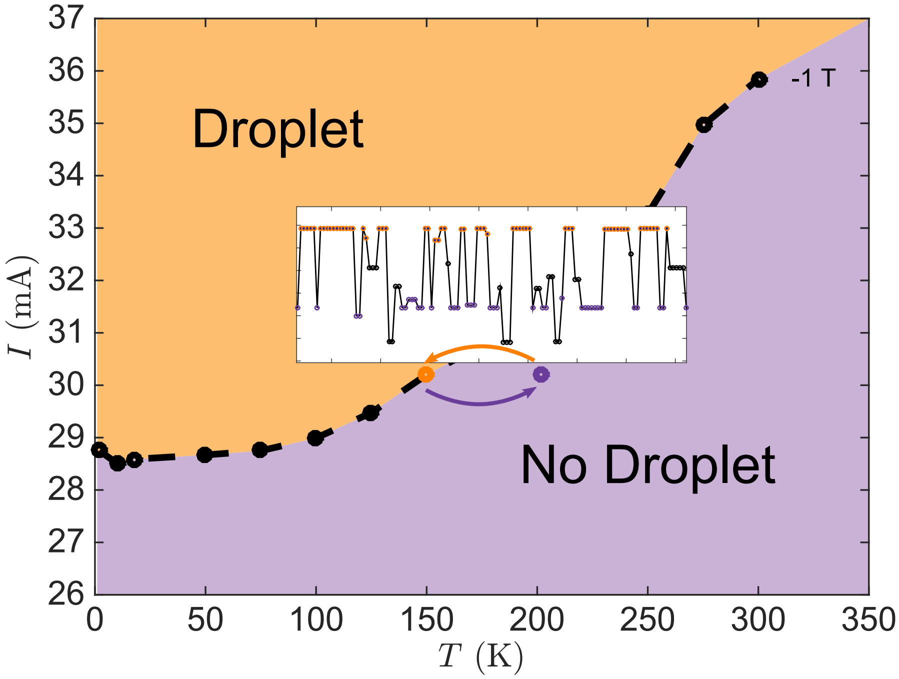

Figure 6.29: RTN as a switching between droplet and no droplet states as the sample is warmed up when the droplet is created, and the current supplied is not high enough to produce droplet.

goes from the non-droplet state to the high-resistance droplet state, it first passes through these intermediate states. These intermediate states change from one sample to another, and we attribute them to excitations of the magnetization. The pinning is also affecting these excitations, as the intermediate excitations are more noticeable at lower temperatures.

6.6 Conclusions

In conclusion, in Section 6.3 we have observed and measured drift instabilities in magnetic dissipative droplet solitons and have proved that droplet solitons may still exist and be stable at room temperature. We suggest that the drift instability is produced by an effective field asymmetry in the nanocontact region that can have different origins.

In section 6.4 we have observed how temperature affects the droplet. We attribute the onset current behavior, and equivalently the creation field, to pinning. The pinning has the effect of lowering the onset current as drift instabilities are

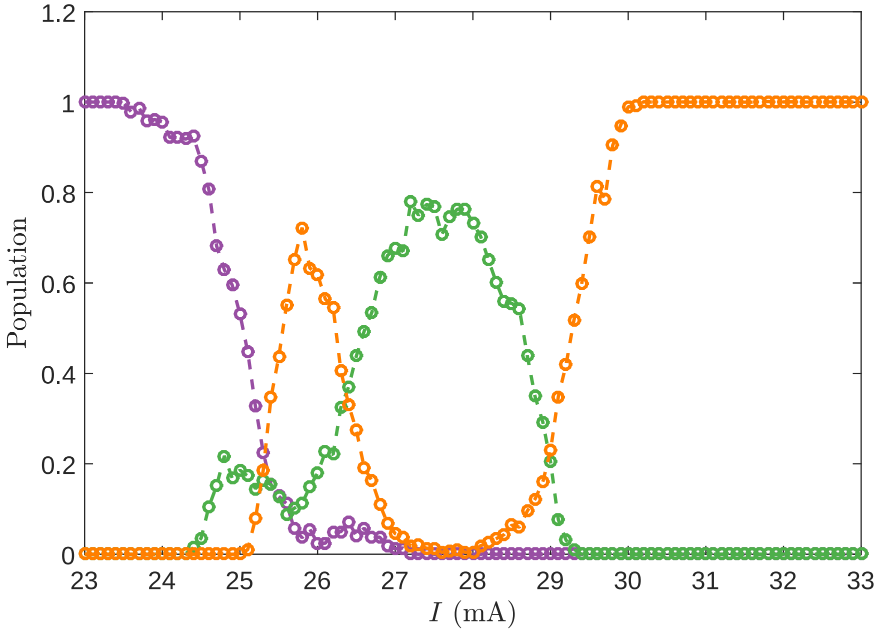

Figure 6.30: Population for levels 1 (purple) corresponding to a non-excited level, 2 (green) and 3 (orange) corresponding to the droplet, for all the measured currents.

no longer capable of overcoming the pinning potential. The pinning increases as the temperatures goes down, and hence it fixes the droplet more.

Finally, in section 6.5 we studied the RTN appearing close to the onset of the droplet. We have characterized the noise and attributed it to dynamic changes in the thermal properties of the nanocontact, which are in agreement to the pinning model.

7

General Conclusions and Future Work

7.1 Conclusions

Throughout the thesis we have seen the importance of studying the magnetization dynamics to understand new phenomena in different magnetic systems. In the first part of the thesis we have studied systems that allowed a macroscopic-spin model where spatial variations of magnetization were neglected. We developed a theory that set the requirements for the observation of the rotational Doppler effect in a ferromagnetic system and we measured quantum effects in randomly oriented nanoparticles of a single-molecule magnet, which might be a good candidate for the observation of the Doppler effect. In the second part of the thesis, we studied the magnetization dynamics in macroscopic systems that required a spatial dependence of the magnetic moment. We have been able to generate and control the dynamic states of the magnetic domains with oscillating fields, in the case of magnetic vortices, and with electrical currents, in the case of droplet solitons.

In Chapter 3, we have explored the effect of rotation on a ferromagnetic body. We have derived a general expression of the shift in the FMR produced by the rotation. From the general expression we deduced that there is a shift only when the symmetry of the body is broken. This asymmetry can come from the magnetocrystalline anisotropy or from the shape anisotropy. We have computed the power absorbed by a rotating body affected by a linearly polarized wave near the FMR frequency. We have obtained that the main resonance peak shifts proportional to the rotation velocity, and a second, small peak arises at a frequency separated twice the rotation velocity from the main FMR peak. We argue that the observation of such a displacement would be observable in high-precision experiments in which the position of the FMR can be determined with an accuracy of 1 kHz or better. Another system in which this effect may be observed consists of the so called free rotors.

In Chapter 4, we studied nanoparticles of Mn_{12}, which could be embedded in a matrix to obtain free rotors. This compound also presents quantum effects, which could enrich the behavior under rotations. In our experiments in randomly oriented nanospheres of Mn_{12}, we observed characteristic behavior of macroscopic quantum tunneling. As this was unexpected (normally oriented crystals are needed), we developed a model that accounts for the peaks observed in the derivative of the magnetization with respect to field. This model predicts the appearance of peaks at the resonant fields and the magnetization following a $1/H^2$ law. We confirmed this behavior in randomly oriented microcrystals. We argue that this result shall ease the characterization process to find molecules with resonant spin tunneling.

The dynamics of magnetic domains is studied in Chapters 5 and 6. In Chapter 5 we have worked with magnetic vortices created in elongated samples. We have excited an array of ellipses with one- an two-vortex states and we have observed the appearance of a vortex-antivortex-vortex state in spectral measurements as well as in MFM images. These results indicate that antivortex formation is possible in samples with a simple structure, making it easier to experimentally study the dynamics of the antivortex. In thick stadium-shape samples we have observed a much more complex frequency response. With the comparison of MFM and micromagnetic simulations, we argue that the samples have a core consisting of an out-of-plane magnetization that moves inside the thick sample. However, the exact frequency response of such an elongated core is still to be determined.

Finally, in Chapter 6 we use electrical currents to generate and study the dynamics of the magnetic domains. We report measurements in nanocontacts to ferromagnetic thin films with PMA. We have observed the formation of dissipative droplet solitons and a low-frequency response that we attribute to movement of the soliton due to drift instabilities. Through micromagnetic simulations, we give some possible origins of the drift instability, consisting of effective asymmetries of the field in the nanocontact. These results explain previous measurements with a partial reversal of the magnetization. Future studies should take into account the drift instabilities of the droplet to stabilize it. We have also measured the temperature dependence of the characteristic creation and annihilation parameters of the droplet. We have observed an increase with temperature on the creation current and a decrease in the creation field. This indicates that the droplet is easier to form at low temperatures. We argue that this is produced by pinning of the droplet, as the effects of pinning are higher at low temperatures. This opens new questions on what are the energies involved in the droplet and how we can control them.

Different experimental methods have been used. The magnetization states have been recorded with SQUID magnetometry and MFM imaging. Analyzing the magnetization obtained with SQUID magnetometry, we have been able to as-certain the barriers of the magnetic systems and record the slow dynamics of the overall magnetization. With MFM imaging and micromagnetic simulations, we have established the stable magnetic configuration of different structures, allowing, this time, the determination of spatial variations of the magnetization. We have used spectral measurements to record the fast magnetization dynamics of domain structures. We have also used transport measurements to determine the magnetization state of spintronic devices. Moreover, the transport measurements were also done in a cryostat to be able to reach temperatures of 2 K. Different nanofabrication techniques have been implemented to develop the devices: optical lithography, electron-beam lithography, electron-beam evaporation, and sputtering. These are only a part of a great variety of methods available to study the magnetization dynamics, which makes this field challenging and thrilling.

7.2 Future Work

Our studies of the dynamics of two different magnetic domains—magnetic vortices and droplet solitons—we have shown the capability to control the state of the system, with microwave pulses in the case of vortices, and with a current in solitons. The measurements were done in systems with a small number of elements, or even a single element. This is useful to understand the physics of the system, but it produces a small signal. Applications require a high-power signal, which can be obtained with a large array of elements. However, each element of the array should respond similarly, otherwise the system is difficult to control. As a matter of fact, this was the issue reported in Chapter 5, in which we had a large array of ellipses that ended in different magnetic configurations. Therefore, it is of great importance to study the synchronization of different elements in an array. This is, in fact, a matter of recent studies in both magnetic vortices and droplet solitons.

Synchronization in an array of magnetic entities is produced through propagating spin waves. It has been shown that a Doppler effect might be produced in the propagation of a spin wave in a ferromagnet subject to a current. The Doppler effect, hence, could play a role in the synchronization, when a current is needed. Furthermore, recent studies argue that a rotation on a ferromagnetic body could generate a current. This could be used for new devices with low consumption.

Other attempts to synchronize the magnetization are done with surface acoustic waves (SAW). SAW may also allow the propagation and directionality of spin waves in a circuit. Additionally, SAW are also used to excite the magnetization, and some experiments have used SAW to excite FMR. Using SAW to excite the magnetization in magnetic vortices, or to propagate magnetic droplet solitons, might have the advantage of requiring low currents. SAW-induced excitations could also be used to produce magnetization reversal in nanoparticles, similar to some experiments that used them to ignite magnetic avalanches in Mn_{12} crystals and other compounds.

Bibliography

d'Albuquerque e Castro, J., D. Altbir, J. C. Retamal, and P. Vargas, "Scaling Approach to the Magnetic Phase Diagram of Nanosized Systems," Phys. Rev. Lett. **88**, 237202 (2002) (cit. on pp. 55, 57).

Anderson, J. D. and B. Mashhoon, "Pioneer anomaly and the helicity-rotation coupling," Phys. Lett. A **315**, 199–202 (2003) (cit. on p. 21).

Arrott, A. and R. Hertel, "Large amplitude oscillations (switching) of bi-stable vortex structures in zero field," J. Magn. Magn. Mater. **322**, 1389–1391 (2010) (cit. on p. 74).

Ashby, N., "Relativity in the Global Positioning System," Living Rev. Relativ. **6** (2003) `10.12942/lrr-2003-1` (cit. on p. 21).

Ashcroft, N. W. and N. D. Mermin, *Solid state physics* (Saunders College, 1976), (cit. on pp. 10, 11, 102).

Backes, D., F. Macià, S. Bonetti, R. Kukreja, H. Ohldag, and A. D. Kent, "Direct Observation of a Localized Magnetic Soliton in a Spin-Transfer Nanocontact," Phys. Rev. Lett. **115**, 127205 (2015) (cit. on pp. 78, 98).

Baibich, M. N., J. M. Broto, A. Fert, F. N. Van Dau, and F. Petroff, "Giant Magnetoresistance of (001)Fe/(001)Cr Magnetic Superlattices," Phys. Rev. Lett. **61**, 2472–2475 (1988) (cit. on p. 79).

Barbara, B., W. Wernsdorfer, L. Sampaio, J. Park, C. Paulsen, M. Novak, R. Ferré, D. Mailly, R. Sessoli, A. Caneschi, K. Hasselbach, A. Benoit, and L. Thomas, "Mesoscopic quantum tunneling of the magnetization," J. Magn. Magn. Mater. **140-144**, 1825–1828 (1995) (cit. on p. 39).

del Barco, E., J. M. Hernandez, M. Sales, J. Tejada, H. Rakoto, J. M. Broto, and E. M. Chudnovsky, "Spin-phonon avalanches in Mn_{12} acetate," Phys. Rev. B **60**, 11898–11901 (1999) (cit. on pp. 34, 39).

Barman, A., S. Barman, T. Kimura, Y. Fukuma, and Y. Otani, "Gyration mode splitting in magnetostatically coupled magnetic vortices in an array," J. Phys. D. Appl. Phys. **43**, 422001 (2010) (cit. on p. 61).

Barreiro, S., J. W. R. Tabosa, H. Failache, and A. Lezama, "Spectroscopic Observation of the Rotational Doppler Effect," Phys. Rev. Lett. **97**, 113601 (2006) (cit. on p. 22).

Bartolomé, J., F. Luis, and J. F. Fernández, eds., *Molecular Magnets: Physics and Applications* (Springer-Verlag Berlin Heidelberg, 2014), (cit. on p. 35).

Basistiy, I. V., A. Y. Bekshaev, M. V. Vasnetsov, V. V. Slyusar, and M. S. Soskin, "Observation of the rotational doppler effect for optical beams with helical wave front using spiral zone plate," J. Exp. Theor. Phys. Lett. **76**, 486–489 (2002) (cit. on pp. 20, 22).

Bertaina, S., S. Gambarelli, T. Mitra, B. Tsukerblat, A. Müller, and B. Barbara, "Quantum oscillations in a molecular magnet.," Nature **453**, 203–6 (2008) (cit. on p. 34).

Binasch, G., P. Grünberg, F. Saurenbach, and W. Zinn, "Enhanced magnetoresistance in layered magnetic structures with antiferromagnetic interlayer exchange," Phys. Rev. B **39**, 4828–4830 (1989) (cit. on p. 79).

Bogani, L. and W. Wernsdorfer, "Molecular spintronics using single-molecule magnets.," Nat. Mater. **7**, 179–86 (2008) (cit. on p. 30).

Bohlens, S., B. Krüger, A. Drews, M. Bolte, G. Meier, and D. Pfannkuche, "Current controlled random-access memory based on magnetic vortex handedness," Appl. Phys. Lett. **93**, 142508 (2008) (cit. on p. 54).

Bonetti, S. and J. Åkerman, "Nano-Contact Spin-Torque Oscillators as Magnonic Building Blocks," in *Magnonics*, Vol. 125, edited by S. O. Demokritov and A. N. Slavin, Topics in Applied Physics (Springer Berlin Heidelberg, Berlin, Heidelberg, 2013), pp. 177–187 (cit. on p. 78).

Bonetti, S., R. Kukreja, Z. Chen, F. Macià, J. M. Hernàndez, A. Eklund, D. Backes, J. Frisch, J. Katine, G. Malm, S. Urazhdin, A. D. Kent, J. Stöhr, H. Ohldag, and H. A. Dürr, "Direct observation and imaging of a spin-wave soliton with $p-$like symmetry," (2015), arXiv:`1504.00144` (cit. on p. 78).

Bonetti, S., V. Tiberkevich, G. Consolo, G. Finocchio, P. Muduli, F. Mancoff, A. Slavin, and J. Åkerman, "Experimental Evidence of Self-Localized and Propagating Spin Wave Modes in Obliquely Magnetized Current-Driven Nanocontacts," Phys. Rev. Lett. **105**, 217204 (2010) (cit. on p. 86).

Boust, F. and N. Vukadinovic, "Micromagnetic simulations of vortex-state excitations in soft magnetic nanostructures," Phys. Rev. B **70**, 172408 (2004) (cit. on p. 73).

Brataas, A., A. D. Kent, and H. Ohno, "Current-induced torques in magnetic materials.," Nat. Mater. **11**, 372–81 (2012) (cit. on pp. 80, 81).

Bretenaker, F. and A. Le Floch, "Energy exchanges between a rotating retardation plate and a laser beam," Phys. Rev. Lett. **65**, 2316–2316 (1990) (cit. on p. 22).

Buchanan, K. S., P. E. Roy, M. Grimsditch, F. Y. Fradin, K. Y. Guslienko, S. D. Bader, and V. Novosad, "Soliton-pair dynamics in patterned ferromagnetic ellipses," Nat. Phys. **1**, 172–176 (2005) (cit. on pp. 54, 63).

——, "Magnetic-field tunability of the vortex translational mode in micron-sized permalloy ellipses: Experiment and micromagnetic modeling," Phys. Rev. B **74** (2006) `10.1103/PhysRevB.74.064404` (cit. on pp. 54, 63).

Bussmann, K., G. A. Prinz, S.-F. Cheng, and D. Wang, "Switching of vertical giant magnetoresistance devices by current through the device," Appl. Phys. Lett. **75**, 2476 (1999) (cit. on p. 54).

Caputo, J.-G., Y. Gaididei, F. Mertens, and D. Sheka, "Vortex Polarity Switching by a Spin-Polarized Current," Phys. Rev. Lett. **98**, 056604 (2007) (cit. on p. 60).

Carbonera, C., I. Imaz, D. Maspoch, D. Ruiz-Molina, and F. Luis, "Magnetic behaviour of Mn12 single-molecule magnet nanospheres," Inorganica Chim. Acta **361**, 3951–3956 (2008) (cit. on pp. 34, 35, 44, 45, 49).

Cascales, J. P., D. Herranz, U. Ebels, J. A. Katine, and F. G. Aliev, "Detection of spin torque magnetization dynamics through low frequency noise," Appl. Phys. Lett. **107**, 052401 (2015) (cit. on p. 109).

Cascales, J. P., D. Herranz, J. L. Sambricio, U. Ebels, J. A. Katine, and F. G. Aliev, "Magnetization reversal in sub-100 nm magnetic tunnel junctions with ultrathin MgO barrier biased along the hard axis," Appl. Phys. Lett. **102**, 092404 (2013) (cit. on p. 109).

Castillo-Sepúlveda, S., D. Altbir, N. M. Vargas, and S. Allende, "Mechanisms of magnetization reversal in stadium-shaped particles," J. Appl. Phys. **112**, 083906 (2012) (cit. on pp. 67, 68).

Champeney, D. C. and P. B. Moon, "Absence of Doppler Shift for Gamma Ray Source and Detector on Same Circular Orbit," Proc. Phys. Soc. **77**, 350–352 (1961) (cit. on p. 21).

Chen, L. and W. She, "Sorting photons of different rotational Doppler shifts (RDS) by orbital angular momentum of single-photon with spin-orbit-RDS entanglement," Opt. Express **16**, 14629 (2008) (cit. on p. 22).

Cheynis, F., A. Masseboeuf, O. Fruchart, N. Rougemaille, J. C. Toussaint, R. Belkhou, P. Bayle-Guillemaud, and A. Marty, "Controlled Switching of Néel Caps in Flux-Closure Magnetic Dots," Phys. Rev. Lett. **102**, 107201 (2009) (cit. on p. 74).

Chikazumi, S. and C. D. Graham, *Physics of Ferromagnetism*, 2nd., International Series of Monographs on Physics (Clarendon Press, 1997), (cit. on pp. 7, 10–12, 15, 16, 94, 102).

Choe, S. B., Y. Acremann, A. Scholl, A. Bauer, A. Doran, J. Stöhr, and H. A. Padmore, "Vortex core-driven magnetization dynamics.," Science **304**, 420–2 (2004) (cit. on p. 59).

Christou, G., D. Gatteschi, D. N. Hendrickson, and R. Sessoli, "Single-Molecule Magnets," MRS Bull. **25**, 66–71 (2000) (cit. on p. 36).

Chudnovsky, E. M., "Conservation of angular momentum in the problem of tunneling of the magnetic moment," Phys. Rev. Lett. **72**, 3433–3436 (1994) (cit. on p. 24).

Chudnovsky, E. M. and D. A. Garanin, "Rotational states of a nanomagnet," Phys. Rev. B **81**, 214423 (2010) (cit. on p. 30).

Chudnovsky, E. M., D. A. Garanin, and R. Schilling, "Universal mechanism of spin relaxation in solids," Phys. Rev. B **72**, 094426 (2005) (cit. on p. 24).

Chudnovsky, E. M. and J. Tejada, "Evidence of the Extended Orientational Order in Amorphous Alloys Obtained from Magnetic Measurements," Europhys. Lett. **23**, 517–522 (1993) (cit. on p. 49).

——, *Macroscopic Quantum Tunneling of the Magnetic Moment* (Cambridge University Press, Cambridge, 1998) (cit. on pp. 36, 38).

——, *Lectures on Magnetism: With 128 Problems* (Rinton Press, 2006), (cit. on pp. 7, 9, 11, 15–17, 24, 27, 38, 102).

Chung, S., S. M. Mohseni, S. R. Sani, E. Iacocca, R. K. Dumas, T. N. Anh Nguyen, Y. Pogoryelov, P. K. Muduli, A. Eklund, M. Hoefer, and J. Åkerman, "Spin transfer torque generated magnetic droplet solitons (invited)," J. Appl. Phys. **115**, 172612 (2014) (cit. on pp. 78, 86, 100).

Chung, S.-H., R. D. McMichael, D. T. Pierce, and J. Unguris, "Phase diagram of magnetic nanodisks measured by scanning electron microscopy with polarization analysis," Phys. Rev. B **81**, 024410 (2010) (cit. on p. 55).

Chupas, P. J., X. Qiu, J. C. Hanson, P. L. Lee, C. P. Grey, and S. J. L. Billinge, "Rapid-acquisition pair distribution function (RA-PDF) analysis," J. Appl. Crystallogr. **36**, 1342–1347 (2003) (cit. on p. 41).

Coppinger, F., J. Genoe, D. K. Maude, U. Gennser, J. C. Portal, K. E. Singer, P. Rutter, T. Taskin, A. R. Peaker, and A. C. Wright, “Single Domain Switching Investigated Using Telegraph Noise Spectroscopy: Possible Evidence for Macroscopic Quantum Tunneling,” Phys. Rev. Lett. **75**, 3513–3516 (1995) (cit. on p. 109).

Coppinger, F., J. Genoe, D. K. Maude, X. Kleber, L. B. Rigal, U. Gennser, J. C. Portal, K. E. Singer, P. Rutter, T. Taskin, A. R. Peaker, and A. C. Wright, “Magnetic characterization of self-organized ErAs clusters using telegraph noise spectroscopy,” Phys. Rev. B **57**, 7182–7189 (1998) (cit. on p. 109).

Cornia, A., A. C. Fabretti, R. Sessoli, L. Sorace, D. Gatteschi, A.-L. Barra, C. Daiguebonne, and T. Roisnel, “Disorder effects in Mn_{12} –acetate at 83 K,” Acta Crystallogr. Sect. C Cryst. Struct. Commun. **58**, m371–m373 (2002) (cit. on p. 41).

Corona, R., D. Altbir, and J. Escrig, “Magnetic properties of elliptical and stadium-shaped nanoparticles: Effect of the shape anisotropy,” J. Magn. Magn. Mater. **324**, 3824–3828 (2012) (cit. on pp. 67, 68).

Courtial, J., K. Dholakia, D. A. Robertson, L. Allen, and M. J. Padgett, “Measurement of the Rotational Frequency Shift Imparted to a Rotating Light Beam Possessing Orbital Angular Momentum,” Phys. Rev. Lett. **80**, 3217–3219 (1998) (cit. on p. 22).

Cowburn, R. P., “Magnetic nanodots for device applications,” J. Magn. Magn. Mater. **242-245**, 505–511 (2002) (cit. on p. 54).

Cowburn, R. P., D. K. Koltsov, A. O. Adeyeye, and M. E. Welland, “Single-Domain Circular Nanomagnets,” Phys. Rev. Lett. **83**, 1042–1045 (1999) (cit. on pp. 55, 59).

Curcic, M., H. Stoll, M. Weigand, V. Sackmann, P. Juellig, M. Kammerer, M. Noske, M. Sproll, B. Van Waeyenberge, A. Vansteenkiste, G. Woltersdorf, T. Tyliszczak, and G. Schütz, “Magnetic vortex core reversal by rotating magnetic fields generated on micrometer length scales,” Phys. status solidi **248**, 2317–2322 (2011) (cit. on pp. 60, 66).

Denysenkov, V. P. and a. M. Grishin, “Broadband ferromagnetic resonance spectrometer,” Rev. Sci. Instrum. **74**, 3400–3405 (2003) (cit. on p. 62).

Ding, J., S. Jain, J. E. Pearson, S. Lendinez, V. Khovaylo, and V. Novosad, “Dynamic control of metastable remanent states in mesoscale magnetic elements,” J. Appl. Phys. **117**, 17A707 (2015) (cit. on pp. 69, 74, 75).

Ding, J., G. N. Kakazei, X. Liu, K. Y. Guslienko, and A. O. Adeyeye, "Higher order vortex gyrotropic modes in circular ferromagnetic nanodots.," Sci. Rep. **4**, 4796 (2014) (cit. on pp. 74, 75).

Drews, A., B. Krüger, G. Meier, S. Bohlens, L. Bocklage, T. Matsuyama, and M. Bolte, "Current- and field-driven magnetic antivortices for nonvolatile data storage," Appl. Phys. Lett. **94**, 062504 (2009) (cit. on p. 54).

Friedman, J. R., M. P. Sarachik, J. Tejada, and R. Ziolo, "Macroscopic Measurement of Resonant Magnetization Tunneling in High-Spin Molecules," Phys. Rev. Lett. **76**, 3830–3833 (1996) (cit. on pp. 33, 34, 38, 39, 50, 51).

Ganzhorn, M., S. Klyatskaya, M. Ruben, and W. Wernsdorfer, "Carbon nanotube nanoelectromechanical systems as magnetometers for single-molecule magnets.," ACS Nano **7**, 6225–36 (2013) (cit. on p. 34).

———, "Strong spin-phonon coupling between a single-molecule magnet and a carbon nanotube nanoelectromechanical system.," Nat. Nanotechnol. **8**, 165–9 (2013) (cit. on p. 34).

Garetz, B. A. and S. Arnold, "Variable frequency shifting of circularly polarized laser radiation via a rotating half-wave retardation plate," Opt. Commun. **31**, 1–3 (1979) (cit. on pp. 20, 22).

Guslienko, K. Y., B. A. Ivanov, V. Novosad, Y. Otani, H. Shima, and K. Fukamichi, "Eigenfrequencies of vortex state excitations in magnetic submicron-size disks," J. Appl. Phys. **91**, 8037–8039 (2002) (cit. on pp. 59, 60).

Guslienko, K. Y., K.-S. Lee, and S.-K. Kim, "Dynamic Origin of Vortex Core Switching in Soft Magnetic Nanodots," Phys. Rev. Lett. **100**, 027203 (2008) (cit. on p. 66).

Ha, J. K., R. Hertel, and J. Kirschner, "Configurational stability and magnetization processes in submicron permalloy disks," Phys. Rev. B **67**, 064418 (2003) (cit. on p. 58).

———, "Micromagnetic study of magnetic configurations in submicron permalloy disks," Phys. Rev. B **67**, 224432 (2003) (cit. on p. 58).

Hardner, H., M. Hurben, and N. Tabat, "Noise and magnetic domain fluctuations in spin-valve GMR heads," IEEE Trans. Magn. **35**, 2592–2594 (1999) (cit. on p. 109).

Hartmann-Boutron, F., P. Politi, and J. Villain, "Tunneling and Magnetic Relaxation in Mesoscopic Molecules," Int. J. Mod. Phys. B **10**, 2577–2637 (1996) (cit. on p. 24).

Hay, H. J., J. P. Schiffer, T. E. Cranshaw, and P. A. Egelstaff, “Measurement of the Red Shift in an Accelerated System Using the Mössbauer Effect in Fe 57,” Phys. Rev. Lett. **4**, 165–166 (1960) (cit. on p. 21).

Hehl, F. W. and W.-T. Ni, “Inertial effects of a Dirac particle,” Phys. Rev. D **42**, 2045–2048 (1990) (cit. on p. 23).

Heinze, S., K. von Bergmann, M. Menzel, J. Brede, A. Kubetzka, R. Wiesendanger, G. Bihlmayer, and S. Blügel, “Spontaneous atomic-scale magnetic skyrmion lattice in two dimensions,” Nat. Phys. **7**, 713–718 (2011) (cit. on p. 84).

Hernandez, J. M., F. Torres, J. Tejada, and E. Molins, “Crystal defects and spin tunneling in single crystals of Mn_{12} clusters,” Phys. Rev. B **66**, 161407 (2002) (cit. on p. 34).

Hernàndez, J. M., X. X. Zhang, F. Luis, J. Bartolomé, J. Tejada, and R. Ziolo, “Field tuning of thermally activated magnetic quantum tunnelling in Mn_{12} - Ac molecules,” Europhys. Lett. **35**, 301–306 (1996) (cit. on pp. 34, 38).

Hernandez, J. M., X. X. Zhang, F. Luis, J. Tejada, J. R. Friedman, M. P. Sarachik, and R. Ziolo, “Evidence for resonant tunneling of magnetization in Mn_{12} sacetate complex,” Phys. Rev. B **55**, 5858–5865 (1997) (cit. on p. 34).

Hernández-Mínguez, A., J. M. Hernandez, F. Macià, A. García-Santiago, J. Tejada, and P. V. Santos, “Quantum Magnetic Deflagration in Mn_{12} Acetate,” Phys. Rev. Lett. **95**, 217205 (2005) (cit. on p. 34).

Hertel, R. and C. Schneider, “Exchange Explosions: Magnetization Dynamics during Vortex-Antivortex Annihilation,” Phys. Rev. Lett. **97**, 177202 (2006) (cit. on p. 66).

Hoefer, M. A., T. J. Silva, and M. W. Keller, “Theory for a dissipative droplet soliton excited by a spin torque nanocontact,” Phys. Rev. B **82**, 054432 (2010) (cit. on pp. 78, 84, 93, 100).

Hoefer, M. A., M. Sommacal, and T. J. Silva, “Propagation and control of nanoscale magnetic-droplet solitons,” Phys. Rev. B **85**, 214433 (2012) (cit. on p. 93).

Huber, R. and D. Grundler, “Ferromagnetic nanodisks for magnonic crystals and waveguides,” in Spie nanosci. + eng. Edited by H.-J. M. Drouhin, J.-E. Wegrowe, and M. Razeghi (2011), pp. 81000D–81000D–8 (cit. on p. 54).

Hubert, A. and R. Schäfer, *Magnetic Domains: The Anlaysis of Magnetic Microstructures* (Springer-Verlag Berlin Heidelberg, Berlin, 1998) (cit. on p. 54).

Hung, K., P. Ko, C. Hu, and Y. Cheng, "Random telegraph noise of deep-submicrometer MOSFETs," IEEE Electron Device Lett. **11**, 90–92 (1990) (cit. on p. 109).

Ieda, J., M. Matsuo, and S. Maekawa, "Theory of mechanical spin current generation via spin–rotation coupling," Solid State Commun. **198**, 52–56 (2014) (cit. on p. 22).

Imaz, I., F. Luis, C. Carbonera, D. Ruiz-Molina, and D. Maspoch, "Single-molecule magnet behaviour in metal-organic nanospheres generated by simple precipitation of Mn12O12 clusters.," Chem. Commun. (Camb)., 1202–4 (2008) (cit. on pp. 34, 35, 39, 44, 45, 49).

Ivanov, B. A. and A. M. Kosevich, "Bound states of large number of magnons in a three-dimensional ferromagnet (magnons drops)," Zh. Eksp. Teor. Fiz. **24**, 495–499 (1976) (cit. on p. 83).

———, "Bound states of a large number of magnons in a ferromagnet with a single-ion anisotropy," Zh. Eksp. Teor. Fiz. **72**, 2000–2015 (1977) (cit. on p. 83).

Jain, S., V. Novosad, F. Y. Fradin, J. E. Pearson, V. Tiberkevich, A. N. Slavin, and S. D. Bader, "From chaos to selective ordering of vortex cores in interacting mesomagnets.," Nat. Commun. **3**, 1330 (2012) (cit. on pp. 54, 55, 62, 63, 65).

Jain, S., H. Schultheiss, O. Heinonen, F. Y. Fradin, J. E. Pearson, S. D. Bader, and V. Novosad, "Coupled vortex oscillations in mesoscale ferromagnetic double-disk structures," Phys. Rev. B **86**, 214418 (2012) (cit. on pp. 64, 65).

Juhás, P., T. Davis, C. L. Farrow, and S. J. L. Billinge, "PDFgetX3 : a rapid and highly automatable program for processing powder diffraction data into total scattering pair distribution functions," J. Appl. Crystallogr. **46**, 560–566 (2013) (cit. on p. 41).

Julliere, M., "Tunneling between ferromagnetic films," Phys. Lett. A **54**, 225–226 (1975) (cit. on p. 79).

Kakazei, G. N., P. E. Wigen, K. Y. Guslienko, R. W. Chantrell, N. A. Lesnik, V. Metlushko, H. Shima, K. Fukamichi, Y. Otani, and V. Novosad, "In-plane and out-of-plane uniaxial anisotropies in rectangular arrays of circular dots studied by ferromagnetic resonance," J. Appl. Phys. **93**, 8418 (2003) (cit. on p. 67).

Kammerer, M., M. Weigand, M. Curcic, M. Noske, M. Sproll, A. Vansteenkiste, B. Van Waeyenberge, H. Stoll, G. Woltersdorf, C. H. Back, and G. Schuetz, "Magnetic vortex core reversal by excitation of spin waves.," Nat. Commun. **2**, 279 (2011) (cit. on pp. 61, 66).

Kasai, S., K. Nakano, K. Kondou, N. Ohshima, K. Kobayashi, and T. Ono, "Three-Terminal Device Based on the Current-Induced Magnetic Vortex Dynamics with the Magnetic Tunnel Junction," Appl. Phys. Express **1**, 091302 (2008) (cit. on p. 54).

Katine, J. A., F. J. Albert, R. A. Buhrman, E. B. Myers, and D. C. Ralph, "Current-Driven Magnetization Reversal and Spin-Wave Excitations in Co / Cu / Co Pillars," Phys. Rev. Lett. **84**, 3149–3152 (2000) (cit. on p. 86).

Kholmetskii, A. L., T. Yarman, and O. V. Missevitch, "Kündig's experiment on the transverse Doppler shift re-analyzed," Phys. Scr. **77**, 035302 (2008) (cit. on p. 21).

Kholmetskii, A. L., T. Yarman, O. V. Missevitch, and B. I. Rogozev, "A Mössbauer experiment in a rotating system on the second-order Doppler shift: confirmation of the corrected result by Kündig," Phys. Scr. **79**, 065007 (2009) (cit. on p. 21).

Kim, D.-H., E. A. Rozhkova, I. V. Ulasov, S. D. Bader, T. Rajh, M. S. Lesniak, and V. Novosad, "Biofunctionalized magnetic-vortex microdiscs for targeted cancer-cell destruction.," Nat. Mater. **9**, 165–71 (2010) (cit. on p. 54).

Kirschenbaum, L., C. Rogers, S. Russek, and S. Sanders, "Telegraph noise in silver-Permalloy giant magnetoresistance test structures," IEEE Trans. Magn. **31**, 3943–3945 (1995) (cit. on pp. 109, 110).

Kiselev, S. I., J. C. Sankey, I. N. Krivorotov, N. C. Emley, R. J. Schoelkopf, R. A. Buhrman, and D. C. Ralph, "Microwave oscillations of a nanomagnet driven by a spin-polarized current.," Nature **425**, 380–3 (2003) (cit. on p. 86).

Kittel, C., "On the Theory of Ferromagnetic Resonance Absorption," Phys. Rev. **73**, 155–161 (1948) (cit. on pp. 15, 24).

——, *Introduction to solid state physics*, 8th. (Wiley & Sons, Inc., New York, 2004), (cit. on pp. 10, 15, 102).

Kosevich, A. M., B. A. Ivanov, and A. S. Kovalev, "Magnetic Solitons," Phys. Rep. **194**, 117–238 (1990) (cit. on pp. 77, 83).

Krüger, B., A. Drews, M. Bolte, U. Merkt, D. Pfannkuche, and G. Meier, "Vortices and antivortices as harmonic oscillators," J. Appl. Phys. **103**, 07A501 (2008) (cit. on p. 54).

Kündig, W., "Measurement of the Transverse Doppler Effect in an Accelerated System," Phys. Rev. **129**, 2371–2375 (1963) (cit. on p. 21).

Kurti, N., *Selected Works of Louis Néel* (CRC Press, 1988), (cit. on p. 14).

Landau, L. D. and E. Lifshitz, *The Classical Theory of Fields, Fourth Edition: Volume 2 (Course of Theoretical Physics Series)*, 4th (Pergamon Press, New York, 1975), (cit. on pp. 21, 23).

——, *Mechanics, Third Edition: Volume 1 (Course of Theoretical Physics Series)*, 3rd (Pergamon Press, New York, 1982), (cit. on p. 22).

Langan, P., R. Robinson, P. J. Brown, D. Argyriou, D. Hendrickson, and G. Christou, "A low-temperature neutron diffraction study of Mn_{12} -acetate," Acta Crystallogr. Sect. C Cryst. Struct. Commun. **57**, 909–910 (2001) (cit. on p. 41).

Lee, K.-J., A. Deac, O. Redon, J.-P. Nozières, and B. Dieny, "Excitations of incoherent spin-waves due to spin-transfer torque.," Nat. Mater. **3**, 877–81 (2004) (cit. on p. 109).

Lee, K.-S., S.-K. Kim, Y.-S. Yu, Y.-S. Choi, K. Y. Guslienko, H. Jung, and P. Fischer, "Universal Criterion and Phase Diagram for Switching a Magnetic Vortex Core in Soft Magnetic Nanodots," Phys. Rev. Lett. **101**, 267206 (2008) (cit. on p. 61).

Lis, T., "Preparation, structure, and magnetic properties of a dodecanuclear mixed-valence manganese carboxylate," Acta Crystallogr. Sect. B Struct. Crystallogr. Cryst. Chem. **36**, 2042–2046 (1980) (cit. on p. 36).

Locatelli, N., V. Cros, and J. Grollier, "Spin-torque building blocks.," Nat. Mater. **13**, 11–20 (2014) (cit. on p. 78).

Locatelli, N., A. Mizrahi, A. Accioly, R. Matsumoto, A. Fukushima, H. Kubota, S. Yuasa, V. Cros, L. G. Pereira, D. Querlioz, J.-V. Kim, and J. Grollier, "Noise-Enhanced Synchronization of Stochastic Magnetic Oscillators," Phys. Rev. Appl. **2**, 034009 (2014) (cit. on p. 101).

Lv, G., H. Zhang, X. Cao, F. Gao, and Y. Liu, "Micromagnetic simulations of magnetic normal modes in elliptical nanomagnets with a vortex state," Appl. Phys. Lett. **103**, 1–4 (2013) (cit. on pp. 73, 74).

Macià, F., D. Backes, and A. D. Kent, "Stable magnetic droplet solitons in spin-transfer nanocontacts.," Nat. Nanotechnol. **9**, 992–6 (2014) (cit. on pp. 78, 86, 92, 97, 100, 102).

Macià, F., A. D. Kent, and F. C. Hoppensteadt, "Spin-wave interference patterns created by spin-torque nano-oscillators for memory and computation.," Nanotechnology **22**, 095301 (2011) (cit. on p. 78).

Macià, F., P. Warnicke, D. Bedau, M.-Y. Im, P. Fischer, D. Arena, and A. Kent, "Perpendicular magnetic anisotropy in ultrathin Co|Ni multilayer films studied with ferromagnetic resonance and magnetic x-ray microspectroscopy," J. Magn. Magn. Mater. **324**, 3629–3632 (2012) (cit. on p. 88).

Mashhoon, B., “Nonlocal theory of accelerated observers,” Phys. Rev. A **47**, 4498–4501 (1993) (cit. on p. 21).

Masseboeuf, A., O. Fruchart, F. Cheynis, N. Rougemaille, J. C. Toussaint, A. Marty, and P. Bayle-Guillemaud, “Micromagnetic study of flux-closure states in Fe dots using quantitative Lorentz microscopy,” Ultramicroscopy **115**, 26–34 (2012) (cit. on p. 74).

McCord, J., B. Erkartal, T. von Hofe, L. Kienle, E. Quandt, O. Roshchupkina, and J. Grenzer, “Revisiting magnetic stripe domains — anisotropy gradient and stripe asymmetry,” J. Appl. Phys. **113**, 073903 (2013) (cit. on p. 56).

McGuire, T. and R. Potter, “Anisotropic magnetoresistance in ferromagnetic 3d alloys,” IEEE Trans. Magn. **11**, 1018–1038 (1975) (cit. on p. 79).

Messiah, A., *Quantum mechanics* (Wiley, New York, 1976) (cit. on p. 23).

Mironov, V. L., O. L. Ermolaeva, S. A. Gusev, A. Y. Klimov, V. V. Rogov, B. A. Gribkov, O. G. Udalov, A. A. Fraerman, R. Marsh, C. Checkley, R. Shaikhaidarov, and V. T. Petrashov, “Antivortex state in crosslike nanomagnets,” Phys. Rev. B **81**, 094436 (2010) (cit. on pp. 54, 58).

Miyazaki, T., T. Yaoi, and S. Ishio, “Large magnetoresistance effect in 82Ni-Fe/Al-Al2O3/Co magnetic tunneling junction,” J. Magn. Magn. Mater. **98**, L7–L9 (1991) (cit. on p. 79).

Mohseni, S. M., S. R. Sani, R. K. Dumas, J. Persson, T. N. Anh Nguyen, S. Chung, Y. Pogoryelov, P. K. Muduli, E. Iacocca, A. Eklund, and J. Åkerman, “Magnetic droplet solitons in orthogonal nano-contact spin torque oscillators,” Phys. B Condens. Matter **435**, 84–87 (2014) (cit. on pp. 78, 86, 100).

Mohseni, S. M., S. R. Sani, J. Persson, T. N. A. Nguyen, S. Chung, Y. Pogoryelov, P. K. Muduli, E. Iacocca, A. Eklund, R. K. Dumas, S. Bonetti, A. Deac, M. A. Hoefer, and J. Åkerman, “Spin torque-generated magnetic droplet solitons.,” Science **339**, 1295–8 (2013) (cit. on pp. 78, 86, 92, 100).

Momma, K. and F. Izumi, “VESTA 3 for three-dimensional visualization of crystal, volumetric and morphology data,” J. Appl. Crystallogr. **44**, 1272–1276 (2011) (cit. on p. 37).

Myers, E. B., “Current-Induced Switching of Domains in Magnetic Multilayer Devices,” Science **285**, 867–870 (1999) (cit. on p. 86).

Nelson, D. R., “Orientational ordering in 2- and 3-dimensional systems,” J. Non. Cryst. Solids **61-62**, 475–485 (1984) (cit. on p. 49).

Nienhuis, G., “Doppler effect induced by rotating lenses,” Opt. Commun. **132**, 8–14 (1996) (cit. on pp. 20, 22).

Novosad, V., F. Y. Fradin, P. E. Roy, K. S. Buchanan, K. Y. Guslienko, and S. D. Bader, “Magnetic vortex resonance in patterned ferromagnetic dots,” Phys. Rev. B **72**, 024455 (2005) (cit. on p. 59).

Novosad, V., K. Y. Guslienko, H. Shima, Y. Otani, S. Kim, K. Fukamichi, N. Kikuchi, O. Kitakami, and Y. Shimada, “Effect of interdot magnetostatic interaction on magnetization reversal in circular dot arrays,” Phys. Rev. B **65**, 2–5 (2002) (cit. on p. 67).

Padgett, M., “Electromagnetism: like a speeding watch.,” Nature **443**, 924–5 (2006) (cit. on pp. 22, 29).

Politi, P., A. Rettori, F. Hartmann-Boutron, and J. Villain, “Tunneling in Mesoscopic Magnetic Molecules,” Phys. Rev. Lett. **75**, 537–540 (1995) (cit. on p. 36).

Pribiag, V. S., I. N. Krivorotov, G. D. Fuchs, P. M. Braganca, O. Ozatay, J. C. Sankey, D. C. Ralph, and R. A. Buhrman, “Magnetic vortex oscillator driven by d.c. spin-polarized current,” Nat. Phys. **3**, 498–503 (2007) (cit. on p. 73).

Pues, M., M. Martens, T. Kamionka, and G. Meier, “Reliable nucleation of isolated magnetic antivortices,” Appl. Phys. Lett. **100**, 162404 (2012) (cit. on p. 54).

Puliafito, V., G. Siracusano, B. Azzerboni, and G. Finocchio, “Self-Modulated Soliton Modes Excited in a Nanocontact Spin-Torque Oscillator,” IEEE Magn. Lett. **5**, 1–4 (2014) (cit. on p. 100).

Ralls, K. S., W. J. Skocpol, L. D. Jackel, R. E. Howard, L. A. Fetter, R. W. Epworth, and D. M. Tennant, “Discrete Resistance Switching in Submicrometer Silicon Inversion Layers: Individual Interface Traps and Low-Frequency (1/f ?) Noise,” Phys. Rev. Lett. **52**, 228–231 (1984) (cit. on p. 109).

Rippard, W., M. Pufall, S. Kaka, S. Russek, and T. Silva, “Direct-Current Induced Dynamics in $Co_{90}Fe_{10}$ / $Ni_{80}Fe_{20}$ Point Contacts,” Phys. Rev. Lett. **92**, 027201 (2004) (cit. on p. 86).

Rozhkova, E. A., V. Novosad, D.-H. Kim, J. E. Pearson, R. Divan, T. Rajh, and S. D. Bader, “Ferromagnetic microdisks as carriers for biomedical applications,” J. Appl. Phys. **105**, 2009–2012 (2009) (cit. on p. 54).

Sales, M., J. M. Hernandez, J. Tejada, and J. L. Martínez, “Time-dependent heat capacity of Mn_{12} clusters,” Phys. Rev. B **60**, 14557–14560 (1999) (cit. on pp. 34, 39, 49).

Schlegel, C., J. van Slageren, M. Manoli, E. K. Brechin, and M. Dressel, "Direct Observation of Quantum Coherence in Single-Molecule Magnets," Phys. Rev. Lett. **101**, 147203 (2008) (cit. on p. 34).

Schneider, M., H. Hoffmann, and J. Zweck, "Lorentz microscopy of circular ferromagnetic permalloy nanodisks," Appl. Phys. Lett. **77**, 2909 (2000) (cit. on p. 56).

Shinjo, T., T. Okuno, R. Hassdorf, K. Shigeto, and T. Ono, "Magnetic Vortex Core Observation in Circular Dots of Permalloy," Science **289**, 930–932 (2000) (cit. on p. 56).

Simoen, E. and C. Claeys, "On the flicker noise in submicron silicon MOSFETs," Solid. State. Electron. **43**, 865–882 (1999) (cit. on p. 109).

Simoen, E., B. Kaczer, M. Toledano-Luque, and C. Claeys, "(Invited) Random Telegraph Noise: From a Device Physicist's Dream to a Designer's Nightmare," ECS Trans. **39**, 3–15 (2011) (cit. on p. 109).

Simon, R., H. J. Kimble, and E. C. G. Sudarshan, "Evolving Geometric Phase and Its Dynamical Manifestation as a Frequency Shift: An Optical Experiment," Phys. Rev. Lett. **61**, 19–22 (1988) (cit. on p. 22).

Slonczewski, J. C., "Current-driven excitation of magnetic multilayers," J. Magn. Magn. Mater. **159**, L1–L7 (1996) (cit. on pp. 78, 79).

———, "Excitation of spin waves by an electric current," J. Magn. Magn. Mater. **195**, L261–L268 (1999) (cit. on pp. 78, 81).

Subedi, P., S. Vélez, F. Macià, S. Li, M. P. Sarachik, J. Tejada, S. Mukherjee, G. Christou, and A. D. Kent, "Onset of a Propagating Self-Sustained Spin Reversal Front in a Magnetic System," Phys. Rev. Lett. **110**, 207203 (2013) (cit. on p. 34).

Suzuki, Y., M. P. Sarachik, E. M. Chudnovsky, S. McHugh, R. Gonzalez-Rubio, N. Avraham, Y. Myasoedov, E. Zeldov, H. Shtrikman, N. E. Chakov, and G. Christou, "Propagation of Avalanches in Mn_{12} -Acetate: Magnetic Deflagration," Phys. Rev. Lett. **95**, 147201 (2005) (cit. on p. 34).

Tejada, J., E. M. Chudnovsky, E. del Barco, J. M. Hernandez, and T. P. Spiller, "Magnetic qubits as hardware for quantum computers," Nanotechnology **12**, 181–186 (2001) (cit. on p. 34).

Tejada, J., R. D. Zysler, E. Molins, and E. M. Chudnovsky, "Evidence for Quantization of Mechanical Rotation of Magnetic Nanoparticles," Phys. Rev. Lett. **104**, 027202 (2010) (cit. on pp. 22, 30).

Thiele, A., "Steady-State Motion of Magnetic Domains," Phys. Rev. Lett. **30**, 230–233 (1973) (cit. on p. 59).

Thomas, L., F. Lionti, R. Ballou, D. Gatteschi, R. Sessoli, and B. Barbara, "Macroscopic quantum tunnelling of magnetization in a single crystal of nanomagnets," Nature **383**, 145–147 (1996) (cit. on pp. 34, 38).

Tokman, I. D. and V. I. Pozdnyakova, "Mechanical rotation of nanomagnet through interaction with an electromagnetic wave," Eur. Phys. J. B **88**, 51 (2015) (cit. on p. 30).

Tsoi, M., A. G. M. Jansen, J. Bass, W.-C. Chiang, M. Seck, V. Tsoi, and P. Wyder, "Excitation of a Magnetic Multilayer by an Electric Current," Phys. Rev. Lett. **80**, 4281–4284 (1998) (cit. on p. 101).

Uhlíř, V., M. Urbánek, L. Hladík, J. Spousta, M.-Y. Im, P. Fischer, N. Eibagi, J. J. Kan, E. E. Fullerton, and T. Sikola, "Dynamic switching of the spin circulation in tapered magnetic nanodisks.," Nat. Nanotechnol. **8**, 341–6 (2013) (cit. on p. 54).

Urazhdin, S., N. O. Birge, W. P. Pratt, and J. Bass, "Current-Driven Magnetic Excitations in Permalloy-Based Multilayer Nanopillars," Phys. Rev. Lett. **91**, 146803 (2003) (cit. on p. 101).

Van Waeyenberge, B., A. Puzic, H. Stoll, K. W. Chou, T. Tyliszczak, R. Hertel, M. Fähnle, H. Brückl, K. Rott, G. Reiss, I. Neudecker, D. Weiss, C. H. Back, and G. Schütz, "Magnetic vortex core reversal by excitation with short bursts of an alternating field.," Nature **444**, 461–4 (2006) (cit. on pp. 60, 66).

Vansteenkiste, A., J. Leliaert, M. Dvornik, M. Helsen, F. Garcia-Sanchez, and B. Van Waeyenberge, "The design and verification of MuMax3," AIP Adv. **4**, 107133 (2014) (cit. on pp. 69, 96).

Vavassori, P., N. Zaluzec, V. Metlushko, V. Novosad, B. Ilic, and M. Grimsditch, "Magnetization reversal via single and double vortex states in submicron Permalloy ellipses," Phys. Rev. B **69**, 214404 (2004) (cit. on p. 67).

Vlaminck, V. and M. Bailleul, "Current-induced spin-wave Doppler shift," Science **322**, 410–3 (2008) (cit. on p. 22).

Vukadinovic, N. and F. Boust, "Three-dimensional micromagnetic simulations of magnetic excitations in cylindrical nanodots with perpendicular anisotropy," Phys. Rev. B **75**, 014420 (2007) (cit. on p. 73).

———, "Three-dimensional micromagnetic simulations of multidomain bubble-state excitation spectrum in ferromagnetic cylindrical nanodots," Phys. Rev. B **78**, 184411 (2008) (cit. on p. 74).

Vukadinovic, N., F. Boust, and S. Labbé, "Domain wall resonant modes in nanodots with a perpendicular anisotropy," J. Magn. Magn. Mater. **310**, 2324–2326 (2007) (cit. on p. 74).

Wernsdorfer, W. and R. Sessoli, “Quantum Phase Interference and Parity Effects in Magnetic Molecular Clusters,” Science **284**, 133–135 (1999) (cit. on p. 34).

Xia, K., P. J. Kelly, G. E. W. Bauer, A. Brataas, and I. Turek, “Spin torques in ferromagnetic/normal-metal structures,” Phys. Rev. B **65**, 220401 (2002) (cit. on p. 80).

Xiao, Q. F., J. Rudge, B. C. Choi, Y. K. Hong, and G. Donohoe, “Dynamics of vortex core switching in ferromagnetic nanodisks,” Appl. Phys. Lett. **89**, 262507 (2006) (cit. on p. 66).

Xu, X., S. Yin, R. Moro, and W. A. de Heer, “Magnetic Moments and Adiabatic Magnetization of Free Cobalt Clusters,” Phys. Rev. Lett. **95**, 237209 (2005) (cit. on p. 22).

Yan, M., R. Hertel, and C. M. Schneider, “Calculations of three-dimensional magnetic normal modes in mesoscopic permalloy prisms with vortex structure,” Phys. Rev. B **76**, 094407 (2007) (cit. on pp. 74, 75).

Zarzuela, R., E. M. Chudnovsky, J. M. Hernandez, and J. Tejada, “Quantum dynamics of vortices in mesoscopic magnetic disks,” Phys. Rev. B **87**, 144420 (2013) (cit. on p. 54).

Zarzuela, R., E. M. Chudnovsky, and J. Tejada, “Excitation modes of vortices in submicron magnetic disks,” Phys. Rev. B **87**, 014413 (2013) (cit. on p. 75).

Zarzuela, R., S. Vélez, J. M. Hernandez, J. Tejada, and V. Novosad, “Quantum depinning of the magnetic vortex core in micron-size permalloy disks,” Phys. Rev. B **85**, 180401 (2012) (cit. on p. 54).

Zélis, P. M., I. J. Bruvera, M. P. Calatayud, G. F. Goya, and F. H. Sánchez, “Determination of the blocking temperature of magnetic nanoparticles: The good, the bad and the ugly,” (2015), arXiv:`1508.04413` (cit. on p. 43).

Zhang, B., W. Wang, C. Mu, Q. Liu, and J. Wang, “Calculations of three-dimensional magnetic excitations in permalloy nanostructures with vortex state,” J. Magn. Magn. Mater. **322**, 2480–2484 (2010) (cit. on p. 74).

Zimmler, M. A., B. Özyilmaz, W. Chen, A. D. Kent, J. Z. Sun, M. J. Rooks, and R. H. Koch, “Current-induced effective magnetic fields in Co/Cu/Co nanopillars,” Phys. Rev. B **70**, 184438 (2004) (cit. on p. 80).

Related Publications

Chapter 3: Rotational Doppler Effect in FMR

[1] Lendínez, S., E. M. Chudnovsky, and J. Tejada, "Rotational Doppler effect in magnetic resonance," Phys. Rev. B **82**, 174418 (2010).

We study the effect of rotation on the various magnetic resonances of a body. In particular, we obtain expressions of the Doppler shift produced by a circularly polarized electromagnetic wave on a rotating body for the Electron-Spin Resonance (ESR), the Nuclear Magnetic Resonance (NMR) and Ferromagnetic Resonance (FMR). In addition, we compute the power absorbed by a rotating magnet through the FMR when a linearly polarized electromagnetic wave is used.

Contribution: Theoretical analysis on the Doppler effect in FMR, calculation on the power absorption and partial writing of the manuscript.

Chapter 4: Resonant Spin Tunneling in Single-Molecule Magnets

[2] Lendínez, S., R. Zarzuela, J. Tejada, M. W. Terban, S. J. L. Billinge, J. Espin, I. Imaz, D. Maspoch, and E. M. Chudnovsky, "Resonant spin tunneling in randomly oriented nanospheres of Mn_{12} acetate," Phys. Rev. B **91**, 024404 (2015).

We give experimental evidence of the macroscopic tunneling of the magnetization in randomly-oriented nanospheres of Mn_{12}. We propose an analysis to explain the observed behavior and suggest that this analysis would make the identification of tunneling in new compounds easier.

Contribution: Magnetization measurements of the Mn_{12} nanospheres and microcrystals, analysis of the magnetization data, and partial writing of the manuscript.

Chapter 5: Magnetic Vortices in Elongated Patterns

[3] Lendínez, S., S. Jain, V. Novosad, F. Y. Fradin, J. E. Pearson, J. Tejada, and S. D. Bader, "Dynamic decay of a single vortex into vortex-antivortex pairs," J. Appl. Phys. **115**, 17D121 (2014).

We create antivortex structures by exciting ferromagnetic ellipses having a vortex configuration of the magnetization. The ferromagnetic ellipses of $Fe_{20}Ni_{80}$ are patterned on top of coplanar waveguides that allow us to measure the spectral response to microwave excitations. We observe the vortex disappearance with spectral measurements and confirm the antivortex creation with magnetic force microscopy images.

Contribution: Design of the experimental setup, measurements of the spectral response and magnetic force microscopy, and writing of the manuscript.

Chapter 6: Magnetic Doplet Solitons in Thin Films

[4] Lendínez, S., N. Statuto, D. Backes, A. D. Kent, and F. Macià, "Observation of droplet soliton drift resonances in a spin-transfer-torque nanocontact to a ferromagnetic thin film," (2015), arXiv:`1507.08218`, accepted in Phys. Rev. B.

We observe a low-frequency noise in the spectral response of a nanocontact to a ferromagnetic thin film. We attribute it to the movement of a droplet soliton beneath the nanocontact area due to drift instabilities. We argue that the drift instabilities are produced by an effective asymmetry in the field in the nanocontact region, and give some possible explanations that may turn out in an asymmetry with micromagnetic simulations.

Contribution: Design of the experimental setup, measurements of the spectral and dc response, and writing of the manuscript.

[5] Lendínez, S., S. Vélez, L. Hueso, D. Backes, A. D. Kent, and F. Macià, "Temperature stability of a magnetic droplet soliton in a nanocontact to a thin film," (2015), in preparation.

We study the temperature dependance of the stability of the droplet soliton with dc measurements from 2 K to 350 K. We find that, contrary to STNOs, the droplet is more stable at low temperatures. This might be due to the effects of pinning ponential acting on the reversed magnetization. At lower temperatures, the pinning barriers cannot be overcome and the droplet is fixed.

Contribution: Design of the experimental setup, measurements of the dc response, and writing of the manuscript.

Other Publications

[6] Ding, J., S. Jain, J. E. Pearson, S. Lendinez, V. Khovaylo, and V. Novosad, "Dynamic control of metastable remanent states in mesoscale magnetic elements," J. Appl. Phys. **117**, 17A707 (2015).

[7] Posada, C. M., P. A. R. Ade, Z. Ahmed, K. Arnold, J. E. Austermann, A. N. Bender, L. E. Bleem, B. A. Benson, K. Byrum, J. E. Carlstrom, C. L. Chang, H. M. Cho, S. T. Ciocys, J. F. Cliche, T. M. Crawford, A. Cukierman, D. Czaplewski, J. Ding, R. Divan, T. de Haan, M. A. Dobbs, D. Dutcher, W. Everett, A. Gilbert, N. W. Halverson, N. L. Harrington, K. Hattori, J. W. Henning, G. C. Hilton, W. L. Holzapfel, J. Hubmayr, K. D. Irwin, O. Jeong, R. Keisler, D. Kubik, C. L. Kuo, A. T. Lee, E. M. Leitch, S. Lendinez, S. S. Meyer, C. S. Miller, J. Montgomery, M. Myers, A. Nadolski, T. Natoli, H. Nguyen, V. Novosad, S. Padin, Z. Pan, J. E. Pearson, J. E. Ruhl, B. R. Saliwanchik, G. Smecher, J. T. Sayre, E. Shirokoff, L. Stan, A. A. Stark, J. Sobrin, K. Story, A. Suzuki, K. L. Thompson, C. Tucker, K. Vanderlinde, J. D. Vieira, G. Wang, N. Whitehorn, V. Yefremenko, K. W. Yoon, and K. E. Ziegler, "Fabrication of large dual-polarized multichroic TES bolometer arrays for CMB measurements with the SPT-3G camera," Supercond. Sci. Technol. **28**, 094002 (2015).